

DYNAMICS OF RECONFIGURABLE MULTIBODY SPACE SYSTEMS  
CONNECTED BY MAGNETIC FLUX PINNING

A Dissertation

Presented to the Faculty of the Graduate School  
of Cornell University

in Partial Fulfillment of the Requirements for the Degree of  
Doctor of Philosophy

by

Joseph Paul Shoer

May 2011

© 2011 Joseph Paul Shoer

DYNAMICS OF RECONFIGURABLE MULTIBODY SPACE SYSTEMS  
CONNECTED BY MAGNETIC FLUX PINNING

Joseph Paul Shoer, Ph. D.

Cornell University 2011

Many future space systems, from solar power collection satellites to sparse-aperture telescopes, will involve large-scale space structures which must be launched in a modular fashion. Currently, assembling modular structures in orbit is a challenging problem in multi-vehicle control or human-vehicle interaction. Some novel approaches to assembling modular space structures or formation-flying space systems involve augmenting the system dynamics with non-contacting force fields such as electromagnetic interactions. However, familiar divergenceless forces are subject to Earnshaw's Theorem and require active control in 6 DOF for stability. This study proposes an approach to modular spacecraft assembly based on the passively stable physics of magnetic flux pinning, an interaction between superconductors and magnetic fields which is not limited by Earnshaw's Theorem. Spacecraft modules linked by flux pinning passively fall into stable, many-degree-of-freedom basins of attraction in which flux pinning holds the modules together with stiffness and damping but no mechanical contact. This dissertation reports several system identification experiments that characterize the physical properties of flux pinning for spacecraft applications and identify avenues for design of flux-pinning space hardware.

Once assembled in orbit, altering a spacecraft to effect repairs or adapt to new missions presents significant control challenges as well. Flux-pinning technology also offers exciting possibilities for new spacecraft-reconfiguration techniques, in which a spacecraft changes structure and function at the system level. Flux-pinned modular

spacecraft can reconfigure in such a way that the passive physics of flux pinning and the space environment govern the low-level dynamics of a reconfiguration maneuver, instead of full-state feedback control. These reconfiguration maneuvers take the form of sequences of passively stable evolutions to equilibrium states, with joint kinematics between modules preventing collisions. This dissertation develops a theory for multibody spacecraft reconfiguration controllers that take a high-level, hybrid-systems approach in which a pre-computed graph structure stores all the reachable configurations that meet certain design-specified criteria. Edges of the graph carry mission-related weights so that a space system can optimize power consumption, robustness measures, or other performance metrics during a maneuver. These technologies and control strategies may provide opportunities for versatile space systems that can accomplish a wide variety of future missions.

## BIOGRAPHICAL SKETCH

Joseph Shoer was born in Maine and grew up in central Massachusetts. In high school, he became an active member of the Civil Air Patrol. He eventually held the position of cadet commander of his squadron and earned numerous awards, including the Frank G. Brewer Award for Excellence in Aerospace Education and the General Billy Mitchell Award, a national award that recognizes the entrance into cadet officer grades. During the summers of 2001 and 2002, Joseph worked as an intern in the solar physics group at the Harvard-Smithsonian Center for Astrophysics.

Joseph attended Williams College, where he majored in physics. His senior thesis concerned experiments on and numerical simulations of an all-fiber laser designed to produce soliton pulses for optical communication purposes. For his physics thesis and work in the science tutoring program, Joseph was awarded the Howard P. Stabler Prize in Physics when he graduated in 2006.

His enthusiasm for space exploration and scientific research led Joseph to pursue Ph.D. studies in aerospace engineering at Cornell University. In addition to his work on flux-pinned spacecraft technologies and systems, Joseph avidly pursued studies in planetary astronomy, and spent the summer of the 40<sup>th</sup> anniversary of Apollo 11 working on the new lunar rover concept at Johnson Space Center. His NASA program coordinator appointed him as a NASA Student Ambassador after that work.

Joseph looks forward to working on next-generation space exploration programs in the future.

## ACKNOWLEDGMENTS

First and foremost, I want to thank my research advisor and committee chair, Dr. Mason Peck. He has been a tremendous advisor for me, from hours spent in his office bouncing crazy ideas around, to impromptu runs into the lab to share results and brainstorm techniques, to connecting me with a summer position at NASA. Not every professor is like Mason, and I appreciated every moment of it.

My other committee members have provided insight and assistance that shaped my approach to this research. I want to thank Joseph Burns for helping keep my astronomy studies straight and Hadas Kress-Gazit for giving me all sorts of ideas about hybrid systems that came in very handy when I was setting up my multibody dynamics simulations. I would also like to thank Mark Campbell for discussions about system ID techniques that were very useful in processing my pendulum experiment data and for providing me with a great experience as a TA.

The undergraduates, M.Eng. students, graduate students, and staff members who have worked with me in the lab – Sachit Butail, Brian Kashawlic, Timothy Szwarc, William Wilson, Max Knobel, Mike Norman, Laura Jones, Jessica Gersh, and Liran Gazit – made contributions to the flux-pinned spacecraft research effort that were invaluable in pushing my own research forward. My sincerest thanks go to all of them.

This research offered me the chance to fly with a microgravity experiment on a NASA “vomit comet” aircraft, something I did not anticipate I would have the opportunity to do. I would like to thank the administrators of the NASA FAST program at Glenn Research Center, the physiological training staff at Johnson Space Center’s Sonny Carter Training Facility, and the staff and flight crew from the JSC Reduced Gravity Office for giving me that fantastic experience.

In addition, I want to thank all the people who offered the little thoughts, perspectives, and bits of advice that helped nudge me in the right direction: Marcia, the other MAE faculty, and whichever other grad students happened to be near me in the office at the time.

Finally, my heartfelt thanks go to all my old friends, family, Mom and Dad, and Nicole for encouraging me to keep pushing and pursue my dreams all the way into outer space.

## TABLE OF CONTENTS

Biographical Sketch	iii
Acknowledgments	iv
Table of Contents	vi
List of Figures	viii
Chapter 1 Introduction	1
1.1 Motivation	1
1.2 The Physics of Magnetic Flux Pinning	5
1.3 Technological Applications of Flux Pinning	7
1.4 Kinematic Reconfiguration Control Strategies	10
1.5 Overview and Contributions	12
Chapter 2 Stiffness of a Flux-Pinned Virtual Structure for Modular Spacecraft	16
2.1 Testing the Mechanical Properties of Flux Pinning	16
2.1.1 Static Experiment	16
2.1.2 Static Model	19
2.2 Experiment Results and Discussion	20
2.3 Chapter Conclusions	31
Chapter 3 Reconfigurable Spacecraft as Kinematic Mechanisms	36
3.1 Reconfiguration Mechanisms	36
3.2 Example Applications	39
3.3 Chapter Conclusions	42
Chapter 4 Flux-Pinned Interfaces for the Assembly, Manipulation, and Reconfiguration of Modular Space Systems	44
4.1 Properties of the Interface	45
4.2 Image-Dipole Model	50
4.3 Experiment	54
4.4 Results and Discussion	59
4.4.1 Range of Flux Pinning	59
4.4.2 Pendulum Mode Modification	60
4.4.3 Performance modification and actuation of flux-pinned interfaces	64
4.5 Chapter Conclusions	68
Chapter 5 Microgravity Demonstrations of Flux Pinning for Station-Keeping and Reconfiguration of CubeSat-Sized Spacecraft	73
5.1 6DOF Station-Keeping Demonstration	74
5.2 Revolute Joint Demonstration	76
5.3 Chapter Conclusions	79
Chapter 6 Simulation of Multibody Spacecraft Reconfiguration through Sequential Dynamic Equilibria	81
6.1 The Sequential-Equilibrium Reconfiguration Concept	82
6.2 Formulation of Udwadia and Kalaba's Fundamental Equation with Quaternion Coordinates	88
6.2.1 Derivation of General Equation of Motion with Quaternion States	88

6.2.2	Constraint Matrices for Joints with Quaternion Coordinates	91
6.3	Simulation of Sequential Multibody Reconfiguration	94
6.3.1	Simulation of Two-Equilibrium Laboratory Demonstrations	96
6.3.2	Planetary Imaging Mission	98
6.3.3	Imaging Mission Graph-Weighting Schemes	102
6.4	Chapter Conclusions	104
Chapter 7 Conclusions		107
References		110

## LIST OF FIGURES

Fig. 1-1 A non-contacting, modular CubeSat spacecraft concept with a flux-pinned interface capable of action-at-a-distance six degree-of-freedom actuation.	4
Fig. 1-2 A cylindrical permanent magnet (1.9 cm dia.) flux pinned with its center about 2 cm above the surface of a YBCO superconductor.	5
Fig. 1-3 Reconfigurable optical mirrors assembled from modules with non-contacting interfaces.	7
Fig. 2-1 Experimental setup with robot arm, load cell, permanent magnet, and superconductor.	17
Fig. 2-2 $k_{11}$ ( $x$ translation stiffness) versus separation distance $d$ for several magnet tilt angles $\beta$ .	22
Fig. 2-3 $k_{22}$ ( $y$ translation stiffness) versus separation distance $d$ for several magnet tilt angles $\beta$ .	23
Fig. 2-4 $k_{33}$ ( $z$ translation stiffness) versus separation distance $d$ for several magnet tilt angles $\beta$ .	24
Fig. 2-5 $k_{44}$ ( $\theta_x$ rotation stiffness) versus separation distance $d$ for several magnet tilt angles $\beta$ .	25
Fig. 2-6 $k_{55}$ ( $\theta_y$ rotation stiffness) versus separation distance $d$ for several magnet tilt angles $\beta$ .	26
Fig. 2-7 $k_{33}$ (relating $z$ to $F_z$ ) versus separation distance $d$ when a number of identical permanent magnets was stacked into a longer cylinder ( $N = 1, 2,$ and $3$ ) at tilt $\beta = 0^\circ$ .	27
Fig. 2-8 Stiffness $k_{33}$ (relating $z, F_z$ ) versus measured flux density over all experimental trials.	28
Fig. 2-9 Contours of fixed stiffness for desired module separation as a function of the mass of the magnet necessary to achieve that stiffness.	29
Fig. 3-1 Flux-pinned joints with one or more degrees of freedom. Arrows indicate unconstrained motions of the superconducting cube. Left to right: revolute joint, cylindrical joint, and prismatic joint.	38
Fig. 3-2 Reconfiguration of a linear chain of modules by kinematic mechanism formation. Dashed double lines represent fully constrained FPIs and dashed circles represent FPIs with one rotation DOF. (top) walking reconfiguration and (bottom) Jacob's-ladder reconfiguration.	39
Fig. 3-3 Air-table demonstration of a non-contacting kinematic joint actuated by a momentum wheel.	41
Fig. 4-1 Kinematic mechanisms formed by flux pinning a superconducting cube to the fields of permanent magnets. The cube may freely undergo only the indicated motions. Left to right: revolute joint, cylindrical joint, and prismatic joint.	46
Fig. 4-2 Three possible modes of reconfiguration. (a) Flux pinning fixes modules only in their initial and end states, other actuators (thrusters shown) are used for the reconfiguration. (b) Flux pinning selects the available degrees of freedom between	

modules; in this example a hinge. (c) Electromagnets bend flux-pinned interfaces and articulate a modular structure.	48
Fig. 4-3 Image-dipole model of flux pinning. Top: frozen and mobile images appear within the superconducting volume upon field-cooling. Bottom: the frozen image remains fixed, while the mobile image moves with the magnet.	50
Fig. 4-4 Log-log plot of translational stiffness of a flux-pinned magnet-superconductor pair against flux density at the superconductor surface.	53
Fig. 4-5 Experimental setup, showing the placement of the (a) vertically-mounted YBCO superconductor in its liquid nitrogen bath, (b) pendulum with permanent magnet and tracking flags, (c) input coil, (d) motion-capture camera system, and (e) translation stage.	55
Fig. 4-6 Modes of the pendulum bob. From left to right: swinging (perpendicular to the HTSC), swinging (parallel to the HTSC), twisting, rocking, and rolling motion.	56
Fig. 4-7 Modification of pendulum modes, as measured by FFTs of motion capture data.	58
Fig. 4-8 Pendulum frequency modification as a function of field-cooling separation distance; data and frozen-image model.	60
Fig. 4-9 Flux-pinned stiffness as a function of field-cooling separation distance; data and frozen-image model.	61
Fig. 4-10 Flux-pinned stiffness versus magnetic flux density at the superconductor surface upon field-cooling.	63
Fig. 4-11 Flux-pinned stiffness versus field-cooling separation in the presence of an iron plate. Left: experimental measurements, right: frozen-image model of $k_z$ vs. $d$ with iron plate.	64
Fig. 4-12 Damping a flux-pinned interface with a plate of aluminum over the superconductor.	66
Fig. 4-13 Top: schematic of a magnet (red) flux-pinned to a HTSC disc (blue) with an electromagnet coil (gold ring) near the disc. Bottom: simulated time history of the magnet position (blue) and control coil field (green).	67
Fig. 4-14 Design space of a flux-pinned interface based on the 9.0 J/T magnet and single-domain YBCO in these experiments.	68
Fig. 4-15 Potential arrangement of magnets for a flux-pinned interface.	69
Fig. 5-1 (Left) Top-down diagram of the experimental setup on the microgravity flight. The laptop computer and equipment container were secured to the floor of the aircraft, while the magnet modules and superconductor Dewar floated freely during the microgravity portions of the flight. Camera views in this note are from the left to the right on this diagram. (Right) Photograph of the two free-floating magnet modules used in these experiments. The left of the image shows the revolute joint module, and the right of the image shows the 6DOF station-keeping magnet module.	73
Fig. 5-2 Diagram of the 6DOF magnet module cube in flight position relative to the cylindrical superconductor Dewar. The superconductor is mounted at the bottom of the Dewar and the magnets are located on the top face of the cube (permanent magnets in green; electromagnets in red).	74
Fig. 5-3 Still photos of the low-stiffness 6DOF station keeping demo. The superconductors are located at the bottom face of the insulated superconductor carrier;	

magnets are in the top face of the CubeSat mockup. (Photo on right courtesy of NASA.)	75
Fig. 5-4 Diagram of the revolute joint magnet module at its two equilibrium states relative to the superconductor Dewar. The axis of the flux-pinned revolute joint is at the center of the permanent magnet, pointing out of the page.	76
Fig. 5-5 Demonstration of a flux-pinned hinge on a CubeSat mockup at 100 FPS. (a) Flux pinning stiffens the translational motion of the CubeSat, which rotates about the hinge axis of the magnet (intersection of the solid lines). (b) Flux pinning does not prevent the CubeSat from drifting away from the superconductor carrier and the estimate of the hinge axis wanders off of the magnetic axis.	77
Fig. 5-6 Rotation angle between the flux-pinned CubeSat mockup and superconductor carrier about the hinge axis.	79
Fig. 6-1 Potential energies in the stepwise passive reconfiguration concept for a system with two possible degrees of freedom.	84
Fig. 6-2 Sample time history of the system from Fig. 6-1. The control input changes at $t = 100$ s and $t = 600$ s.	85
Fig. 6-3 Potential well linking a flux-pinned magnet and superconductor. The superconducting plane is shaded.	86
Fig. 6-4 First reconfiguration example: multibody system equilibria at two nodes in the reconfiguration graph. The dashed line indicates the rotation axis of a revolute joint. The shaded surface's height shows the potential energy as a function of $x$ and $y$ position of the bodies.	97
Fig. 6-5 System energy as a function of time.	98
Fig. 6-6 Initial setup of the CubeSat-based imaging mission. Blue dots represent possible joint locations.	99
Fig. 6-7 Equilibrium configurations and directed reconfiguration graph of an example system.	100
Fig. 6-8 Imaging-mission reconfiguration graph weighted by a relative measure of the time during which at least one cube face is within $20^\circ$ alignment of an arbitrary vector. Edge labels that are zero are not shown; edges with two transitions are labeled near the head of each arrow.	102
Fig. 6-9 Imaging-mission reconfiguration graph weighted by the maximum percent uncertainty in the individual module masses for which the system successfully completes each transition; edges with two transitions are labeled near the head of each arrow.	103
Fig. 6-10 Air-levitated, CubeSat-sized laboratory demonstration unit.	105

# CHAPTER 1

## INTRODUCTION

### 1.1 Motivation

New approaches to the assembly of modular structures in space will be important for future space-system architectures. The challenges of constructing the International Space Station and any potential successor systems, performing rendezvous of disparate elements of a multi-vehicle mission, dispatching self-repairing or adaptable probes to other bodies in the solar system, and maintaining complex formations in orbit require other paradigms than the common approach of adapting terrestrial construction techniques to the space environment [1]. Furthermore, there are many reasons why reconfigurable spacecraft architectures—spacecraft capable of changing their structure, and possibly function, at the system level—are desirable. This capability may allow advantageous changes to a spacecraft's mass properties, adapt the spacecraft to changing mission requirements, or enable autonomous self-repair. The reconfiguration of modular or swarm spacecraft is currently studied in this context [2,3].

The rigors of the space environment require that spacecraft exhibit a high degree of mission assurance, which often takes the form of autonomous fault tolerance [4,5]. However, the technology for spacecraft repair and reconfiguration missions has not yet matured to the point where autonomous operations are also robust. Many completed and envisioned spacecraft reconfiguration or repair techniques involve substantial human-in-the-loop activity, including successful Hubble Space Telescope repair and expansion missions and proposed Chandra X-Ray Observatory servicing activities [6]. Another example is the construction of the International Space Station,

which astronauts have assembled and reconfigured piecemeal during many hours of extravehicular activity. Fully autonomous repair and reconfiguration tasks have been achieved only recently, such as on the Orbital Express mission [7], with extensive sensing and active control solutions [8].

Docking and assembly technologies based on the phenomenon of magnetic flux pinning (Chapter 2) may enable a new in-orbit construction paradigm in which both small and large space systems self-assemble from components that find one another and settle into place without any material connection. The modules maintain a fixed separation distance from one another through the non-contacting interactions. Since flux pinning features passive stability, this approach to self-assembly requires no active control and no appreciable power; and yet neighboring modules are stiffly positioned and oriented. The non-contacting interface opens up new ways of thinking about fractionated and responsive spacecraft [9,10]. Articulated payloads, reconfigurable space stations, and adaptable satellite architectures are possible without the risk, mass and power typically associated with maintaining formations or mechanically rebuilding structures.

These space systems blur the distinction between mechanically linked modular structures and formation-flying clusters of spacecraft. They span a wide range of scales, from picosatellite clusters to space stations. A non-contacting architecture based on flux-pinning forces confers several advantages over traditional space-assembly paradigms. The safety and robustness of the assembly process would be greatly enhanced, as the integration of a new module onto a structure may only involve maneuvering it within pinning range and then activating the non-contacting interfaces. The need for hazardous spacewalks or complex robotic operations to assemble large structures would be mitigated. These modular systems employ

interactions that ensure modules never touch one another, eliminating collision risks, while still maintaining basins of attraction that enable passive assembly processes.

Flux pinning also provides a technological means to depart significantly from traditional approaches to reconfiguration by treating modular, reconfigurable spacecraft as kinematic mechanisms. This proposal addresses the need for robust reconfiguration techniques in space without treating the problem of reconfiguration as one of docking or formation flight. In so doing, its approach incorporates passively stable physics, involving little to no active control at the level of the interface between modules and focusing on architectural control of the system start and end states.

Traditional approaches view autonomous modular system reconfigurations as problems in multi-vehicle feedback control [11], particularly as extensions of rendezvous and docking tasks [3,12]. However, this work suggests that spacecraft achieve reconfiguration without detaching from one another, by forming appropriate kinematic mechanisms. The degrees of freedom of these mechanisms lead to reconfiguration behaviors that are deterministic, in the sense that the spacecraft can be engineered such that the possible motions and configurations of the system are limited and a desired subset of the transitions between possible configurations becomes a stable reconfiguration sequence. This mitigates the risk of instability from extensive low-level active control, as actively controlled equilibria may not be trivial to define, create, identify, or exploit; in addition, the stable subset of transitions could be less susceptible to unmodeled dynamics or interactions between the controller and system dynamics. These systems also offer the potential advantage of low power and fuel consumption, saving spacecraft mass.

Fig. 1-1 shows a simple, CubeSat-based fractionated spacecraft assembled from such non-contacting modules. Each module is structurally identical, simplifying



*Fig. 1-1 A non-contacting, modular CubeSat spacecraft concept with a flux-pinned interface capable of action-at-a-distance six degree-of-freedom actuation.*

integration, test, and operations. This concept suggests spacecraft that form a non-contacting Stewart platform based on this principle. This configuration allows stable 6DOF actuation of close-proximity spacecraft modules. Depending on the design of the interface, this system may be assembled in any one of several different physical configurations and might even be capable of reconfiguring itself. The assembled spacecraft can change its inertia properties, realize new functionality, or restore damaged components through these reconfigurations. As a more specific example, stationkeeping and reconfiguration of sparse-aperture telescope formations are ideal applications of this type of non-contacting architecture, which allows both passive and active control of the modular components [13,14]. Another possibility is that many

small flux-pinned modules may form a solar sail with structure provided by massless magnetic fields [15].

## 1.2 The Physics of Magnetic Flux Pinning

Flux pinning is a phenomenon that arises from the unusual quantum physics of type II high-temperature superconductors (HTSCs). All superconductors completely repel weak magnetic fields because the fields excite supercurrent loops within the zero-resistance HTSC. The magnetic field generated by these supercurrents exactly opposes the applied field, causing the net field within the HTSC material to be zero; this repulsion is known as the Meissner effect [16]. However, type II HTSCs, such as yttrium barium copper oxide (YBCO), are laced with impurities that form sites where sufficiently strong magnetic fields, with flux density above a HTSC-specific critical value [17], penetrate the superconducting material. The applied magnetic field lines become trapped on these impurities in the HTSC; supercurrents excited by the applied field oppose any motion of the flux lines away from such “pinning” sites [16,18].

Flux pinning manifests itself macroscopically as a force on the magnetic field



*Fig. 1-2 A cylindrical permanent magnet (1.9 cm dia.) flux pinned with its center about 2 cm above the surface of a YBCO superconductor.*

source, such as a permanent magnet. After the field lines of the magnet are pinned, the superconductor effectively resists any change in the magnetic flux distribution within its volume. The supercurrent distribution exerts an electromagnetic restoring force and torque on the magnet. In general, this restoring force is nonlinear and hysteric: a levitated magnet can be moved away from the superconductor, brought back, and pinned in a new orientation [16]; furthermore, a pinned magnet experiences different forces depending on the direction of its motion and its distance from the superconductor [17,19]. However, an intuitive physical model for this interaction for small relative motions is a multiple-degree-of-freedom (DOF) spring and damper [17,20].

Many researchers have concentrated on flux-pinning stiffness as a mechanism to achieve magnetic levitation of objects in gravity [21,22], demonstrated by the permanent magnet levitated over a slab of superconducting yttrium barium copper oxide in Fig. 1-2. However, a particularly interesting property of this interaction is that flux pinning acts in any direction along which there is a magnetic field gradient. Thus, the magnet in Fig. 1-2, which has an axially symmetric field, is fixed not only in vertical translation but in every rigid-body degree of freedom except for rotation about its dipole axis. Furthermore, if moving flux lines travel across the superconductor, against the pinning effect, mechanical energy is damped in a powerful manner reminiscent of eddy-current damping. Thus, the flux-pinned connection is heavily damped against oscillation despite the low temperatures.

### 1.3 Technological Applications of Flux Pinning

Magnetic flux pinning has been studied at length by the scientific community for its applications to levitating objects in a 1g environment [16,21,22,23,24]. However, two features of flux pinning make it attractive for space applications. First, it is not subject to the limitations described by Earnshaw's Theorem. A consequence of this theorem is that a configuration of force sources that obey an inverse-square law (*e.g.*, gravitational, electrostatic, or magnetostatic forces) cannot be passively stable [25]. Active control is typically required when these forces are involved, as in the case of the Electromagnetic Formation Flight [26] and Coulomb Formation [27] concepts, which maintain spacecraft formations with magnetic or electrostatic forces, respectively. Instead, flux pinning involves the magnetic fields of supercurrents which depend on the motions of flux-pinned magnets without the input of active control. Flux pinning can create passively stable 6DOF equilibria [16,28] among multiple bodies in space with large basins of attraction. A large system of modules, such as a

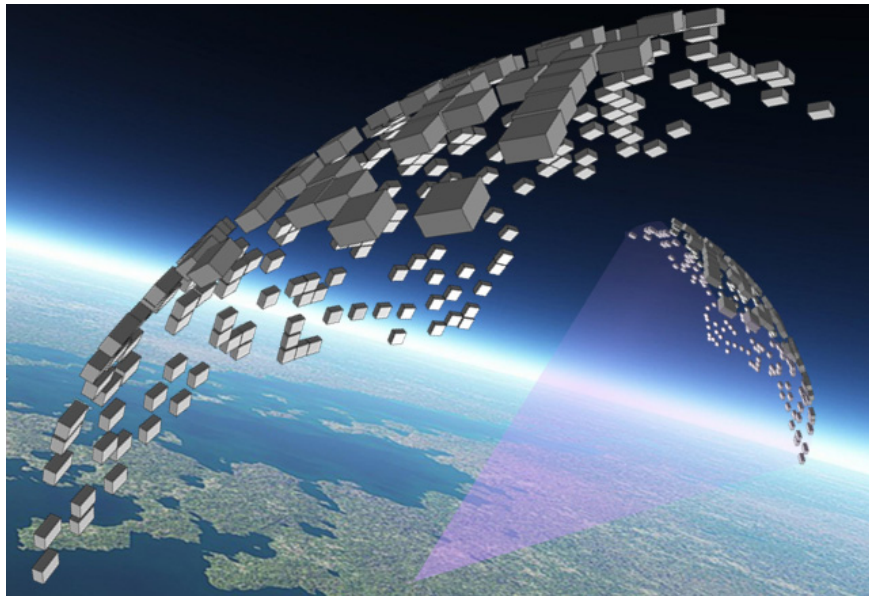


*Fig. 1-3 Reconfigurable optical mirrors assembled from modules with non-contacting interfaces.*

sparse-aperture telescope, could be assembled without the need for active control. For instance, Fig. 1-3 is meant to suggest a reconfigurable sparse-aperture telescope reflector that has been autonomously self-assembled from reflective modules and held in place by flux pinning. In addition, it is possible to establish a flux-pinning equilibrium at some initial separation distance and then change the properties of the pinned magnetic field to alter the equilibrium without breaking the non-contacting connection. This possibility enables control of the relative motion of flux-pinned modules, leading to articulated spacecraft [29] and spacecraft formations [30].

Second, this effect does not require power if the superconductor is passively cooled. As long as the HTSC material remains in its superconducting state (that is, below its critical temperature:  $T_c \approx 88$  K for YBCO), it pins magnetic flux. HTSCs may require power for cooling if they receive incident sunlight, however, depending on the local thermal environment, passive cooling may be sufficient: for example, the equilibrium temperature of the Spitzer Space Telescope is near 30 K, sufficiently low for flux pinning [31]. No voltage need be applied to the superconductor, and no actuation of the magnet is required. Therefore, loss of power and/or loss of command and data handling need not threaten the structural integrity of a system held together by this effect. In addition, flux pinning can be activated and deactivated by simply raising or lowering the temperature of the HTSC above or below  $T_c$  by, for example, opening and closing a sunshade. A permanent magnet flux-pinned to a superconductor experiences a restoring force that attracts it to the position and orientation it held when the superconductor cooled below its critical temperature. Thus, the modules' relative position and orientation before cooling become passive equilibria after cooling. Modules only need be moved within pinning range and their HTSC elements cooled to establish a stable equilibrium.

The hysteretic behavior of flux pinning also has important implications for the application of flux pinning to spacecraft station-keeping and modular assembly. First, linear models of flux-pinning force as a spring and damper are accurate only for small relative motions between the magnet and superconductor. Second, there is no single equilibrium for a specific magnet-superconductor pair. Rather, many different equilibria are possible depending on the history of the system (for instance, whether the superconductor was cooled with the magnet already at its desired equilibrium, or whether the magnet moved in from infinity after cooling) [16]. The versatility of such an interface to establish a wide range of equilibria also extends to HTSCs that exhibit little or no hysteresis. These subtleties may be effects that can be exploited rather than problems to be overcome.

Current approaches to autonomous docking of space vehicles [32,33], as well as spacecraft reconfiguration and formation flying [3,12,34], rely heavily on active controllers. However, the passive physics of magnetic flux pinning allow the development of technologies that may dramatically reduce the control effort required to execute these activities. Instead of modules precisely maneuvering into place under active control and making a mechanical connection (which might involve spacewalks, robot arm manipulations, fuel expenditure, or risks of mechanical failures), the flux-pinned components of the modules passively draw them into a stable basin of attraction. Furthermore, since the potential energy of a flux-pinned magnet and superconductor increases rapidly when the components move closer than their equilibrium separation, the physics of the interface contribute some passive collision avoidance during docking. After assembly, a flux-pinned, non-contacting structure then has several options for reconfiguration. For instance, modules can warm their superconductors to release each other and re-cool their superconductors to establish

new equilibria. Actively controlled electromagnetic fields can also be superimposed on the flux pinning interaction to bend or flex pinned modules with respect to one another, creating a non-contacting articulated structure [35].

## 1.4 Kinematic Reconfiguration Control Strategies

Spacecraft architectures capable of autonomous reconfiguration face a major hurdle in implementation: in-orbit reconfiguration of such modular spacecraft systems is a challenging problem in controls and dynamics. Often, proposed solutions to this problem involve a combination of multibody dynamics analysis, multivariable state feedback control strategies, docking hardware and algorithms, state estimation, and the relative orbital dynamics of formation flight, expressed as a tracking problem [2,3,11,12,34,36]. These approaches incorporate interactions between many vehicles, sensors, and actuators, and thus may be both computation- and power-intensive, with many potential points of failure. With the goal of adding robustness, determinacy, and power savings to the reconfiguration process, we propose that modular spacecraft designs include the capability to alter their kinematic properties. After each such alteration, the multibody system would evolve dynamically due to the presence of ambient forces in the space environment, such as gravity gradients, solar pressure, and planetary magnetic fields, towards a stable equilibrium. From this stable equilibrium, the multibody system can make further changes to its kinematics and passively evolve again. A reconfiguration maneuver in this framework is thus composed of a sequence of natural, dissipative motions towards passive equilibria of the multibody system. In this manner, spacecraft composed of many modules can execute complex but failure-robust reconfiguration maneuvers with little to no low-level control computation or

actuation. Any required computations can be performed offline with common multibody dynamics techniques, and operators on the ground can verify the system state while it is paused at any “safe step” intermediate equilibrium.

There is a parallel between this reconfiguration concept and mechanical deployments in which the potential energy provided by a spring causes a joint to move to a passive dynamic equilibrium. In general, such an approach to reconfiguration may apply to any modular spacecraft system in which kinematic joints link the modules; however, it is especially relevant to systems with modules already connected by force fields through one of several enabling technologies. Such systems include Coulomb-tether formations [27] and Electromagnetic Formation Flight [26], though these approaches involve active control strategies, reducing the benefits of reconfiguration through passive dynamics. In addition to actuation opportunities from time-varying magnetic fields such as those from electromagnetic coils, flux pinning provides an ideal opportunity for spacecraft reconfiguration via this kinematic-mechanism paradigm.

Shaping a magnetic field pinned to a HTSC introduces or removes stiffness, creating a reconfigurable, non-contacting, kinematic mechanism. Other shaping of the magnetic fields, along with exploitation of rigid-body dynamics, gravity gradient, and other ambient forces, may change the stability of the equilibrium points of these mechanisms. In addition, cooling and warming the superconductors is a means to toggle inter-module interfaces. Control of a reconfiguration maneuver for such a system therefore takes the form of specified magnetic field geometries at each interface, to introduce or stiffen appropriate kinematic degrees of freedom, with accompanying magnetostatic, electrostatic, gravitational, or Coriolis forces that cause the system to passively “fall” towards a desired equilibrium in configuration space.

Multiple steps between sequential equilibria allow the system to reach many possible configurations. In these non-contacting systems, spacecraft assembly can be executed as a similar sequence, with modules falling into 6DOF basins of attraction.

A simple non-contacting mechanism consisting of a single revolute joint on an air-table testbed has been demonstrated in a laboratory setting [37]. In 2009, members of the Cornell Space Systems Design Studio demonstrated a simple flux-pinned kinematic mechanism in a NASA microgravity program. The demonstrations, with CubeSat mockups, showed that flux pinning can be implemented on the nanosatellite scale and that vehicles equipped with flux-pinned interfaces can form non-contacting revolute joints, with stiffness in all but one degree of freedom. Future microgravity flights will demonstrate the autonomous assembly of flux-pinned systems and their robustness to sensing and control failures. Simultaneously, an air-levitated laboratory testbed currently in development will examine small satellite reconfiguration maneuvers and algorithms [37].

## 1.5 Overview and Contributions

This dissertation proposes a technological solution for passively stable autonomous assembly of multibody spacecraft and characterizes the physical properties and design principles of this technology. It develops a hybrid systems- and kinematics-based control strategy for passive, robust reconfiguration of modular spacecraft. Flux-pinning-based technology may enable the development of a reconfigurable, modular space system that is capable of self-assembling, integrating new components after its initial deployment, adapting itself to new mission roles, and

repairing damaged systems autonomously, all with the advantages of passive stability and a high tolerance to control failures. The major contributions of this work are:

1. A hybrid systems- and kinematics-based control strategy for passive, robust reconfiguration of multibody systems, in particular modular spacecraft.
2. A modeling approach to such systems that automatically discovers reconfiguration graphs, the design tools for kinematic reconfiguration.
3. Physical implementations of this theory based on the physics of magnetic flux pinning.
4. Characterization of the physical behaviors of flux pinning to inform system architecture principles.
5. Experimental validation of flux-pinned, reconfigurable systems at the nanosatellite scale.
6. A new approach to synthesis of equations of motion for multibody systems with quaternion attitude representations in the Udwadia-Kalaba framework.

Each chapter of this dissertation corresponds to a journal publication. Chapter 2 begins the experimental determination of design metrics for a flux-pinning interface. These experiments are concerned with the general problem of simultaneously characterizing the six-dimensional stiffness of a pinned magnet-superconductor system as functions of the relative positions of a magnet and superconductor, in quasistatic situations. These are the first simultaneous 6DOF measurements of flux-pinning stiffness. The algorithms and techniques developed in this experiment might be extended to performance-verification testing of flux-pinned modules for eventual space application.

The dynamic case, in which the relative motions of the flux-pinned magnet and superconductor are not constrained, is important to evaluate for spacecraft

applications. Chapter 4 describes a system-identification experiment to dynamically characterize the stiffness and damping of flux-pinned interfaces, and proposes means to precisely manipulate the interfaces with non-contacting force fields. The chapter also discusses models of the flux-pinning effect to correlate the experimental data and simulate new space systems.

Chapter 3 identifies some mathematical tools for treating reconfigurable spacecraft systems as kinematic mechanisms. This chapter develops its treatment in the particular context of a reconfigurable system utilizing flux pinning, but the kinematic mechanism concept may be extended to other architectures as well. It also provides some examples of spacecraft reconfiguration governed by kinematic mechanisms. The examples include descriptions of two reconfiguration sequences for changing the order and relative orientation of a line of modules, as well as an air-table demonstration of a simple FPI-based reconfiguration. This air-table demonstration led to a microgravity flight test of a flux-pinned system that demonstrated kinematic reconfiguration at the nanosatellite scale. Chapter 5 describes the microgravity flight test and its results.

The last chapter of this dissertation explores the kinematic reconfiguration concept in detail. It is a novel hybrid-control strategy that reconfigures multibody spacecraft from one shape to another in such a way that passively stable system dynamics enable both low control effort and a high degree of robustness. This approach treats reconfigurable spacecraft systems as multibody kinematic mechanisms with controllable kinematics and takes advantage of ambient force fields in the space environment (gravity gradient, magnetism, etc.) along with passively generated, non-contacting forces on the spacecraft (such as those from permanent magnets) to drive the reconfiguration maneuver to one stable dynamic equilibrium after another, in

sequence. The use of kinematic constraints and passive dynamics adds robustness, while the stepwise nature of the reconfiguration maneuver provides many safe-hold points for verification regardless of transient dynamics. The focus on kinematic constraints lends itself well to Udwadia and Kalaba's technique for generating equations of motion. Chapter 6 details the augmentation of the Udwadia-Kalaba equations with quaternion states and Euler's equation for fully 3D rigid body motions, as well as the development of a simulation environment and computational tools for exploring sequential-equilibrium reconfigurations.

## CHAPTER 2

### STIFFNESS OF A FLUX-PINNED VIRTUAL STRUCTURE FOR MODULAR SPACECRAFT

This chapter describes a quasistatic experiment designed to measure the stiffness of a flux-pinned magnet-superconductor pair simultaneously in all six rigid-body degrees of freedom. This experiment characterized flux-pinning stiffness as a function of the equilibrium distance between the magnet and superconductor. Other design parameters investigated in this chapter include the relative orientation of the components and the size of the flux-pinned permanent magnet. The material in this chapter has been previously published as “Stiffness of a Flux-Pinned Virtual Structure for Modular Spacecraft” in the *Journal of the British Interplanetary Society* [38].

## 2.1 Testing the Mechanical Properties of Flux Pinning

### 2.1.1 Static Experiment

The purpose of the experiment is to measure flux-pinning stiffness, the constant of proportionality between small displacements of the magnet relative to the HTSC and the restoring force exerted by flux pinning. The HTSC material consists of 19 hexagonal tiles of bulk melt-textured YBCO superconductor forming a roughly hexagonal plate approximately 11 cm in diameter and 1 cm thick. The entire assembly has flux-pinning performance comparable to that of a single sintered superconductor because the superconducting grains in the individual YBCO tiles are much smaller than the tiles. A slate tile (with a coefficient of thermal expansion similar to YBCO) epoxied to the superconductors provides structural rigidity. During the experiments, a

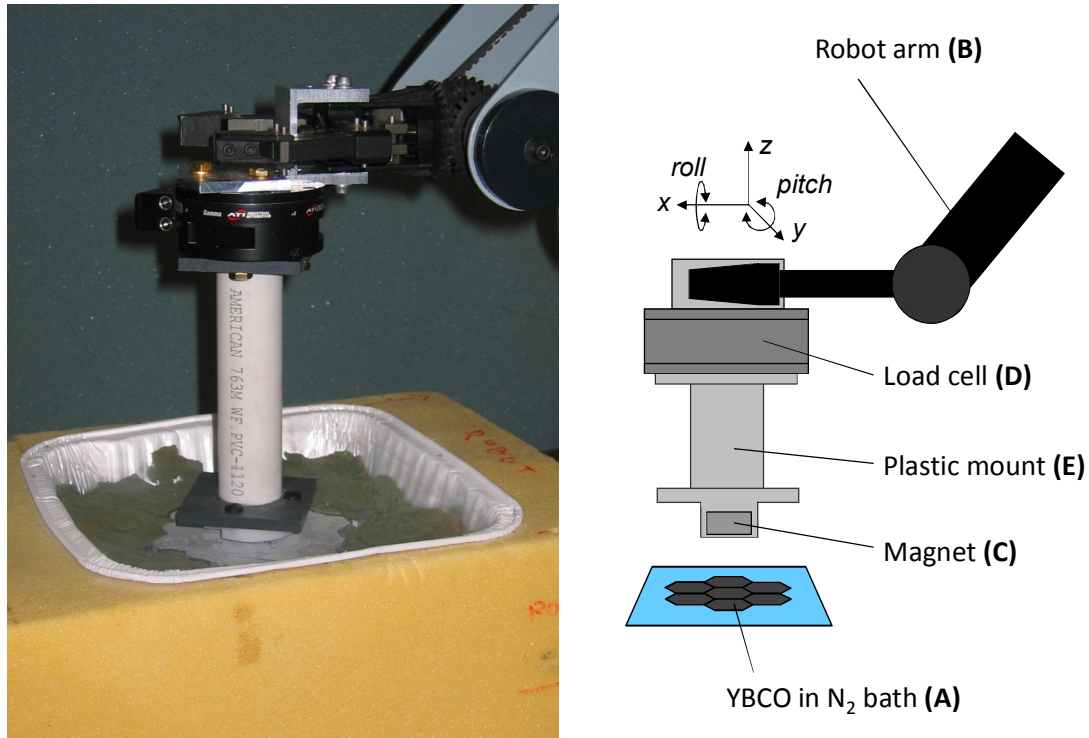


Fig. 2-1 Experimental setup with robot arm, load cell, permanent magnet, and superconductor.

liquid nitrogen ( $N_2$ ) bath cools the superconductors in an insulated container (A) as shown in Fig. 2-1. An Eshed Robotek Scorbot ER-V robot (B) moves a stack of one or more permanent magnets (C) relative to the superconductor. The end effector of the robot can displace in five degrees of freedom (translation in three dimensions along with roll and pitch rotations) [39]. The robot gripper holds an ATI Gamma load cell (D), with non-ferromagnetic components, capable of measuring forces and torques in 6DOF with resolution better than 1/80 N and 1/2000 N m, respectively. A rigid plastic enclosure (E) attaches an NdFeB permanent magnet(s) to this load cell far enough from the load cell surface to separate temperature-sensitive electronics from the nitrogen bath. In addition to the special load cell, the setup uses nonmagnetic components wherever possible to prevent the test equipment from interacting with the magnet and the superconducting plate.

The robot arm runs a program that takes the magnet through a series of small deflections in each of its five degrees of freedom from the initial equilibrium point. The uncontrollable sixth degree of freedom of the robot is nearly coincident with the magnet's axis of symmetry. Since the experiment uses a cylindrical magnet with an axisymmetric dipole field, flux pinning constrains all degrees of freedom of the magnet except for rotations about this dipole axis. Therefore, displacements in this degree of freedom are excluded from the experiment and have near-zero responses from restoring forces. Nevertheless, for completeness, each measurement records the full six-dimensional vector of the magnet's deflection. For each trial, the robot carries out ten discrete displacements: translations of 2 mm in both the positive and negative directions along  $x$ ,  $y$ , and  $z$ , followed by positive and negative rotations of  $3^\circ$  about the  $x$  and  $y$  axes. The flux-pinning interaction is effectively non-hysteretic for these small relative displacements. Forces exerted by the superconductor on the magnet are transferred to the load cell, which resolves them into a 6D measurement of the force and torque experienced by the magnet.

Repeated trials of this experiment measure variation in the 6D stiffness matrix as a function of three parameters: separation distance  $d$  between the magnet and the superconductor surfaces, tilt angle  $\beta$  of the magnet axis with respect to the superconducting plane normal, and the number of identical magnets  $N$  mounted on the load cell. Each point in this  $(d, \beta, N)$  parameter space is associated with a unique stiffness matrix. To prevent hysteretic effects, adjustments to these parameters take place only with the superconductor above  $T_c$ . Experiments occur with the YBCO in field-cooled (FC) conditions, which contrasts with zero-field cooling (ZFC) in which the superconductor cools in the absence of magnetic field and the magnet subsequently moves in from infinity [24]. In space applications, this situation may

reflect a case in which modules pre-load superconductors with magnetic flux to match the magnets in other modules before the corresponding module pairs approach one another. Another possibility is a system of modules that lock together by cooling their superconducting elements below  $T_c$  after they establish desired relative positions and orientations through other formation-flight approaches.

### 2.1.2 Static Model

When a superconductor cools in the presence of a permanent magnet with no external forces, the system is at equilibrium and the superconductor applies no appreciable force to the magnet. For small displacements of the magnet from this equilibrium, the flux-pinning force follows a non-hysteretic minor loop and appears as a linear restoring force [17,18,20]. The linear behavior of this force for small values of displacement  $|r|$  justifies the use of a 6DOF Hooke's Law model:

$$\mathbf{F}_{6 \times 1} = -\mathbf{K}_{6 \times 6} \mathbf{r}_{6 \times 1} \quad (2-1)$$

In Cartesian coordinates with small rotation angles, the six-dimensional generalized position and force vectors are,

$$\begin{aligned} \mathbf{r} &= [x \quad y \quad z \quad \theta_x \quad \theta_y \quad \theta_z]^T \\ \mathbf{F} &= [F_x \quad F_y \quad F_z \quad \tau_x \quad \tau_y \quad \tau_z]^T \end{aligned} \quad (2-2)$$

The magnet's position at the time of field cooling defines the origin of the coordinate system for  $\mathbf{r}$  so that both  $\mathbf{r}$  and  $\mathbf{F}$  are zero at equilibrium. The stiffness matrix is composed of four  $3 \times 3$  translational, rotational, and cross-coupling partitions:

$$\mathbf{K} = \begin{bmatrix} \mathbf{K}_{xx} & \mathbf{K}_{x\theta} \\ \mathbf{K}_{\theta x} & \mathbf{K}_{\theta\theta} \end{bmatrix} \quad (2-3)$$

A least-squares algorithm solves for the stiffness matrix  $\mathbf{K}$  in Eq. (2-1) from the displacement and force data. This 6D matrix equation takes the form

$$\begin{bmatrix} F_x \\ \vdots \\ \tau_z \end{bmatrix} = - \begin{bmatrix} k_{11} & \cdots & k_{16} \\ \vdots & \ddots & \vdots \\ k_{61} & \cdots & k_{66} \end{bmatrix} \begin{bmatrix} x \\ \vdots \\ \theta_z \end{bmatrix} \quad (2-4)$$

A straightforward approach to solving for the components of  $\mathbf{K}$  is to include  $n \geq 6$  pairs of displacement and force measurements as column matrices in this equation and multiply both sides by the right pseudoinverse of the matrix of positions:

$$\begin{bmatrix} F_{x1} & \cdots & F_{xn} \\ \vdots & & \vdots \\ \tau_{z1} & \cdots & \tau_{zn} \end{bmatrix}_{6 \times n} = - \begin{bmatrix} k_{11} & \cdots & k_{16} \\ \vdots & \ddots & \vdots \\ k_{61} & \cdots & k_{66} \end{bmatrix}_{6 \times 6} \begin{bmatrix} x_1 & \cdots & x_n \\ \vdots & & \vdots \\ \theta_{z1} & \cdots & \theta_{zn} \end{bmatrix}_{6 \times n} \quad (2-5)$$

$$\mathbf{K} = - \begin{bmatrix} F_{x1} & \cdots & F_{xn} \\ \vdots & & \vdots \\ \tau_{z1} & \cdots & \tau_{zn} \end{bmatrix} \begin{bmatrix} x_1 & \cdots & x_n \\ \vdots & & \vdots \\ \theta_{z1} & \cdots & \theta_{zn} \end{bmatrix}^+ \quad (2-6)$$

A MATLAB realization of Eq. (2-6) gives the flux-pinning stiffness matrix for the  $n = 10$  corresponding displacements carried out by the robot and force/torque measurements from the load cell at each  $(d, \beta, N)$  point. The algorithm enforces  $k_{66} = 0 \text{ N} \cdot \text{m/rad}$  stiffness about the magnet axis of symmetry and averages  $\mathbf{K}$  with  $\mathbf{K}^T$ .

## 2.2 Experiment Results and Discussion

The experiment parameters are  $N = 1$  at  $(d, \beta)$  points in the range  $d = 5 \text{ mm}$  to  $30 \text{ mm}$  and  $\beta = 0^\circ$  to  $20^\circ$ , and  $N = 2$  and  $3$  at three selected  $(d, \beta)$  points. Each point in this

three-dimensional parameter space yields a stiffness matrix. A representative stiffness matrix obtained from the static experiment is

$$\mathbf{K} = \begin{bmatrix} 101 & 13.5 & -14.3 & | & -0.08 & -1.84 & -0.03 \\ 13.5 & 75.4 & 18.8 & | & -1.73 & -0.47 & 0.00 \\ -14.3 & 18.8 & 196 & \text{N/m} & -0.81 & -0.16 & 0.01_{\text{N/rad}} \\ \hline -0.08 & -1.73 & -0.81 & | & -0.07 & -0.01 & 0.00 \\ -1.84 & -0.47 & -0.16 & | & -0.01 & -0.01 & 0.01 \\ -0.03 & 0.00 & 0.01_{\text{N-m/m}} & | & 0.00 & 0.01 & 0_{\text{N-m/rad}} \end{bmatrix} \quad (2-7)$$

Dashed lines indicate the  $\mathbf{K}_{xx}$ ,  $\mathbf{K}_{x\theta}$ ,  $\mathbf{K}_{\theta x}$ , and  $\mathbf{K}_{\theta\theta}$  partitions.

Several features of this matrix are readily apparent. First, the first three elements along the diagonal are large compared to the other elements in the matrix. These elements correspond to the proportionality between  $x$ ,  $y$ , and  $z$  displacements to  $x$ ,  $y$ , and  $z$  forces, respectively. These elements of the matrix should dominate the other elements in the  $\mathbf{K}_{xx}$  partition if the robot axes, superconductor surface, magnet axis, and load cell axes are well-aligned. In addition, these elements are consistent with the order of the nonzero elements of the  $\mathbf{K}_{\theta\theta}$  partition resulting from a model for the rotational stiffness about  $x$  or  $y$  consisting of two springs, with stiffness  $k_{33}$  and separated by the magnet diameter, connecting the magnet to the YBCO.

Second, the matrix is not diagonal and contains negative elements. If the robot coordinate axes are perfectly aligned with the load-cell axes, the plane of the superconductor, and the magnet's dipole axis, we expect a diagonal  $\mathbf{K}$  matrix. That is,  $\mathbf{K}$  should not couple orthogonal small displacements and their associated restoring forces. The presence of off-diagonal elements may indicate a misalignment in the experimental setup. However, the misalignment is small as the diagonal elements of the matrix are numerically close to its eigenvalues (with less than 5% disagreement in

the diagonal of  $\mathbf{K}_{xx}$ ). The robot is also a likely source of error since its rated position repeatability, approximately 0.5 mm, is about 25% of the displacements commanded; its angular repeatability is rated at  $1^\circ$ , one third of the commanded displacements [39]. Such errors in repeatability may also explain the negative stiffness matrix elements.

Third, the element  $k_{11}$  is not close to  $k_{22}$  in magnitude. By symmetry, these elements should be equal: the restoring force resulting from a lateral displacement of the magnet over the superconductor should not depend on the direction of the lateral displacement if the superconductor behaves uniformly. (That is, the situation should be close to axial symmetry.) Indications are that the YBCO is sufficiently uniform: rotating the YBCO plate  $90^\circ$  from its standard orientation in the experiment does not cause the values of  $k_{11}$  and  $k_{22}$  to switch positions, as should be the case if the YBCO

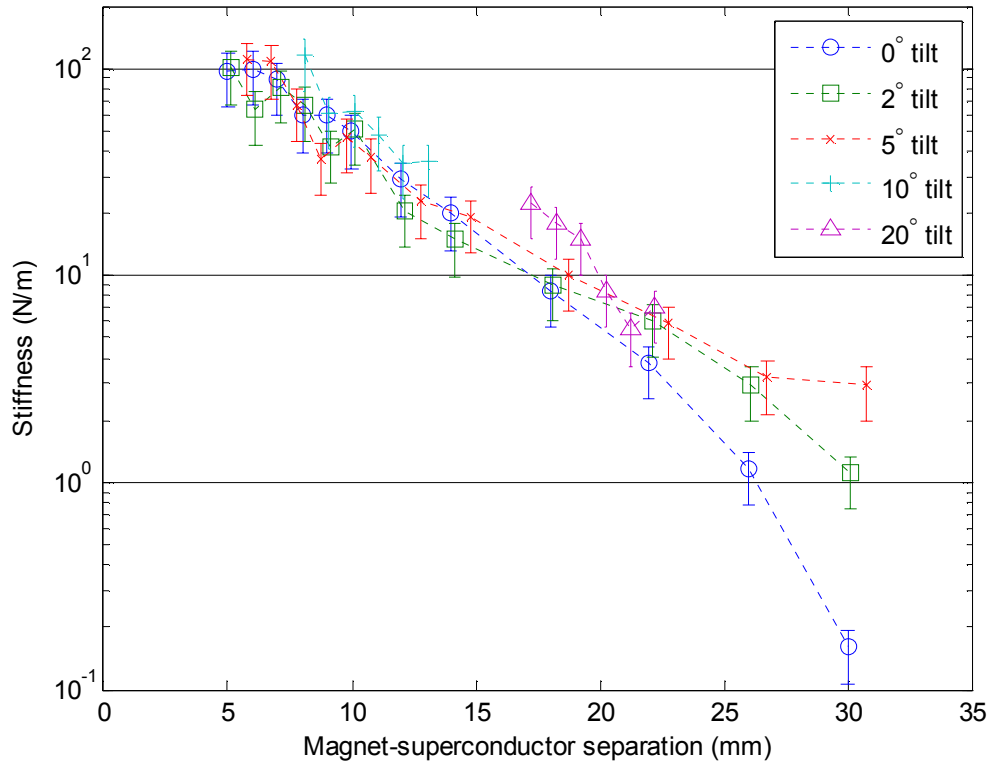


Fig. 2-2  $k_{11}$  ( $x$  translation stiffness) versus separation distance  $d$  for several magnet tilt angles  $\beta$ .

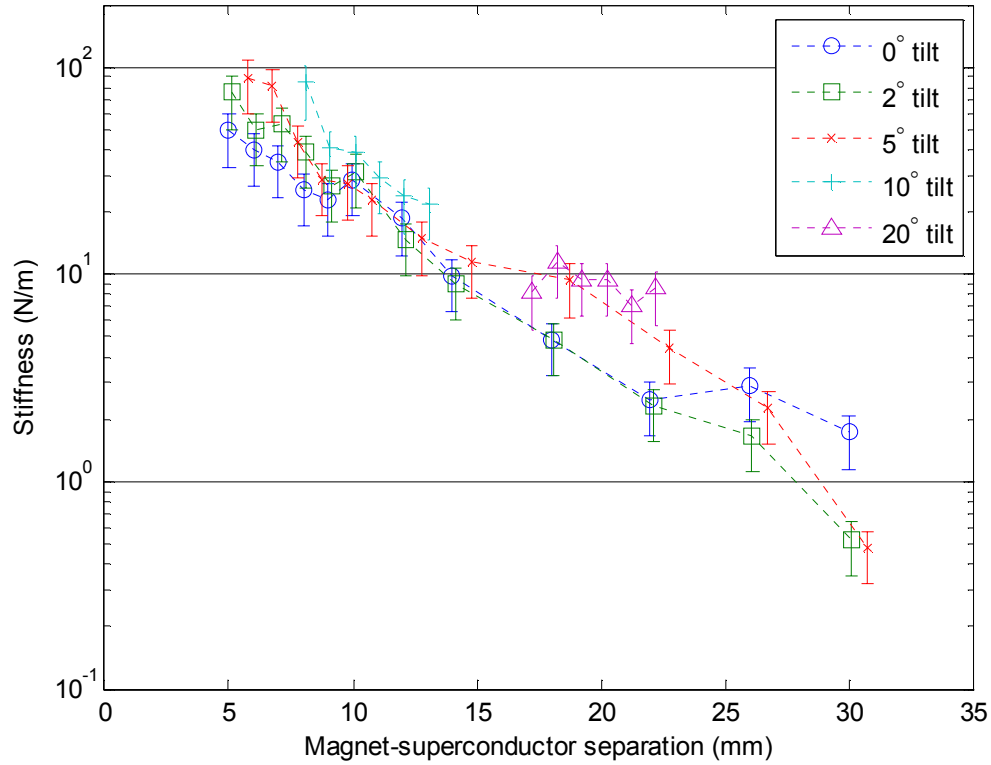


Fig. 2-3  $k_{22}$  ( $y$  translation stiffness) versus separation distance  $d$  for several magnet tilt angles  $\beta$ .

imposes some directionality on the flux-pinned interaction. The stiffness matrix similarly does not depend on the orientation of the magnet with respect to the load cell or the load cell with respect to the robot arm. Therefore, the asymmetry between  $k_{11}$  and  $k_{22}$  is also likely due to nonuniformity in small displacements of the robot arm in the  $x$  and  $y$  directions or some bias in the load cell calibration. Other investigators have found, both theoretically and experimentally, that  $k_{33} = 2k_{22} = 2k_{11}$  [24,40]. In this experiment,  $k_{11} \approx \frac{1}{2}k_{33}$  whereas  $k_{22}$  does not obey this relationship. Since the disparity between  $k_{11}$  and  $k_{22}$  is likely an artifact of the experimental setup,  $k_{11}$  may be the more accurate measure of lateral stiffness.

The diagonal elements of the stiffness matrix show clear trends as the experimental parameters vary. According to the theory developed by Johansen and

Bratsberg [28], the restoring force for displacements in a lateral direction (i.e., along  $x$  or  $y$ ) decays approximately exponentially as the separation  $d$  increases. Johansen et al. [41] also conducted experiments that showed that the stiffness for small displacements in  $z$  falls off as the height of a magnet over a superconducting thin film increases. Data from this experiment are consistent with these observations. Rotational stiffnesses

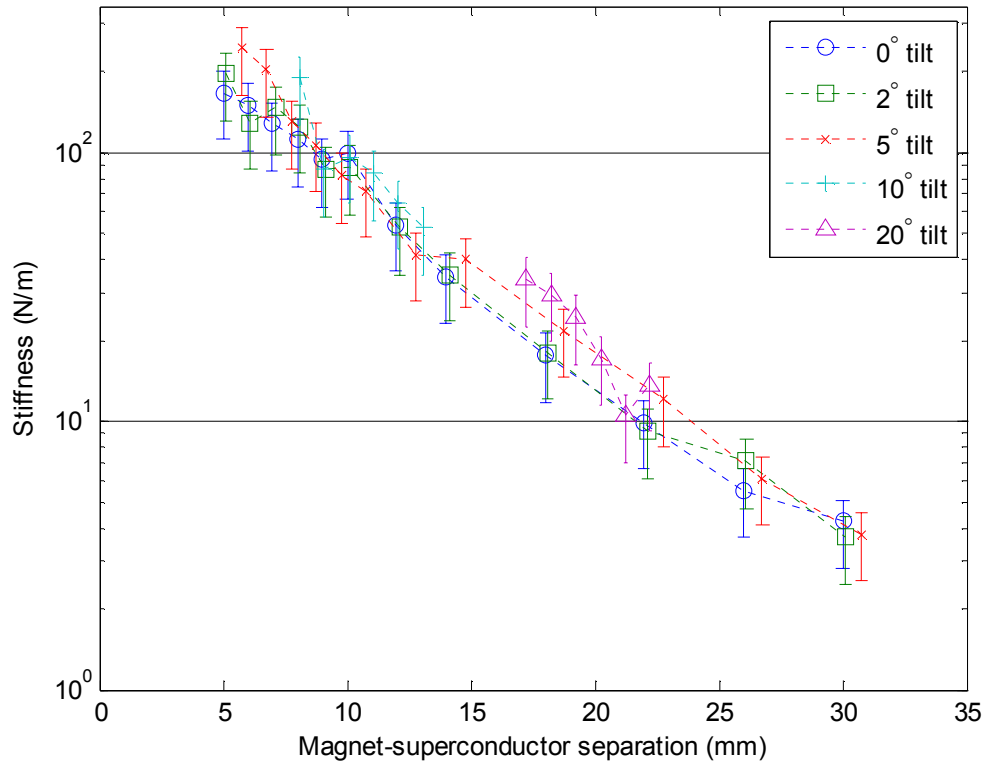


Fig. 2-4  $k_{33}$  ( $z$  translation stiffness) versus separation distance  $d$  for several magnet tilt angles  $\beta$ .

should also fall off with increasing  $d$ . High rotational stiffness is very desirable if non-contacting modules are to remain fixed relative to one another.

Fig. 2-2 through Fig. 2-6 reveal the dependence of the diagonal elements of  $\mathbf{K}$  on initial field-cooling separation distance  $d$  for several values of tilt angle  $\beta$ . Consistent with the other work in this area, both the lateral and axial translational stiffnesses fall

off as the magnet-superconductor separation increases.  $k_{11}$  through  $k_{33}$  appear to exhibit exponential decay. The calculations by Johansen et al. [41] suggest that  $k_{33}$  should depend on  $d$  in a more complex way, but the discrepancy is most significant at smaller values of  $d$  than this experiment measured.

The drop in flux-pinning stiffness with separation distance imposes a limit on the possible separation between two flux-pinned modules in a space system. When fitted to an exponentially decaying function  $k_{ii} = k_{i0}e^{-d/d_0}$ , all the curves in Fig. 2-2 through Fig. 2-6 have  $1/e$  decay scales on the same order, ranging from  $d_0 = 2.8$  mm to 6.5 mm. Each of the translational stiffnesses in  $\mathbf{K}_{xx}$  therefore falls off by a similar factor for a given increase in separation. In microgravity, a relatively small stiffness may be all that is necessary to pin together two modules, if agility is not required. An

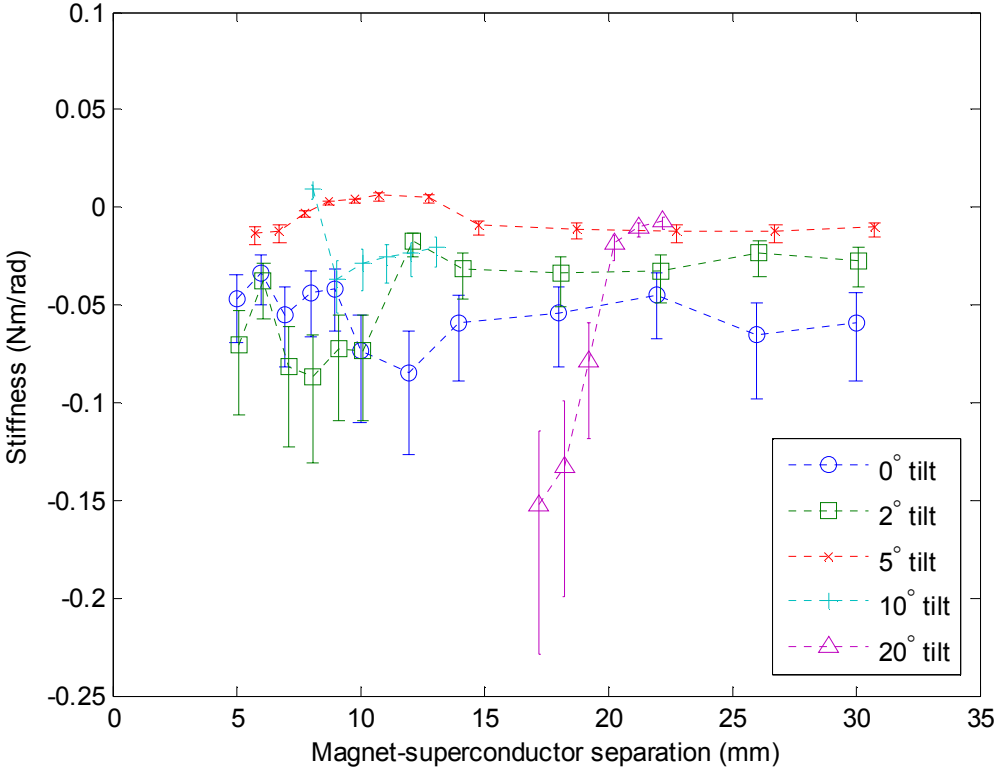


Fig. 2-5  $k_{44}$  ( $\theta_x$  rotation stiffness) versus separation distance  $d$  for several magnet tilt angles  $\beta$ .

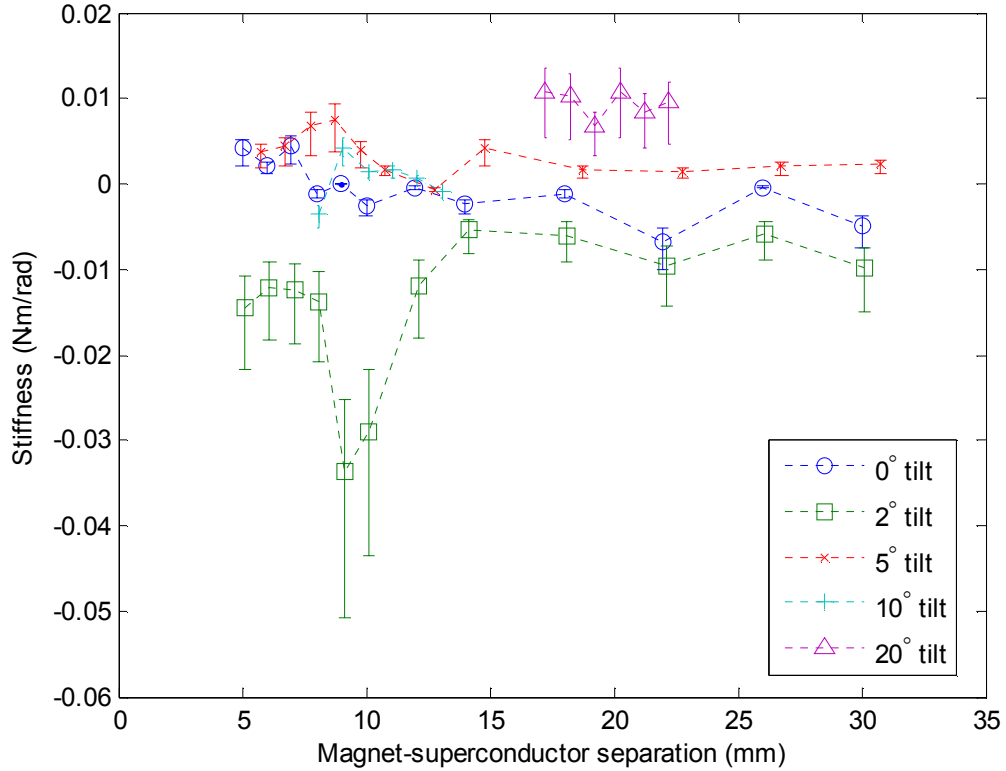


Fig. 2-6  $k_{55}(\theta, \text{rotation stiffness})$  versus separation distance  $d$  for several magnet tilt angles  $\beta$ .

interface comparable to the magnet and YBCO used in this experiment might allow inter-module separations of two to three centimeters or more.

The measured rotational stiffness coefficients  $k_{44}$  and  $k_{55}$  do not exhibit clear trends with separation distance. In fact, the measured rotational stiffness data have too much scatter to unambiguously characterize  $\mathbf{K}_{\theta\theta}(d, \beta)$ . This scatter may be due to angular imprecision in the robot. However, as design parameters, the elements of  $\mathbf{K}_{\theta\theta}$  may not be as important as the diagonal elements of  $\mathbf{K}_{xx}$  since a system of modules linked by magnets and superconductors will likely involve several flux-pinned pairs. Appropriate arrangements of these pairs can produce much larger rotational stiffnesses than those from a single magnet.

Increasing the dipole moment of the magnet, by increasing the parameter  $N$ , scales up the stiffness coefficients. Fig. 2-7 shows data from Fig. 2-2 with points for  $N = 1, 2,$  and  $3$  at  $d = 10, 18,$  and  $30$  mm superimposed. The points at these three heights sketch the exponential decay curve for each value of  $N$  and clearly show that an increase in magnetic field strength increases the stiffness  $k_{33}$ . The  $1/e$  decay scale of an exponential fit to these data remains approximately the same with varying  $N$ , ranging from  $5.8$  mm to  $7.7$  mm. A similar relationship holds for both  $k_{11}$  and  $k_{22}$ . We note that as  $N$  increases much beyond  $3$ , the permanent magnet's field deviates significantly from that of a dipole.

Since the flux-pinning interaction we wish to exploit depends on the magnetic field penetrating the superconductor volume, a likely metric for evaluating the

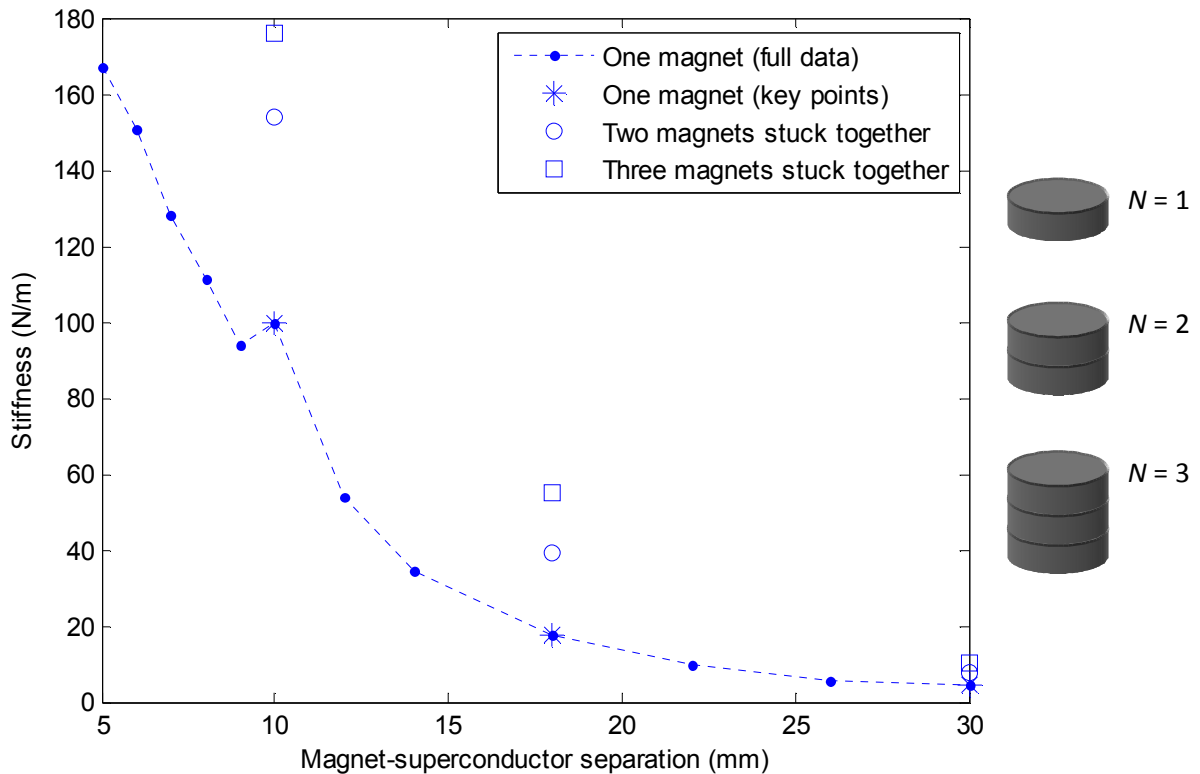


Fig. 2-7  $k_{33}$  (relating  $z$  to  $F_z$ ) versus separation distance  $d$  when a number of identical permanent magnets was stacked into a longer cylinder ( $N = 1, 2,$  and  $3$ ) at tilt  $\beta = 0^\circ$ .

combined effect of  $d$ ,  $\beta$ , and  $N$  on  $\mathbf{K}$  is the magnetic flux density projected across the interface into the superconductor. A gaussmeter measured the flux density at a point on the YBCO surface directly beneath the magnet for each  $(d, \beta, N)$  set in the experimental parameter space. When all the data for, e.g.,  $k_{33}$ , is plotted against the corresponding flux densities, a definite correlation is apparent (Fig. 2-8). This relationship, if well characterized, may provide a useful metric for evaluating the stiffness of an arbitrary arrangement of magnets pinned to superconductors. It is particularly useful for simulation and design: if stiffness is quantifiably related to the flux density in the superconductor volume, existing magnetic field modeling software can optimize a flux-pinned interface without the need to simulate microscopic current flows or quantum phenomena in the superconductor. A linear fit seems to match these

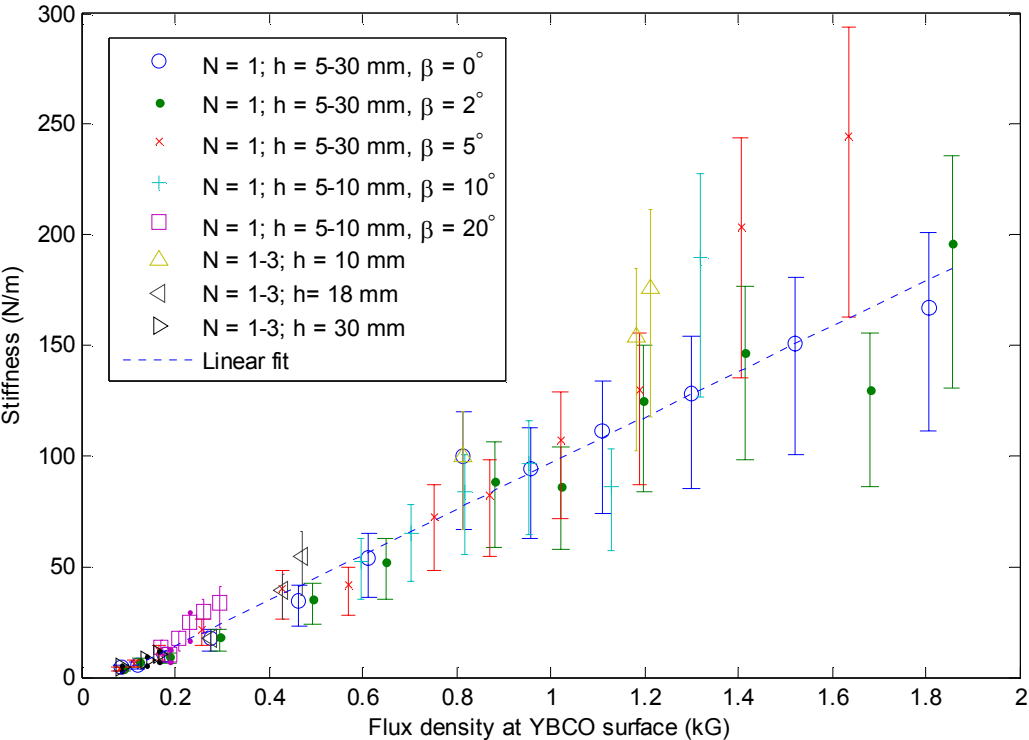


Fig. 2-8 Stiffness  $k_{33}$  (relating  $z$ ,  $F_z$ ) versus measured flux density over all experimental trials.

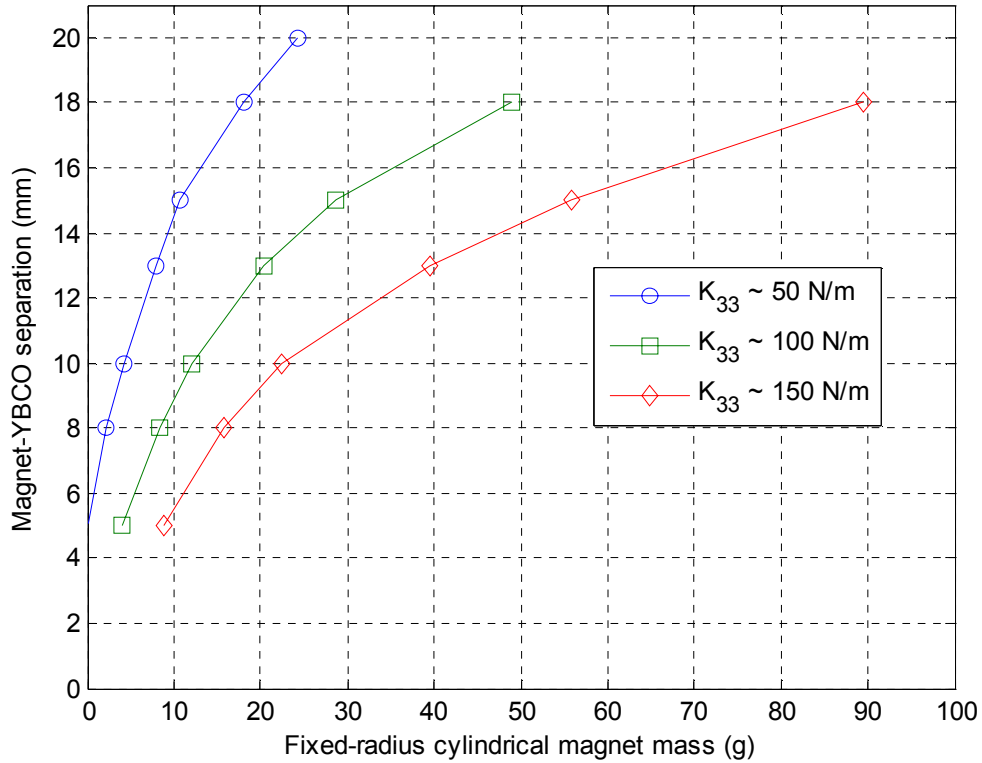


Fig. 2-9 Contours of fixed stiffness for desired module separation as a function of the mass of the magnet necessary to achieve that stiffness.

data quite well for fluxes below  $\sim 1$  kG, but at higher flux densities, the stiffness exhibits much more scatter. Further investigations will allow better characterization of flux-pinning stiffness at higher magnetic fields.

It is highly encouraging that at flux densities near 0.1 kG, flux-pinned stiffness is approximately 3.5 N/m. The minimum magnetic field strength necessary for flux pinning to occur is on the order of 0.1 kG for many high-temperature superconductors [16]; so a flux-pinned virtual structure of space modules equipped with superconductors and magnets comparable to those in this experiment will have a minimum stiffness of several newtons per meter regardless of inter-module separation, provided that sufficient flux reaches the HTSC to establish pinning. This stiffness may

be sufficient to maintain the shape of a modular space structure. For example, maintaining a formation consisting of two 1 kg modules in geosynchronous orbit and separated in the out-of-plane direction by 3 cm requires balancing gravitational forces with a force of approximately  $2 \times 10^{-8}$  N [29]. Introducing a modest stiffness of 1 N/m—less than the stiffness measured in this experiment for a 3 cm separation—gives a restoring force of this magnitude when the modules deflect from the desired separation by less than one part in  $10^7$ . The passive system may be augmented with integral feedback control, possibly actuated with electromagnets, to compensate for this steady-state error; choosing a different equilibrium separation for the flux-pinned “spring” binding the formation together could eliminate this bias passively, at least to the extent that the system’s parameters are known.

As a step toward establishing design criteria for flux-pinned modular spacecraft, this flux-to-stiffness relationship allows an estimate of the permanent magnet mass necessary to maintain two modules at some arbitrary separation distance and desired stiffness. Numerical simulation of magnetic fields provides a relationship from flux density to magnet mass for a magnet of fixed radius (0.95 cm, matching the magnet in these experiments) and arbitrary height. Fig. 2-9 shows the resulting mass, holding  $\beta = 0^\circ$  such that only  $d$  and  $N$  determine the flux density. This figure is promising for the concept of flux-pinned modules: at small separations (5 mm), stiffnesses as high as 150 N/m can be attained with less than 10 g of the spacecraft bus devoted to magnets for the flux-pinned interface hardware. Fig. 2-9 also suggests that a magnet twice the size of the one in our experiments could easily achieve separation distances of 2 cm or more; that connection could have stiffness close to 50 N/m. This experiment does not clearly establish a limit on the range of a flux-pinned connection of this geometry: the

contour  $k_{33} \approx 150$  N/m may be approaching an asymptote near  $d = 2$  cm, but the  $k_{33} \approx 50$  N/m line is not obviously approaching a particular value of  $d$ .

The assumptions about magnet size and shape that led to Fig. 2-9 have other interesting implications. The figure applies only to a single magnet of radius 0.95 cm, where magnet mass (and thus flux density) is increased by increasing the length of the magnet. This arrangement is likely not the optimal one for maximizing flux density in the superconductor volume over the indicated separation distances. A more complicated array of magnets might allow much higher stiffnesses for fixed separation and magnet mass than Fig. 2-9 suggests. (Alternatively, an optimally distributed configuration of magnets might allow much larger separation distances than those displayed in the figure for fixed stiffness and magnet mass.) If there are asymptotic limits to the separation distance achievable for a given magnet size and stiffness, we may be able to optimize the magnet and superconductor shapes to increase those limits.

## 2.3 Chapter Conclusions

Magnetic flux pinning exhibits many desirable properties for space-environment applications. It is a non-contacting force that is not subject to the limits of Earnshaw's Theorem, and is a property of the bulk material of Type II superconductors. Therefore, modular or formation-flying spacecraft systems coupled by magnet-superconductor pairs can be subject to stable restoring forces and damping without the need for active control or mechanical contact. While actuation of such interfaces is possible, it is not necessary to maintain the shape of the virtual structure holding a modular spacecraft system in place.

The experiments discussed here provide insight into trends of the 6DOF properties of magnetic flux pinning. These trends are consistent with previous investigations, which characterized flux-pinning stiffness in one to three degrees of freedom. The stiffness of the pinning interaction decays approximately exponentially with the separation between the two components at the time of field cooling. Furthermore, translational stiffnesses parallel and perpendicular to the plane of the superconductor obey the simple relationship that the restoring force for displacements normal to the superconductor surface is twice that for equal displacements parallel to it. An important distinction between this work and that of other authors is that many other researchers are interested in flux pinning for its application to superconducting bearings and magnetic levitation systems, both of which are levitation effects in a 1g environment, while this research envisions flux pinning as an enabling technology to maintain modules in 6DOF equilibrium in zero gravity.

The experiments reported in this chapter also demonstrate a potential means of performance verification for flux-pinned modular systems. Simultaneous measurements of the force and torque vectors acting on a flux-pinned module pair in response to small, well-known position and orientation displacements allow computation of the full 6DOF stiffness matrix  $\mathbf{K}$ . The 36 entries in  $\mathbf{K}$  (or its eigenvalues) may then serve as performance metrics for the system. Such tests will require much more precise knowledge of the displacements than the experiments reported here. Still, this quasistatic technique may prove useful for verification of flux-pinning flight hardware.

The data reported in this chapter indicate that the interaction may be effective across an inter-module separation of at least several centimeters. However, higher stiffness is desirable for robustness of the passive structure and may require module

separations under a centimeter for magnets and superconductors comparable to those described in Section 2.1.1. One line of inquiry for future work is to characterize the stiffness-to-flux-density relationship of Fig. 2-8 for other types and arrangements of superconductors. Some kinds of superconductors, such as single-domain YBCO, show evidence of flux pinning at enhanced separations of 6 to 7 cm.

While not suitable for the meters- to kilometers-wide separations involved in traditional formation flight systems, flux pinning provides an ideal platform for non-contacting modular systems. Modules could be assembled and connected, as if by a truss or mating adapter, without coming into physical contact. Simply maneuvering the modules into coarse proximity with one another will form a stiff mechanical configuration without power, active control, or the environmental interactions normally associated with attitude control and propulsion. The concept eliminates plume impingement, momentum build-up, and control/structure interactions that adversely affect large systems to be assembled in orbit, such as the International Space Station. These effects make fractionated spacecraft with flux-pinned virtual structures easier to boost into space and mate than modular spacecraft connected in orbit by mechanical means.

Future research will concentrate on developing design criteria for a viable space system using this effect. The results shown in Fig. 2-8 inspire two lines of inquiry. First, optimizing the shape and distribution of the magnets in a flux-pinning interface may maximize the flux density in the corresponding superconductor. Optimizing the shape of the superconductor to enclose a volume of maximum flux may achieve a similar effect. Second, experimental investigations of stiffness at high flux densities will shed light on the behavior of the contours in Fig. 2-8 as magnet strength increases. These investigations will determine how far the effective range of flux pinning may

extend, which has strong implications for the feasibility of this technology for such spacecraft architectures as sparse-aperture telescopes or formation flight missions.

The damping properties of a flux-pinned interface are also important to the dynamics of a non-contacting structure. Even brief laboratory experience with flux pinning is sufficient to conclude that damping can be quite high: if perturbed, a magnet levitated as in Fig. 1-2 oscillates for fewer than a dozen periods before settling. A new experiment treating the flux-pinned magnet-superconductor pair as a dynamic system is necessary to determine the damping ratio and how it varies with the parameters investigated in this work.

Another potentially useful line of investigation is to explore the effects of electromagnets on 6DOF flux pinning. For instance, an electromagnet near a flux-pinned pair might be used to actuate the interface by affecting the distribution of magnetic fields in the system. In addition, an electromagnet of sufficiently high strength could itself be flux-pinned rather than a permanent magnet. Altering the field of a flux-pinned electromagnet by tuning its current might produce effects on the stiffness, damping, and equilibrium separation of the flux-pinned interface, allowing another means of actuation. Coupled with the hysteretic nature of flux pinning, this actuation provides a possible avenue for reconfiguration of non-contacting modular systems. Reconfiguration could also be enabled by exploiting the thermal requirements of superconductivity to turn a flux-pinned interface “on” and “off” by controlling the temperature of the superconductor.

We envision flux-pinned interfaces becoming a standard component of future, modular spacecraft architectures. The scope of potential applications ranges from next-generation mating adapters that align modular components in a robust and safe way prior to final docking to large, segmented arrays of telescopes or instruments held

in place by a flux-pinned virtual structure. Manipulator arms that grasp payloads without contacting them, eliminating the need to find or design any mechanical attachment points on the payload, may also be a near-term outcome of this research. Farther in the future, it is possible that arrays of flux-pinned modules could form a truss-like substrate for even larger assemblies, allowing flux pinning to become an important structural technology for of large orbiting satellites and stations. With the mechanical properties of flux-pinned interfaces in hand, the development of design parameters for such next-generation systems can begin.

## CHAPTER 3

### RECONFIGURABLE SPACECRAFT AS KINEMATIC MECHANISMS

This chapter proposes the concept that flux-pinned interfaces, or other devices connecting spacecraft modules to one another, may form kinematic joints and mechanisms. These mechanisms govern the dynamics of reconfigurable space systems. Control strategies for reconfigurations of such systems consist of a specified sequence of joint kinematics. This chapter highlights the concept of kinematically governed reconfiguration maneuvers and introduces some of the mathematics that can analyze these maneuvers. It originally appeared as the note “Reconfigurable Spacecraft as Kinematic Mechanisms” in the *Journal of Spacecraft and Rockets* [42].

#### 3.1 Reconfiguration Mechanisms

The key concept motivating this approach is that spacecraft reconfiguration may be achieved through a combination of kinematics and passive dynamics by deterministically defining physical equilibria to prescribe a stable sequence of configurations. That is, rather than a feedback control law driving a spacecraft system from one configuration to another based on a state-error estimate, the spacecraft system incorporates a sequence of kinematic constraints that permit only reconfiguration to the desired end state. This process opens up the possibility of passive reconfiguration, where active control or power inputs are not required. Instead, a modular spacecraft may obtain the energy it needs to reconfigure from ambient forces such as gravity gradient or small perturbations of the spacecraft momentum. If the mechanism imposes an appropriate set of kinematic constraints, the spacecraft may even reconfigure to a desired end state by virtue of torque-free, rigid-body motions.

An incidence matrix consisting of 0, 1, and -1 entries describes connectivity among the elements of a multibody system, based on the graph structure of the system [43]. Each column corresponds to a joint, with zeroes in all entries except those rows corresponding to the bodies connected by this joint. For a modular system with a tree structure connected by flux-pinned interfaces, the incidence matrix takes the form

$$S = \begin{matrix} & u_1 & u_2 & \dots & u_a & \dots & u_n \\ S_0 & +1 & 0 & \dots & 0 & \dots & 0 \\ S_1 & -1 & \delta_2^1 & \dots & \delta_a^1 & \dots & \delta_n^1 \\ \vdots & \vdots & \vdots & & \vdots & & \vdots \\ S_i & 0 & \delta_2^i & \dots & \delta_a^i & \dots & \delta_n^i \\ \vdots & \vdots & \vdots & & \vdots & & \vdots \\ S_n & 0 & \delta_2^n & \dots & \delta_a^n & \dots & \delta_n^n \end{matrix} \quad (3-1)$$

$S_0, \dots, S_n$  designate each body in the system (where  $S_0$  is a fictitious base body) and  $u_1, \dots, u_n$  designate the joints linking each body. We introduce the symbol  $\delta_a^i$ , which suggests the Kronecker delta function, in place of constant matrix entries. These entries are parameters specifying the activity state of the flux-pinned interface represented by joint  $a$ . With the exception of the  $S_0$  row and  $u_1$  column, the incidence matrix of an FPI-linked system is generally filled with these parameters. If interface  $u_a$  links body  $S_i$  with  $S_j$ , then the parameters in column  $a$  take the values

$$\begin{aligned} \delta_a^i &= -1 \\ \delta_a^j &= +1 \\ \delta_a^k &= 0, k \neq i, j \end{aligned} \quad (3-2)$$

For  $n$  bodies with pinning interfaces, there are  $n^2$  such parameters, representing the potential for a flux-pinned interface to connect any two bodies and to reconfigure the incidence matrix. Of course, some of the theory of multibody kinematics [43] requires that the  $n \times n$  submatrix of  $S$  formed by deleting the  $S_0$  row be nonsingular. Therefore, if any entire column  $\delta_a^{1, \dots, n}$  becomes zero, the matrix  $S$  must be split into two

nonsingular partitions and treated separately. Physically, this case corresponds to a modular structure split in two. The two sub-structures then experience no constraint forces or torques from each other.

The incidence matrix describes only whether pairs of modules are connected, not the kinematic relations governing each joint. We must further specify the kinematics with the multibody spacecraft mechanism Jacobian  $J$ .  $J$  is a function not

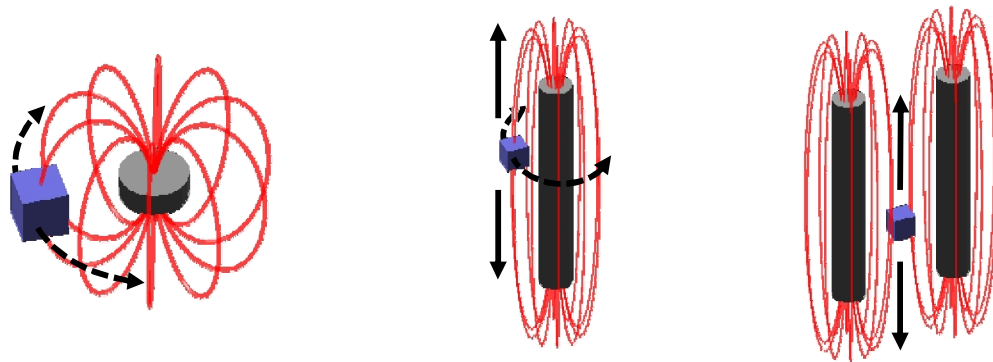


*Fig. 3-1 Flux-pinned joints with one or more degrees of freedom. Arrows indicate unconstrained motions of the superconducting cube. Left to right: revolute joint, cylindrical joint, and prismatic joint.*

only of the FPI connectivity parameters  $\delta_a^i$ , but also of the particular geometry of each FPI. Flux-pinned interfaces can form joints because flux pinning constrains only those DOFs aligned with nonzero magnetic field gradients. Thus, a cylindrically symmetric magnetic field source (such as a pure dipole, solenoid, or cylindrical permanent magnet) flux-pinned to a superconductor is free to rotate about the axis of symmetry in its field. Fig. 3-1 illustrates three possible joints based on this principle. Other joints are possible, derived from any magnetic field distribution with one or more coordinates along which the field gradient is zero. This requirement on magnetic field distribution suggests one way to lock and release selected DOFs in a flux-pinned joint without disengaging the interface thermally: electromagnets may simply toggle on and

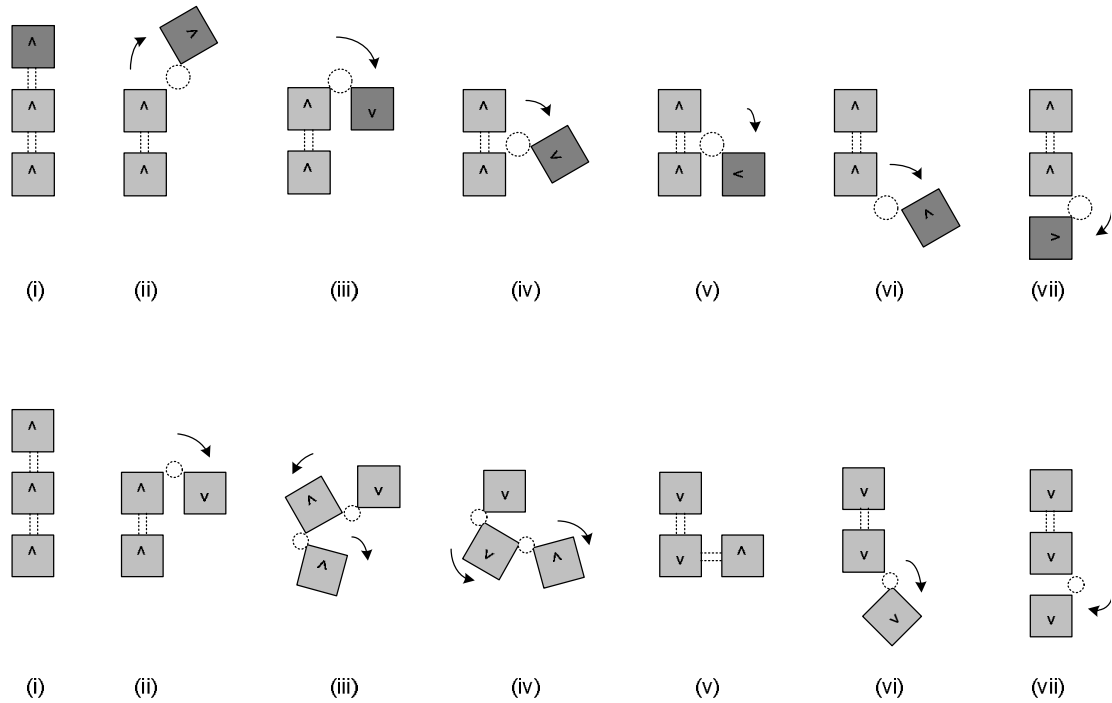


Fig. 3-2 Reconfiguration of a linear chain of modules by kinematic mechanism formation. Dashed double lines represent fully constrained FPIs and dashed circles represent FPIs with one rotation DOF. (top) walking reconfiguration and (bottom) Jacob's-ladder reconfiguration.

off to introduce or remove a field gradient. Other joints may not be affected by the changing field if they are beyond the minimum range for flux pinning (Chapter 4).

## 3.2 Example Applications

Three simple examples illustrate some capabilities of spacecraft reconfiguration via kinematic mechanisms. The first two (Fig. 3-2) demonstrate how appropriate selection of FPI degrees of freedom may change the physical structure of a modular system. In these cases, the initial configuration consists of a series of square cross-section modules arranged in a line (Fig. 3-2(i), top and bottom). A *walking* reconfiguration moves a module from one end of the line to the other, depicted schematically in the top half of Fig. 3-2. The target module (with darker shading in the figure) turns its fixed FPI into a hinge and “walks” down the line by successively

switching the interface that forms the hinge. When the target module changes its interface from a fixed one to a hinge, as it does between stages (i-ii), it alters its Jacobian. Similarly, changing the location of the hinge between stages (iii-iv) and (v-vi) involves a new choice of FPI parameters  $\delta_a^i$ , altering  $S$ . The remaining modules in the system need not change their kinematic properties. Although this example involves only three modules, it can easily be generalized to “walk” a module along an arbitrarily long (or arbitrarily shaped) chain. This idea may be extended to the creation of related machines, such as gears and screws.

A more involved reconfiguration of a three-module chain appears in the bottom row of Fig. 3-2. This is a *Jacob's-ladder* reconfiguration, which does not change the order of modules in the chain but rotates each  $180^\circ$  about an axis perpendicular to the chain. It involves more control over the flux-pinned joints in the formation, with both  $J$  and  $S$  changing simultaneously at some stages in the process and multiple FPIs concurrently releasing a DOF. Reconfiguration begins with one module on the end of the chain hinging as in a walking reconfiguration. This module then becomes the pivot for reconfiguration (ii). The remaining modules rotate such that a new module takes the pivot position (iii-iv). Again, this reconfiguration maneuver generalizes to systems with  $n > 3$ . The last module in the chain hinges to restore the original shape of the system, with each module individually rotated about its center (vi-vii). Momentum actuators could drive either of the reconfiguration processes in Fig. 3-2.

The third example is a demonstration of the non-contacting hinge concept with 3DOF mock-up modules on an air table. The FPI on the demonstration modules of Fig. 3-3 has a simple design: a YBCO superconductor immersed in a small nitrogen bath is on the corner of one module and a cylindrical NdFeB rare-earth permanent

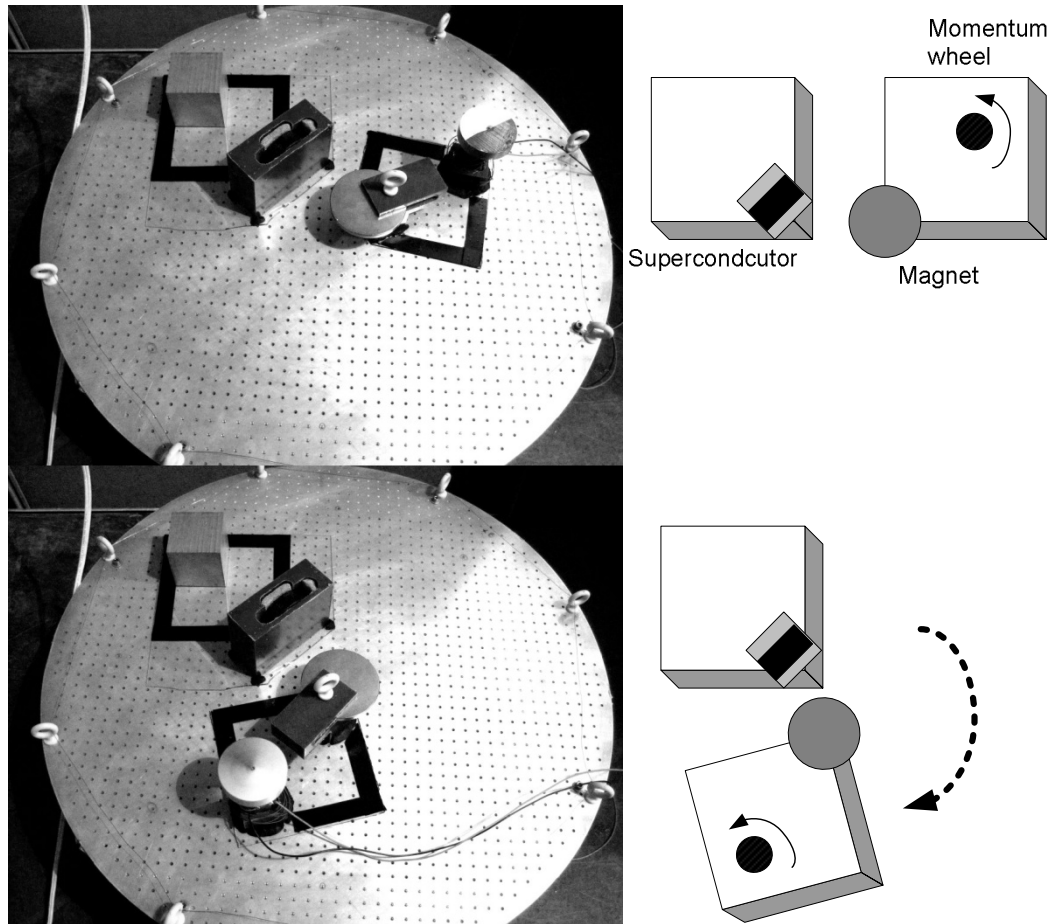


Fig. 3-3 Air-table demonstration of a non-contacting kinematic joint actuated by a momentum wheel.

magnet sits on the adjacent corner of a second module. In addition, the second module incorporates a simple momentum wheel activated remotely. The thin, cylindrical magnet has a high magnetic field magnitude and field gradient in the vertical and horizontal translation directions, which provide high FPI stiffness (tens of newtons per meter) between the “magnet module” and “superconductor module.” However, the axially symmetric field allows demonstrations of free rotation about the magnet’s dipole axis. When the momentum wheel spins up or down, its torque causes the magnet module to rotate about the non-contacting joint axis. Both demonstration modules remain stiffly connected in the other two relative degrees of freedom. (Note

that a counterweight restricts movement of the superconductor module, so its motion due to forces and torques transmitted through the FPI is much less apparent than the motion of the magnet module.) Since the kinematics and momentum actuator govern this reconfiguration procedure, the problems of plume impingement, relative orbital dynamics, and other issues that may affect spacecraft reconfigurations consisting of sequences of docking and undocking maneuvers are not present in this system. This mock-up demonstrates both the action-at-a-distance stiffness of flux pinning and an FPI's ability to reconfigure by forming a non-contacting revolute joint, a building block for many kinematic mechanisms including those in the previous two examples.

### 3.3 Chapter Conclusions

The reconfiguration of fractionated spacecraft is a challenging dynamics and control problem. It is possible that these challenges can be partly or fully addressed by instead treating the problem as a kinematic one. The extensive theory of multibody kinematics and kinematics of machines can then apply to spacecraft reconfiguration applications. Selection of the appropriate kinematic constraints adds determinism and robustness to modular systems. The need for active control and actuation during reconfiguration maneuvers decreases for systems with kinematics prescribed in such a way.

The flux-pinned interface is an enabling technology for such reconfigurable kinematic systems. FPIs are capable of locking and freeing joints between spacecraft modules (altering the spacecraft Jacobian), as well as latching onto and releasing the modules entirely (changing the incidence matrix of the multibody system). This chapter describes two simple ways in which FPIs enable the formation of mechanisms

to reconfigure a modular space system. In addition, it describes a simple kinematic mechanism demonstration incorporating an FPI on an air table. Future work in this area will concentrate on the development of suitable flux-pinned interfaces for the formation of kinematic mechanisms and on maneuver strategies for such mechanisms in spacecraft reconfiguration. However, the prospect of treating reconfigurable, modular spacecraft systems as kinematic mechanisms has more general application than to systems incorporating flux pinning

## CHAPTER 4

### FLUX-PINNED INTERFACES FOR THE ASSEMBLY, MANIPULATION, AND RECONFIGURATION OF MODULAR SPACE SYSTEMS

The previous chapter establishes that flux pinning provides stiffness sufficient to maintain the structure of modular space systems with an inter-module spacing up to approximately 5-7 cm for magnets and superconductors of modest mass ( $\sim 30$ -200 g). A flux-pinned magnet-superconductor pair exhibits sufficient stiffness for close-proximity spacecraft formation or docking maneuver applications, as high as 250 N/m for spacing less than 1 cm. Those experiments characterized flux-pinning in quasi-static situations, determining stiffness from the relation between the force exerted by flux pinning and small displacements of the magnet relative to the superconductor (Chapter 2).

Many other experimenters have examined the properties of magnetic flux pinning from the perspective of levitation in 1g [16,21,22,23]. Flux-pinning force exerted in the direction perpendicular to a superconductor's surface has therefore been well characterized. Spacecraft applications, however, take advantage of the fact that flux pinning affects the other rigid-body degrees of freedom as well. These applications also demand that some attention be paid to the dynamics, in addition to the static loads. This chapter explores the physical properties of a flux-pinned interface, with relevant applications to space systems described throughout. It then describes a dynamic experiment and results, corroborated with a theoretical model of flux-pinning force.

Material from this chapter was originally published as “Flux-Pinned Interfaces for the Assembly, Manipulation, and Reconfiguration of Modular Space Systems” in the *Journal of the Astronautical Sciences* [44].

## 4.1 Properties of the Interface

Prior investigations, both experimental and theoretical, have determined some of the basic properties of the stiffness and damping of a magnet flux-pinned to a superconductor [17,20,24]. Although the force between a permanent magnet and HTSC is, in general, hysteretic, small relative displacements yield force-versus-displacement curves that follow repeatable minor loops. This property allows the interaction to be modeled as a linear restoring force with a linear stiffness constant for small motions. Flux-pinning damping similarly resembles linear viscous damping for small motions. These linear properties hold regardless of the thermal and magnetic history of the interface, which can be described in two common situations. “Field cooling” occurs when the HTSC cools below its critical temperature with a magnet in pinning range, penetrating the HTSC with its field. “Zero-field cooling” is the case when a HTSC cools in the absence of any field and the magnet subsequently approaches from infinity, experiencing a hysteretic force before undergoing its small displacements [24]. However, the stiffness and damping forces acting on the flux-pinned pair are quantitatively different in the zero-field cooled and field-cooled cases [24]. The investigations in this work take place after field cooling, as this scenario would be the likely case if modules in space activate and deactivate their flux-pinned interfaces by altering the temperature of the HTSCs. Field cooling also provides a stable interaction in cases where hysteresis is not present [24].

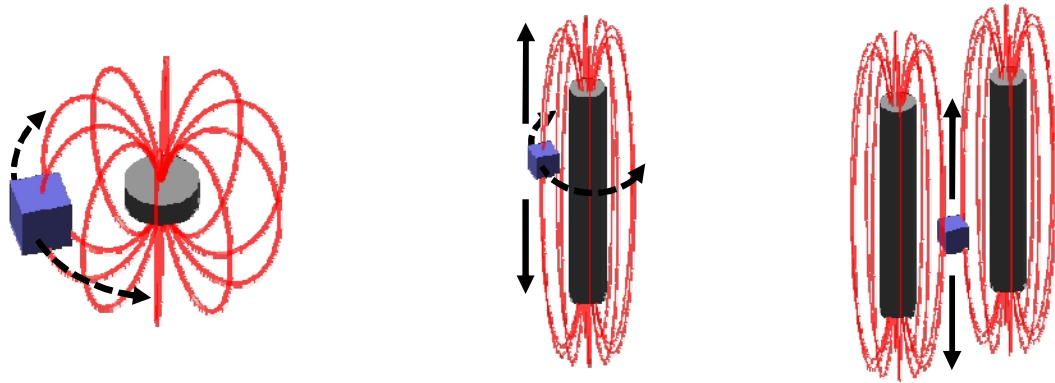


*Fig. 4-1 Kinematic mechanisms formed by flux pinning a superconducting cube to the fields of permanent magnets. The cube may freely undergo only the indicated motions. Left to right: revolute joint, cylindrical joint, and prismatic joint.*

The stiffness and damping of flux-pinned interfaces, or FPIs, obey certain quantitative relationships. Previous work has established that the translational stiffness between a magnet and field-cooled HTSC drops exponentially with distance as the initial pinning separation increases [41]. The lateral and perpendicular stiffnesses also obey the particular relationship that stiffness for small motions perpendicular to the HTSC surface is generally twice that for small motions along the surface. Others have measured this property experimentally and have proved it theoretically [24,28] and our quasistatic experiments confirm it (Chapter 2).

A flux-pinned interface also has the ability to pin only select degrees of freedom. Fig. 4-1 shows three basic joints that permanent magnets and a HTSC can form by taking advantage of this principle (Chapter 3). Since flux pinning does not constrain motions that preserve the magnetic field distribution inside the superconducting volume, designing a flux-pinned joint is equivalent to designing a magnetic field that remains constant within the superconductor during motions along the desired degree(s) of freedom. The simplest joint formed by a magnet-HTSC pair is a revolute joint (Fig. 4-1, *left*), in which the HTSC is free to spin about the magnet's dipole axis,

remaining at constant radius from the dipole center. An elongated, cylindrical magnet has a nearly uniform vertical field close to its midpoint, forming a cylindrical joint in which the HTSC slides along the magnet's axis over a limited range (*middle*). Finally, an additional permanent magnet constrains rotations of the HTSC, creating a prismatic joint (*right*). The high field gradients near the ends of each magnet act as non-contacting limit stops, preventing the HTSC from moving beyond a certain range.

There are several means by which flux-pinned interfaces consisting of HTSCs and magnets enable modular space systems capable of reconfiguration. Fig. 4-2 is a schematic of three of the many possible sequences of reconfiguration for simple modular systems, each with different results. These sequences rely on three properties of flux-pinned interfaces. First, FPIs are “switchable;” that is, the existence of flux-pinning forces depends on the thermal state of the superconductor in a binary fashion. Second, a magnetic field source feels no flux-pinning force or torque about any axis of symmetry in its field. Third, other non-contacting forces can perturb an established flux-pinning equilibrium.

Sequence (a) in Fig. 4-2 demonstrates reconfiguration via the switchability property of FPIs. The FPI connecting two pinned modules might be deactivated by warming its superconducting elements above  $T_c$ , freeing the modules to move. In space, the vehicle can warm its HTSCs simply by exposing them—or a spacecraft-bus face on which they are mounted—to sunlight. Traditional attitude-control actuators such as reaction wheels and thrusters might then be used to reposition the modules. Once components achieve a desired set of positions and orientations, the FPI can be reactivated (by shielding the HTSC from sunlight) to impose restoring and damping forces between the modules, locking them into a new configuration. The major disadvantage of this sequence is that it separates system components and is subject to

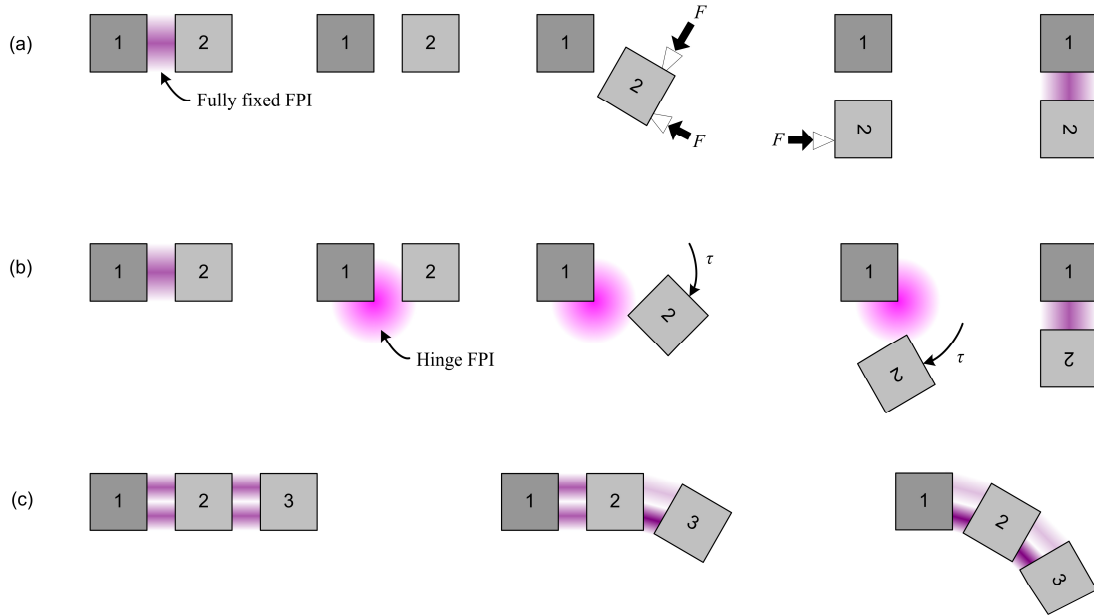


Fig. 4-2 Three possible modes of reconfiguration. (a) Flux pinning fixes modules only in their initial and end states, other actuators (thrusters shown) are used for the reconfiguration. (b) Flux pinning selects the available degrees of freedom between modules; in this example a hinge. (c) Electromagnets bend flux-pinned interfaces and articulate a modular structure.

the complexities of close-proximity formation flight and docking maneuvers, eliminating several advantages conferred by the flux-pinned interfaces during the reconfiguration process.

In sequence (b), the interface includes arrays of electromagnets oriented such that the deactivation of some magnets gives a net field with cylindrical symmetry. This symmetry creates a hinge from the pinning interface. Rotations about the symmetry axis of the field produce no restoring torque, while other degrees of freedom (translation and rocking rotations with respect to the superconductor) remain stiffened by the restoring force and torque of flux pinning [16]. The spacecraft modules now form a non-contacting mechanism that governs their transition into a new configuration before the electromagnets reactivate, stiffening motion in the remaining degrees of freedom and fixing the modules in place once again. At no point does the

FPI disconnect; the modules always remain stiffly bound near each other and rotate only around the defined axis of symmetry. This basic hinge concept extends to modular systems that reconfigure by forming an appropriate kinematic mechanism (Chapter 3). Wilson, Shoer, and Peck describe an experimental implementation of the maneuver depicted in Fig. 3(b) [37]. A space structure of flux-pinned modules can perform reconfiguration maneuvers by selecting appropriate joints at each interface to provide the required kinematic degrees of freedom.

Finally, the bottom sequence in Fig. 4-2 takes advantage of the continuum of equilibria afforded by flux pinning. This continuum gives an FPI some degree of malleability: pinned modules bend into a new configuration via distortion of the magnetic field. An FPI might achieve this new configuration by actuating the current in pinned electromagnets, activating secondary electromagnets arrayed around a pinned permanent magnet, or moving a ferromagnetic material near the superconductors. Depending on how the actuation is applied and the hysteretic properties of the superconductors, this deformation of a modular formation might be permanent or might relax when the actuation ceases. The FPIs retain their switchability features. So, a modular structure might form parts of itself into an articulated arm like that in Sequence (c) as one means to achieve pick-and-place reconfiguration as in Sequence (a).

There are several ways to actuate an active flux-pinned interface. For instance, nearby materials with magnetic properties have a perturbation effect on the interface. Such elements include ferromagnetic materials near the superconductor, which distort the pinned field and change the behavior of the interaction. Perturbations can also come from electromagnets positioned near the HTSC and activated after the permanent magnet has been pinned. These electromagnets force more flux into the

HTSC, altering how the superconductor responds to motions of the pinned magnet. As another example, an active electromagnet flux pinned to a HTSC can be tuned after pinning is established to change the properties of the flux-pinned interface. Behavior changes are possible through modification of the equilibrium separation between the HTSC and flux-pinned magnet and through modification of the stiffness or damping forces experienced by the pinned magnet-superconductor pair.

## 4.2 Image-Dipole Model

In some cases, an effective representation of the magnetic field of the HTSC is the field produced by two virtual *image dipoles* within the superconductor. This *frozen-image model* mimics the effect of the superconductor on the external magnetic field, giving analytical expressions for simulation [45]. This model applies when the superconductor is field-cooled, the magnet-superconductor separation is much greater than the superconductor's skin depth, and hysteresis is negligible. These conditions are consistent with the experiments reported here. In addition, the field of a dipole is a reasonable approximation for a permanent magnet as long as any test point in this field is far from the magnet edge. At position  $\mathbf{r}$  and with dipole

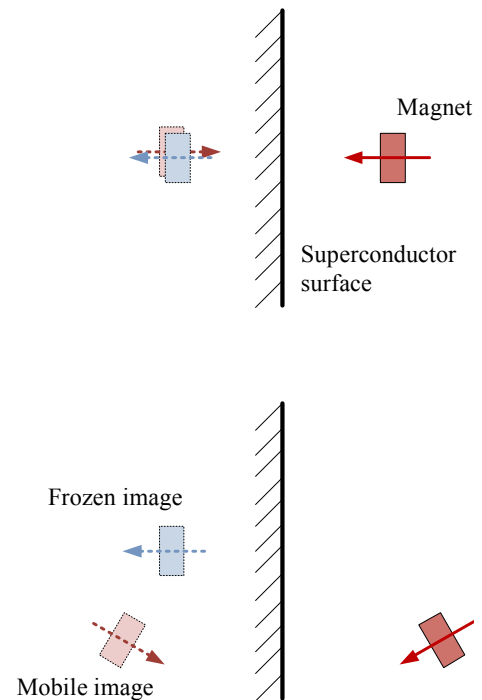


Fig. 4-3 Image-dipole model of flux pinning. Top: frozen and mobile images appear within the superconducting volume upon field-cooling. Bottom: the frozen image remains fixed, while the mobile image moves with the magnet.

moment vector  $\mathbf{n}$ , the field of a magnetic dipole is

$$\mathbf{B} = \frac{\mu_0}{4\pi r^3} (3(\mathbf{n} \cdot \hat{\mathbf{r}})\hat{\mathbf{r}} - \mathbf{n}), \quad (4-1)$$

where the hat denotes a unit vector [46]. This field interacts with two images within the superconductor. One, the frozen image, appears at a position reflected across the superconductor surface from the external magnet's position. The field from the frozen image develops when the superconductor is first field-cooled, and the image remains at this position and orientation as long as the superconductor remains below its critical temperature. Its dipole vector is both reflected and negated in relation to that of the external magnet at the instant of field cooling. Therefore, the frozen image attracts the external magnet for small relative displacements and rotations. If the superconductor surface passes through the origin and has normal vector  $\hat{\mathbf{a}}$ , then the reflection of a vector  $\mathbf{r}$  across this plane is

$$\mathbf{r}_{reflected} = \mathbf{r} - 2(\hat{\mathbf{a}} \cdot \mathbf{r})\hat{\mathbf{a}}. \quad (4-2)$$

Thus, the field of the frozen image is

$$\mathbf{B}_f = \frac{\mu_0}{4\pi\rho_f^3} \left( 3[(2(\hat{\mathbf{a}} \cdot \mathbf{n}_{FC})\hat{\mathbf{a}} - \mathbf{n}_{FC}) \cdot \hat{\boldsymbol{\rho}}_f]\hat{\boldsymbol{\rho}}_f - (2(\hat{\mathbf{a}} \cdot \mathbf{n}_{FC})\hat{\mathbf{a}} - \mathbf{n}_{FC}) \right) \quad (4-3)$$

where  $\boldsymbol{\rho}_f = \mathbf{r} - \mathbf{r}_{frozen} = \mathbf{r} - \mathbf{r}_{FC} + 2(\hat{\mathbf{a}} \cdot \mathbf{r}_{FC})\hat{\mathbf{a}}$  represents the relative position and subscript “FC” represents the position and moment vectors at the time of field-cooling. The position vector  $\mathbf{r}$  of the flux-pinned dipole may vary with time.

The second image is a mobile image that moves in response to the external magnet. At any time, it appears at the reflected position vector of the external magnet with a dipole axis vector also reflected from that of the external magnet. The mobile image, which mimics Meissner-effect exclusion of magnetic fields from the

superconductor, generally repels the external magnet. The field of the mobile image resembles that of the frozen image, obeying the stated reflection laws:

$$\mathbf{B}_m = \frac{\mu_0}{4\pi\rho_m^3} (3[(\mathbf{n} - 2(\hat{\mathbf{a}} \cdot \mathbf{n})\hat{\mathbf{a}}) \cdot \hat{\boldsymbol{\rho}}_m]\hat{\boldsymbol{\rho}}_m - (\mathbf{n} - 2(\hat{\mathbf{a}} \cdot \mathbf{n})\hat{\mathbf{a}})) \quad (4-4)$$

A key difference between the equations for the field of the frozen and mobile images is that the quantities that determine the mobile image field, including the relative position  $\boldsymbol{\rho}_m = \mathbf{r} - \mathbf{r}_{mobile} = 2(\hat{\mathbf{a}} \cdot \mathbf{r})\hat{\mathbf{a}}$ , may vary with time.

Once the frozen and mobile image fields are known, the force and torque on the external dipole with axis  $\mathbf{n}$  are straightforward to calculate:

$$\begin{aligned} \mathbf{F} &= \nabla (\mathbf{n} \cdot (\mathbf{B}_f + \mathbf{B}_m)) \\ \boldsymbol{\tau} &= \mathbf{n} \times (\mathbf{B}_f + \mathbf{B}_m) \end{aligned} \quad (4-5)$$

Stiffnesses can be calculated either numerically or by evaluating partial derivatives of the force and torque given by these expressions. However, damping ratios for the flux-pinned magnet and superconductor cannot be calculated from this model as the damping arises from hysteretic losses, which are not described by the image magnets.

One great advantage of the frozen-image model is that it does not require the extensive numerical computations of, for instance, simulating supercurrent distributions. The model provides design intuition for the magnet-superconductor interaction. Several features of the interaction are evident from Fig. 4-3. The field-cooled position of the magnet is the flux-pinning equilibrium since the two image dipoles coincide when the magnet is in this position, giving a net zero field and therefore no force. Furthermore, this equilibrium is stable for small displacements, since the frozen image generally attracts the magnet towards it while the mobile image always repels it: if the magnet moves closer to the HTSC surface, the repelling image

is closer and thus exerts a greater force on the magnet. The reverse is true when the magnet displaces away from the superconductor. Similar relations for magnet displacements along the superconductor surface demonstrate stability in that direction as well. In addition, the nonlinearity of the system is apparent from the varying separations between the magnet and its images and the fact that dipolar magnetic fields fall off with the inverse cube of distance. Finally, the image model offers insight into why Earnshaw's Theorem does not limit flux pinning: the motions of the mobile image in response to the flux-pinned magnet have a direct parallel to active control, which can maintain stable equilibria between magnets.

This model reproduces and extends the quasistatic experiment results of Chapter 2. It provides a basis for calculating the six-dimensional stiffness matrix of an arbitrary collection of magnets and superconductors, provided that the collection is consistent with the assumptions of the image model. Superpositions of the simple analytical expressions for dipole fields lead to easy-to-calculate numerical expressions

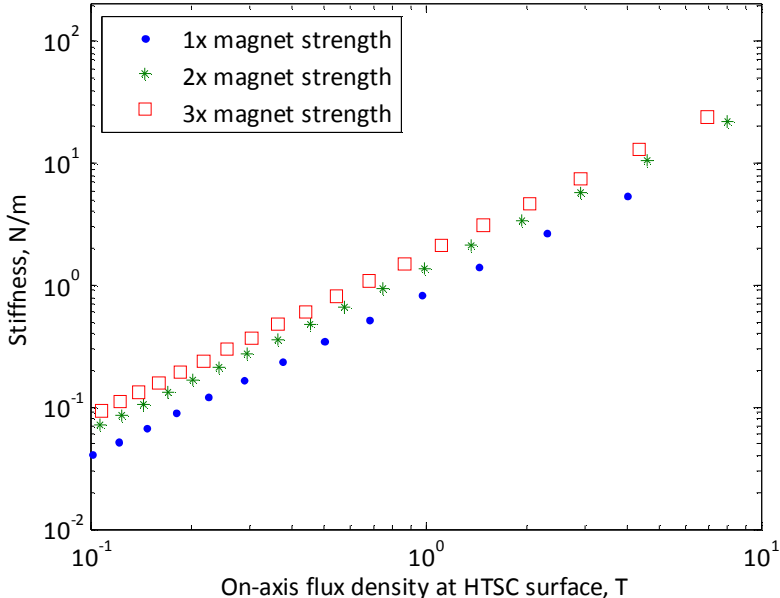


Fig. 4-4 Log-log plot of translational stiffness of a flux-pinned magnet-superconductor pair against flux density at the superconductor surface.

for the fields of nearly dipolar magnets. Fig. 4-4 mimics in simulation a plot showing data obtained experimentally in Chapter 2 (Fig. 2-8). These numerical results confirm that the flux-pinned stiffness of a paired magnet and superconductor has a power-law dependence on the flux density projected to the superconductor surface.

The frozen image represents the magnetic flux distribution from supercurrents excited by the flux-pinned magnet, but the frozen image persists even if the field-cooled magnet moves far away from the superconductor. This persistent image interacts with any other magnet that approaches the superconductor surface as long as the superconductor temperature remains below  $T_c$ . This property suggests that a superconductor can be “preloaded” with a magnetic flux distribution such that it passively attracts magnets to the established non-contacting 6DOF equilibrium. In this way, flux-pinned interfaces enable passive self-assembly of modular spacecraft that have never come into contact with one another before assembly begins.

### 4.3 Experiment

The experimental apparatus is designed to characterize the 6DOF stiffness and damping of a flux-pinned interface, under a variety of conditions, using system-identification techniques. Similar experiments have been performed in the context of superconducting levitation applications, where a magnet is levitated over an HTSC and then its position measured as it vibrates in response to some input [24,40]. However, since we envision flux pinning applications in zero gravity, experiments reported here are not restricted to levitation. Levitation involves an equilibrium between flux pinning and gravitational forces, while the objectives of these experiments include characterizing only flux pinning.

Fig. 4-5 is a schematic of the experimental setup. A field-cooled single-domain YBCO disc with diameter 56 mm and thickness 20 mm is immersed in a liquid nitrogen bath with its axis of symmetry oriented horizontally, i.e., along the experiment's  $x$  axis. A translation stage precisely positions the superconductor near a permanent magnet. The stage allows magnet-superconductor separations from  $d = 5$  cm to about 1.5 m. The magnet itself is the bob of a  $\sim 3.5$  m long pendulum. The pendulum constrains motions of the magnet in the direction of gravity and severely limits rotations of the magnet about its dipole axis but allows small motions in all other rigid-body degrees of freedom. The constrained motions are either equivalent to other motions by symmetry or are unaffected by flux pinning. The pendulum dynamics affect the four remaining modes in a quantifiable manner.

The inputs and outputs chosen for system identification do not interfere with the motion of the magnet relative to the superconductor. A simple coil of wire supplied with a computer-controlled current drives the flux-pinned system. This electromagnet does not contain a ferromagnetic core, which keeps it from affecting the flux-pinned magnet's equilibrium when no current flows in the coil. A motion-capture camera

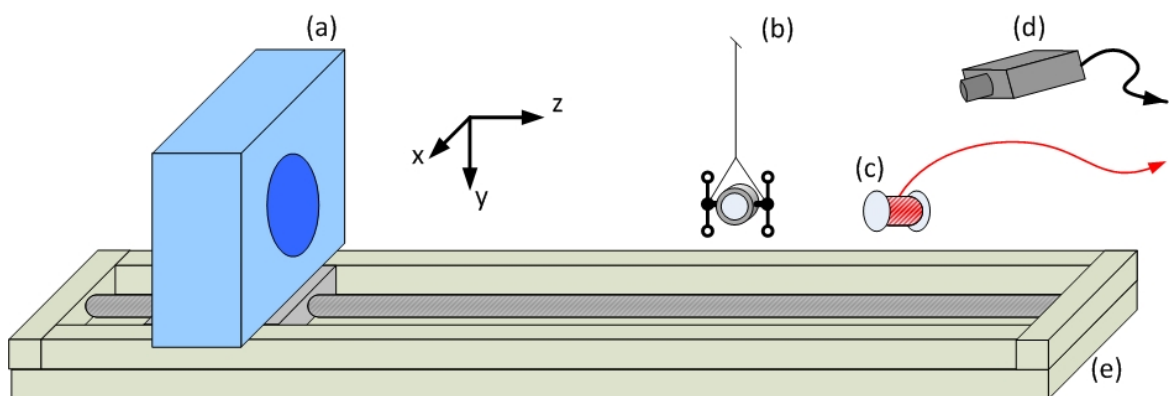


Fig. 4-5 Experimental setup, showing the placement of the (a) vertically-mounted YBCO superconductor in its liquid nitrogen bath, (b) pendulum with permanent magnet and tracking flags, (c) input coil, (d) motion-capture camera system, and (e) translation stage.

system tracks the resulting movements of the pendulum bob with a minimum frame rate of 105 fps, allowing frequency measurements up to at least 10 Hz. Reducing the region of interest of the camera CCD allows it to achieve higher frame rates and reliably measure frequencies up to 15 Hz. Low-mass flags with bright target-tracking points on the pendulum bob and a contrasting black background behind the pendulum facilitate motion capture.

The motion-capture data describes the position of the tracking flags in the camera's field of view. The actuating electromagnet coil and motion-capture camera excite and measure each of the fundamental modes of the pendulum bob. The modes of the unpinned pendulum include swinging motion in the directions parallel ( $x$ ) and perpendicular ( $z$ ) to the superconductor surface, twisting rotation about the monofilament pendulum axis, and rocking rotations about the axis perpendicular to

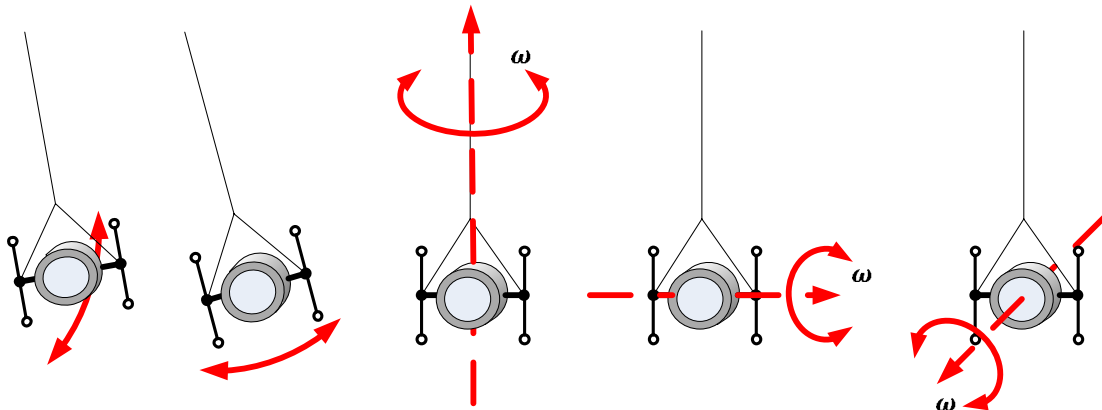


Fig. 4-6 Modes of the pendulum bob. From left to right: swinging (perpendicular to the HTSC), swinging (parallel to the HTSC), twisting, rocking, and rolling motion.

both the magnetic dipole axis and pendulum axis. Rolling motion of the magnet is not affected by flux pinning as this motion is a rotation about the magnetic dipole axis. It is limited by the construction of the pendulum bob and enters into the system only as a higher-order pendulum mode. Fig. 4-6 shows these mode shapes. Fast Fourier transforms (FFTs) of position time histories from the tracking camera provide the

spectral content of the pendulum motion. A set of second-order system models fit to the FFTs model stiffness and damping for the flux-pinned interface.

The resonant frequencies in each FFT decompose into a combination of the free pendulum frequency and frequency introduced by flux-pinning stiffness. The one-dimensional equation of motion for a pendulum bob connected to a vertical wall by a spring is

$$\begin{aligned}\ddot{z} &= -\frac{k}{m}z - \frac{g}{l}z \\ &= -\left(\frac{k}{m} + \frac{g}{l}\right)z\end{aligned}\tag{4-6}$$

for small motions of the pendulum bob. The frequency of oscillation for the composite system, therefore, is

$$\begin{aligned}\omega &= \sqrt{\frac{k}{m} + \frac{g}{l}} \\ &= \sqrt{\omega_{pinning}^2 + \omega_{pendulum}^2}\end{aligned}\tag{4-7}$$

Thus, the resonance introduced by flux-pinning stiffness adds in root-sum-square fashion to the existing pendulum frequency. Frequencies related to other stiff elements in the pendulum system (such as torsion of the pendulum bob about the pendulum axis) similarly combine in this fashion with flux-pinning frequencies. The frequency of each mode is unique due to the mass properties of the pendulum bob, with the exception of the two swing modes. These two modes are split by the unequal lateral and transverse flux-pinning stiffnesses. Thus, the frequencies of each distinct DOF can be identified in the FFTs.

The pendulum arrangement is versatile and can accommodate many experiments to determine the behavior of a flux-pinned interface under different perturbations. Experiments to characterize the dynamic stiffness and damping of flux pinning involve tracking pendulum motions when the actuating coil applies impulses, sine

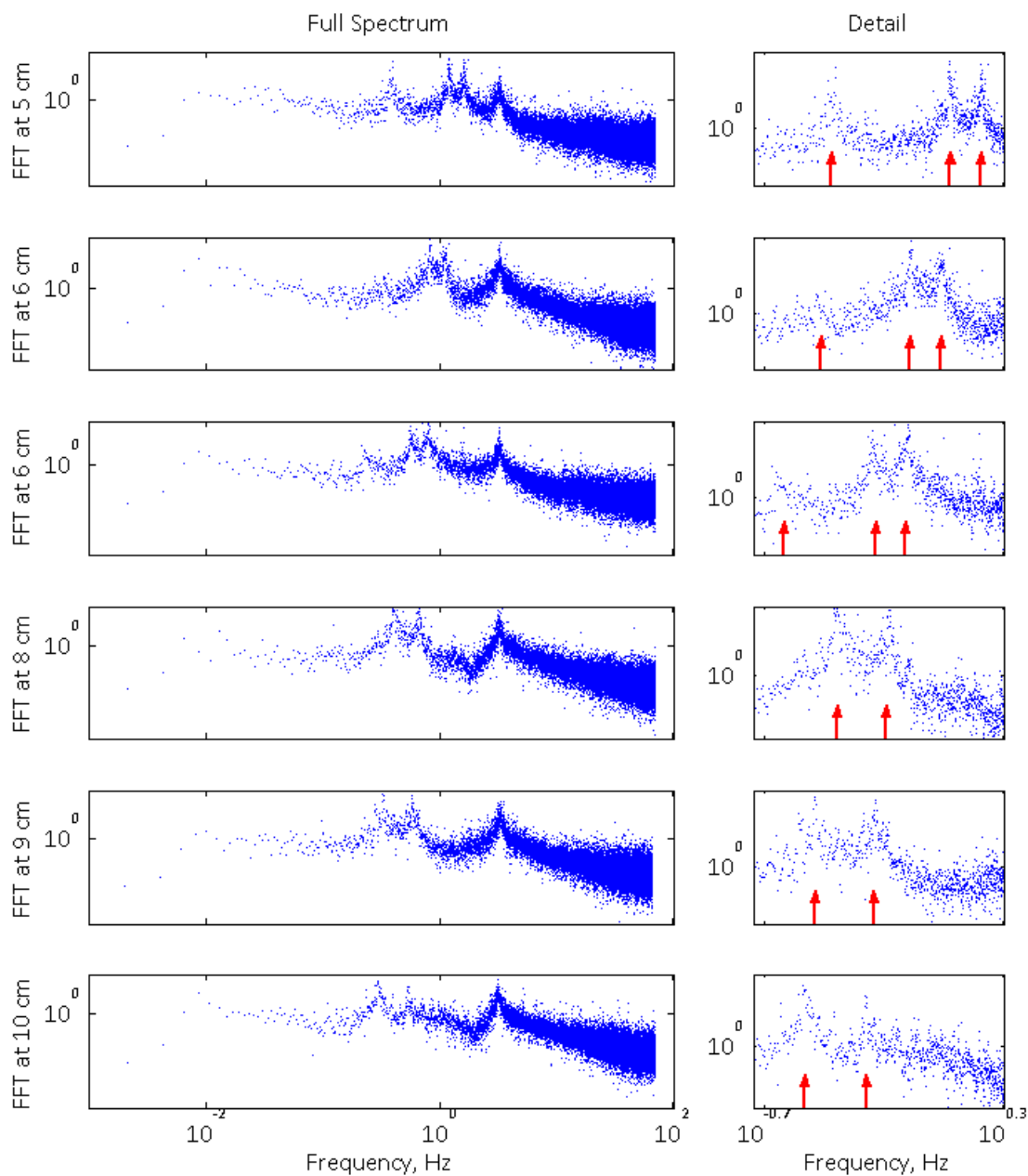


Fig. 4-7 Modification of pendulum modes, as measured by FFTs of motion capture data.

sweeps, Gaussian noise, or other inputs. Simple initial tests determine the range of distances over which flux pinning acts for various types of magnets and superconductors. More subtle tests include modifying the interface with other conductive materials in an effort to establish the feasibility of different ways of adjusting stiffness, damping, and equilibrium position.

## 4.4 Results and Discussion

### 4.4.1 Range of Flux Pinning

In order to establish a flux-pinning interaction between a magnet and superconductor, the magnet must project a minimum field into the superconducting volume. Any less than the minimum and the superconductor exhibits only Meissner repulsion of the magnet, which cannot establish a stable action-at-a-distance equilibrium. Measurements of the resonant frequencies of the pendulum as a function of magnet-superconductor separation clearly indicate the distance at which the magnet provides the minimum flux to the superconductor because the flux-pinning stiffness  $k_z$  is twice  $k_x$ . Therefore, the swing mode of the pendulum shifts from its unpinning frequency due to Meissner repulsion as it approaches the YBCO, but the resonance splits into two distinct modes only when flux pinning is present.

Fig. 4-7 shows a series of FFTs of the captured motion for varying magnet-superconductor separation distances, with one cylindrical NdFeB magnet (approximately 3.8 cm in diameter and 1.3 cm tall, with a mass of about 30 g and a measured dipole moment of about 2.5 J/T) on the pendulum and one single-domain YBCO disk. For distances ranging from approximately  $d = 5$  to 7 cm, four resonance peaks appear in the Fourier spectrum (the detailed spectra show three of the four

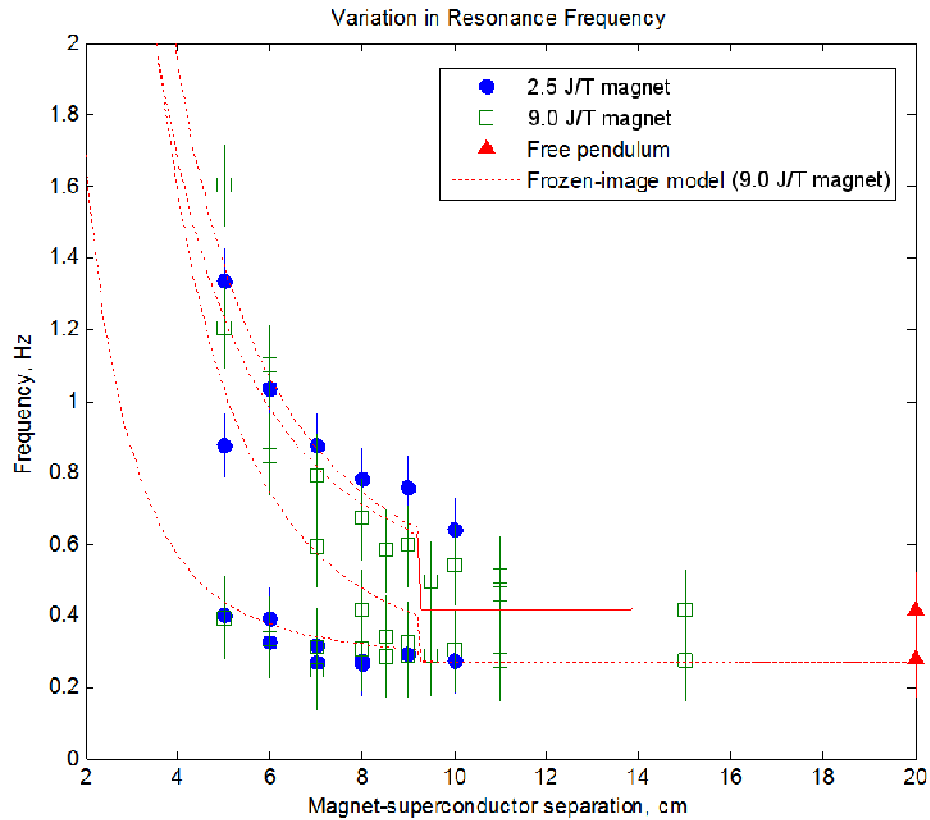


Fig. 4-8 Pendulum frequency modification as a function of field-cooling separation distance; data and frozen-image model.

peaks). However, at  $d = 8$  cm and beyond, two of the peaks have merged. The resonance splitting is qualitative evidence that the range of flux pinning for this magnet-superconductor configuration is approximately 7 cm. Other configurations, including larger single-domain YBCO discs and special arrangements of magnets, may increase this pinning range.

#### 4.4.2 Pendulum Mode Modification

Fourier transform data such as that in Fig. 4-7 provides stiffness and damping data through fits of a simple harmonic oscillator model to each peak within its half-power bandwidth. The dependence of resonant frequency on separation is clear in Fig. 9, in

which frequencies are plotted along with values obtained from the frozen-image model. Error bars on the plot show the standard deviation in measurements of a pendulum frequency that was not modified by flux pinning. The values agree qualitatively, confirming that frequency decays exponentially with field-cooling separation until there is not enough flux penetrating the superconductor upon field cooling to allow flux pinning. At separations below this minimum-flux limit, about 9-10 cm in Figs. 9 and 10, flux pinning cannot affect the pendulum frequency. The frozen-image model of the pinned pendulum adopts the unmodified pendulum frequency beyond this separation distance to represent this effect. The decreasing trends of both the modeled and experimental data in Fig. 10 are consistent with the

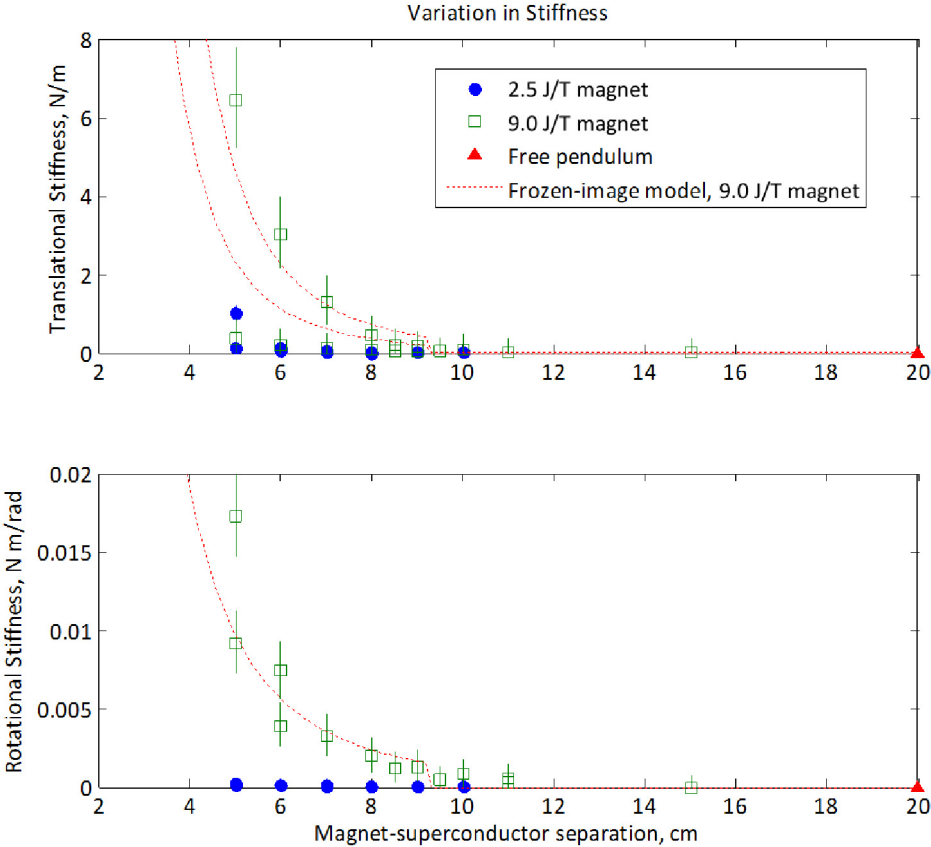


Fig. 4-9 Flux-pinned stiffness as a function of field-cooling separation distance; data and frozen-image model.

conclusion from Chapter 2 that stiffness decays exponentially with pinning separation out to a limit at the maximum range of flux pinning. The image model correspondence with this data allows a better estimate of the maximum range of flux pinning than does that in the preceding section. We conclude that the 9.0 J/T NdFeB magnet and single-domain YBCO disc exhibit flux-pinning behavior at separations up to approximately 9-10 cm, with decreasing stiffness as the field-cooling separation increases.

Fig. 4-9 shows the translational and rotational stiffnesses of two identical, axially attached magnets flux-pinned to the YBCO discs as a function of field-cooling separation after the particular vibration modes from Fig. 9 were identified. Again, the frozen-image model matches the exponential decay trend of the plots for separation distances where flux pinning occurs. The upper points in the translational stiffness plot are associated with the pendulum swing mode in  $z$ . This value is a key performance parameter of a flux-pinned interface, since stiffness about other translational and rotational degrees of freedom can be constructed from  $k_z$  through various arrangements of axially stiff magnet/superconductor pairs. Figure 10 clearly indicates that a larger magnet enhances stiffness: the dipole moments of the rare-earth magnets are 2.5 and 9.0 J/T, and the larger magnet provides the FPI with a little over three times the stiffness  $k_z$  of the smaller magnet. In fact, the increased stiffness with a larger magnet corroborates the principle that the stiffness of a flux-pinned interface scales with the magnetic flux at the YBCO surface at the time of field-cooling according to a power law, as calculations with the frozen-image model show (in Fig. 4-4). The data in Fig. 4-10 support this experimentally for cylindrical magnets. We therefore regard the magnetic flux density projected onto the superconducting components of a flux-pinned interface as an important metric in optimizing the design of FPI hardware.

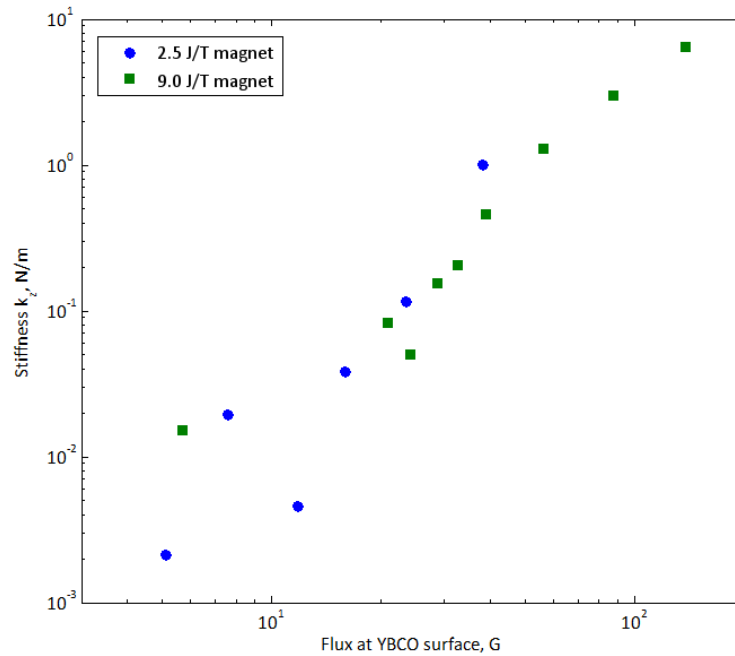


Fig. 4-10 Flux-pinned stiffness versus magnetic flux density at the superconductor surface upon field-cooling.

Fig. 4-9 does not show the expected relationship of translational stiffnesses, that  $k_z = 2k_x$  [24,28]. The probable reason for this discrepancy is that the vibration mode shapes of the flux-pinned pendulum do not correspond directly to the Cartesian coordinates  $x$  and  $z$ . The normal modes of oscillation are, rather, swing along the superconductor surface normal and two combinations of the twist and swing modes. These modes are the “rolling motions” described in Sugiura et al. [23]. Frequencies and stiffnesses of these modes are shown here as “translation” or “rotation” according to the coordinate with which the mode shape is best aligned.

Damping in a flux-pinned magnet-superconductor pair results from hysteretic energy losses as the magnet moves relative to the superconductor. However, these data are unable to distinguish the damping ratio of the pendulum flux pinned to the single-domain YBCO from the damping naturally present in the pendulum. A likely

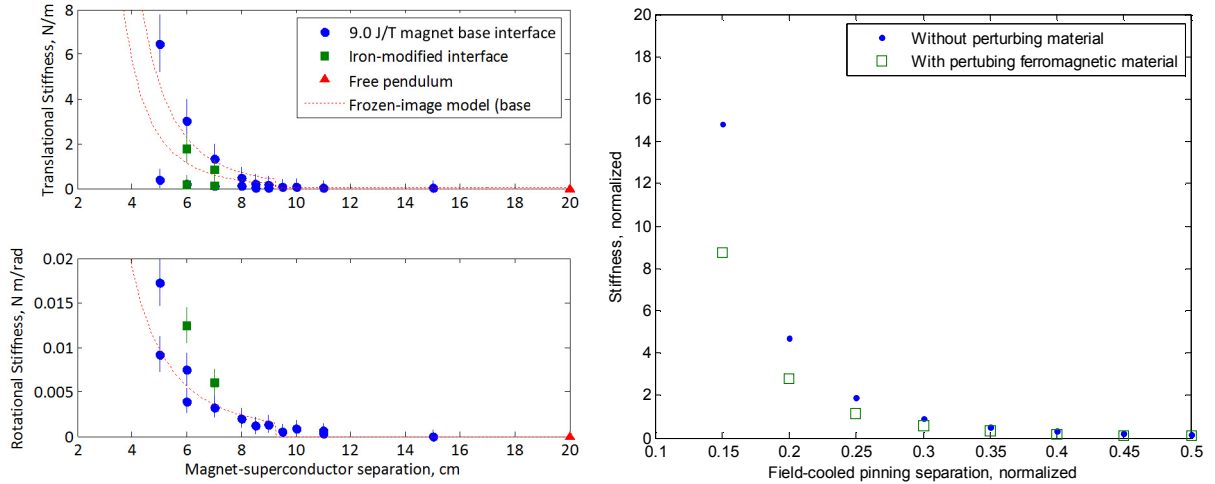


Fig. 4-11 Flux-pinned stiffness versus field-cooling separation in the presence of an iron plate. Left: experimental measurements, right: frozen-image model of  $k_z$  vs.  $d$  with iron plate.

conclusion from the absence of damping is that the single-domain superconductors exhibit very non-hysteretic interactions—a useful fact, as it implies that hysteresis is low. This low damping validates one of the initial assumptions of the frozen-image model and allows us to neglect hysteresis in the treatment of similar flux-pinned interfaces based on these superconductors. Instead, the use of other materials, such as thin aluminum plates, can provide damping for an FPI through eddy-current effects, as described in the next section.

#### 4.4.3 Performance modification and actuation of flux-pinned interfaces

The properties and behaviors of a flux-pinned interface can be modified by design. Methods of doing so include adding passive hardware elements as perturbations on the base FPI (such as ferromagnetic materials, diamagnetic materials, conductive metals, or permanent magnets) and flux pinning an actively controlled electromagnet rather than a permanent magnet. This section examines the effect of these modifications on the equilibrium position of the pinned pendulum bob and the

stiffness and damping of the flux-pinned interface through both frozen-image simulation and experiment.

Fig. 4-11 illustrates how the presence of ferromagnetic material modifies the stiffness of the flux-pinned interface while maintaining the magnet-superconductor separation at its field-cooled value. In this experiment, the perturbation is an iron disc approximately the same size as the YBCO, placed on the opposite side of the superconductor from the magnet. Before field cooling, when the YBCO is not in its superconducting state, the ferromagnetic disc attracts magnetic flux lines into the YBCO volume, changing the magnitude and gradient of the magnetic field within the superconductor. This configuration exhibits a number of qualitatively different effects on the pendulum modes. Translational stiffness  $k_z$  decreases, while  $k_x$  remains largely the same. Rotational stiffness (corresponding to the pendulum twist mode) increases. A simple simulation with the frozen-image model, treating the iron disc as another (weak) dipole attracting the flux-pinned magnet, also shows a drop in translational stiffness perpendicular to the superconductor. So, an FPI design may trade one for the other by varying the amount of ferromagnetic material near the superconductor.

While the single-domain superconductors are relatively non-hysteretic and thus very lightly damped, other non-contacting interactions with magnets may provide valuable damping for a flux-pinned interface. For example, a magnet near conductive metal such as aluminum is subject to the well-known eddy-current damping effect. We performed several experiments with aluminum plates between the magnet and superconductor and found that the aluminum does not interfere with the flux-pinned equilibrium or stiffness but dramatically enhances the damping of the pendulum up to strong overdamping. The results of one such damping experiment appear in Fig. 4-12. At the 5-6 cm separations, when an aluminum plate is present the damping ratios of

each mode are enhanced. The inclusion of conductive plates to provide eddy-current damping allows flux-pinned interfaces to exhibit both high stiffness and high structural damping, which would be important to non-contacting modular spacecraft systems such as those described in Norman and Peck [13] or Gersh [14]. The

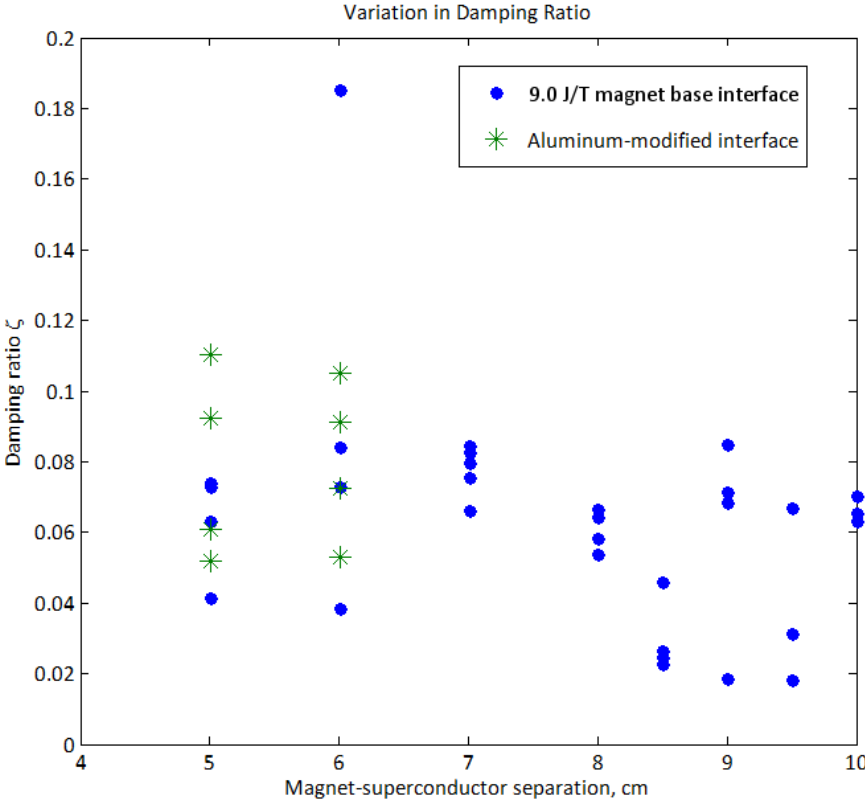


Fig. 4-12 Damping a flux-pinned interface with a plate of aluminum over the superconductor.

properties of these conductive plates may be tailored to design FPIs with a desired damping ratio; some configurations exhibit significant overdamping in the FFTs. This result is particularly compelling if the flux-pinned connections between modules provide the “virtual structure” of a fractionated spacecraft: Demchak [47] recommends passive damping ratios be modeled at no lower than  $\zeta = 0.001$  for space structures. Common practice is 0.0025. A flux-pinned interface may provide an even higher level

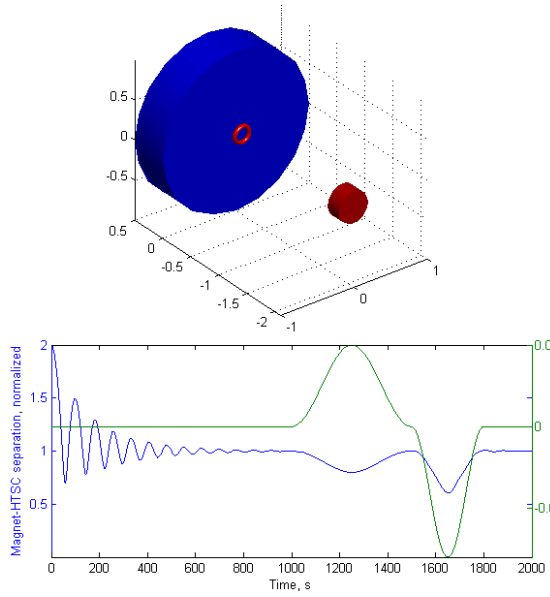


Fig. 4-13 Top: schematic of a magnet (red) flux-pinned to a HTSC disc (blue) with an electromagnet coil (gold ring) near the disc. Bottom: simulated time history of the magnet position (blue) and control coil field (green).

of passive damping than this guideline when modules are separated by several centimeters. Therefore, a flux-pinned interface can eliminate some conservatism in dynamics analysis. They may also represent an opportunity to improve the stability margins and/or performance of control loops associated with these relative motions.

Along with confirming previous results, an extension of the

frozen-image model suggests that nearby electromagnets can actuate a flux-pinned interface. The time history of simulated motion in a possible scenario is shown in Fig. 4-13. In this simulation, a magnet falls in towards a superconducting disc that has been “preloaded” with flux by field-cooling and settles into the previously established equilibrium. A control electromagnet located at the superconductor surface then activates, pulling the magnet into a new, adjustable equilibrium. Taking the  $z$  direction to be normal to the HTSC surface, this one-dimensional equilibrium is the solution of

$$0 = \frac{m^2}{(z_0 + z)^4} - \frac{m^2}{(2z)^4} + \frac{m_c m}{(z - \delta)^4} - \frac{m_c m}{(z + \delta)^4} \quad (4-8)$$

In this model, the permanent magnet with moment  $m$  and initial position  $z_0$  interacts with its flux-pinned images, the control electromagnet with moment  $m_c$  and position  $\delta$ , and the Meissner image of the electromagnet in the superconducting disc. An

arrangement of electromagnets around a flux-pinned interface thus offers the possibility of controlling the separation and orientation of FPI-linked components. The dipole moment of the control electromagnet in the scenario of Fig. 4-13 is much smaller than that of the permanent magnet, suggesting that very little power need be applied to the actuating electromagnets. Should the actuators fail, the components remain robustly bound by the unperturbed flux-pinning stiffness provided by the permanent magnet.

## 4.5 Chapter Conclusions

The stiffness and damping of flux pinning over a wide range of separations, as well as an understanding of how the interface responds to manipulations, can inform the design of flux pinning hardware for modular space systems. A design guideline of this type is shown in Fig. 4-14. Here, the 9.0 J/T rare-earth magnet and single-domain

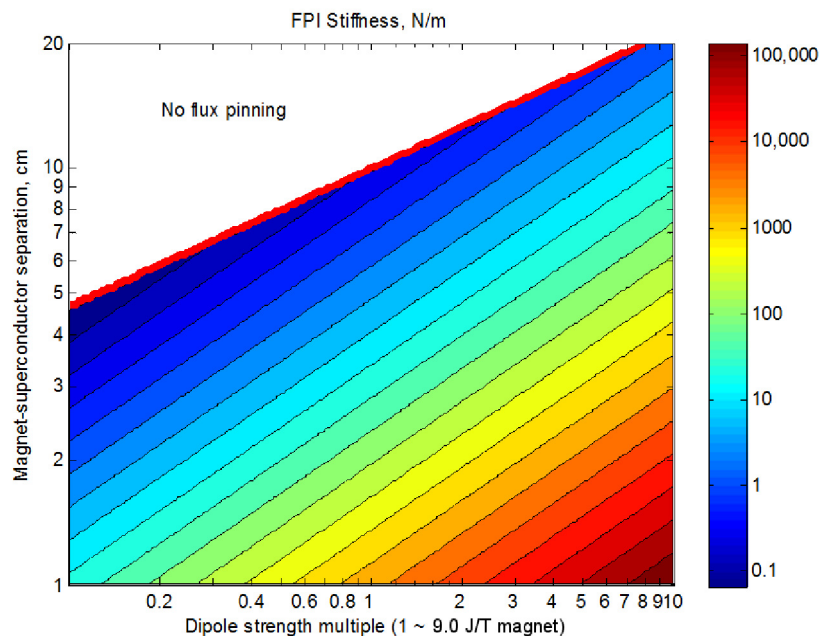
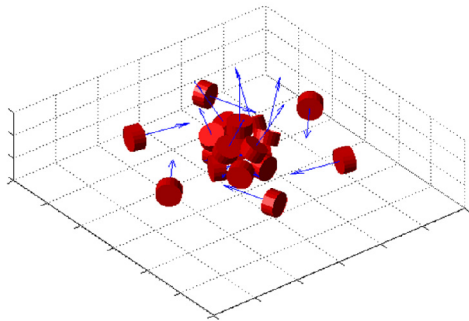


Fig. 4-14 Design space of a flux-pinned interface based on the 9.0 J/T magnet and single-domain YBCO in these experiments.

YBCO disc from these experiments provide the basis for simulated FPI stiffness over a range of separation distances and for a range of dipole moments. The dipole moment of a magnet corresponds roughly to the mass of the magnet, and the mass of the magnet is likely much greater than that of the YBCO; so, this result takes the magnet mass to be the significant performance parameter. The plot shows a range of achievable stiffnesses and inter-module separation distances for a modular system with flux-pinned interfaces similar to the pendulum apparatus. This magnet-superconductor configuration is not necessarily optimal in the sense that it may not project the greatest possible flux to the YBCO surface; other configurations of magnets may be able to optimize this quantity. For example, the arrangement of



*Fig. 4-15 Potential arrangement of magnets for a flux-pinned interface.*

permanent magnets in Fig. 4-15 efficiently projects magnetic flux towards a single-domain YBCO disc above it while limiting the magnetic field bias introduced to the spacecraft bus below the magnets, similar to a Halbach array [48]. These interfaces may form the basis of next-generation docking and mating adapters

or even act as a non-contacting structure supporting modular space systems with inter-module spacing on the 10 cm to 1 m scale.

The ability to alter the equilibrium separation between a flux-pinned magnet and a superconductor offers the possibility of relatively simple actuation of a flux-pinned interface. For example, introducing a perturbing field by increasing the current in a nearby electromagnet causes the equilibrium magnet-superconductor separation to change, so that spacecraft with flux-pinned interfaces would be able to adjust their relative positions, carry out docking maneuvers, and even manipulate other modules

through the interfaces, without physical contact or fuel expenditure. Flux-pinning interfaces may then perform the functions of more familiar manipulators, mating adapters, and close-range formation-flight and maneuvering-hardware technologies. Such articulated systems developed around a flux-pinned “virtual structure” would be passively robust in the event of actuator failure.

The requirement that certain elements of an FPI remain below a critical temperature offers the possibility that such structures might reconfigure by toggling their flux-pinned interfaces on and off. This temperature management might be achieved simply by exposing superconductors to or shielding them from sunlight. Interface toggling behavior is equivalent to docking and release maneuvers, but the force fields involved do not require physical contact between structure elements at any point in the process. Reconfiguration of spacecraft modules in close proximity using flux-pinned interfaces would therefore be a low-risk activity compared to the reconfiguration of a modular system by traditional means. Toggling a flux-pinned interface in such a way would be analogous to activating and deactivating a virtual truss segment between modules.

Yet another exciting possibility relies on the feature that flux pinning does not exert forces or torques along directions of zero magnet field gradient. This feature allows the construction of modular systems in which flux pinning forms the modules into a kinematic mechanism designed to facilitate reconfiguration. A non-contacting, flux-pinned mechanism architecture as in Fig. 4-2(b) has several advantages over both other flux-pinned reconfiguration methods and traditional close-range formation flying or docking methods. All modules may be structurally identical and contain universal interfaces with arrays of magnets. No specially constructed hinge interfaces are necessary. Activation or deactivation of electromagnets in a generic interface

introduces or removes specified kinematic degrees of freedom. In addition, because the modules do not come into physical contact, there is no physical wear of components, and the potential for deployable mechanisms to jam in orbit is virtually eliminated. Spacecraft reconfiguration achieved through kinematics also provides advantages and savings through a reduced reliance on active control: an appropriately selected mechanism constrains undesirable motions kinematically, and the natural dynamics of the entire structure might be enough to drive the reconfiguration process without power input. At most, small internal torques (provided by, for instance, reaction wheels) may be required to rotate modules about a joint.

This investigation indicates that useful design parameters of a flux-pinned interface based on a single magnet and single superconductor include:

- The dipole moment of the magnet. Increased dipole moment gives increased stiffness at constant separation distance and increased maximum flux-pinning range.
- The hysteretic properties of the superconductor. A hysteretic superconductor provides an FPI with more inherent damping. However, hysteresis is not a desirable dynamical property of a space system, and damping can be achieved by other means.
- The amount of ferromagnetic material near the interface, particularly on the opposite side of the superconductor relative to the magnet. More ferromagnetic material changes the relative strengths of the various translational and rotational stiffnesses.
- The amount of conductive material near the interface. Conductive metals introduce eddy-current damping to the FPI.

Additional design parameters affect a flux-pinned interface. Effects not investigated in this chapter include:

- The effects on stiffness and damping of other configurations of magnets and superconductors, including those with both elements on each face of an FPI.
- The effect of changing the amount of superconductive material present, such as using a thin-film superconductor which may provide high stiffness with some mass savings.

Further work on the flux-pinned interfaces described in this paper will allow us to begin the design process for flux-pinned, modular space systems; potentially with the ability to reconfigure their structures by forming kinematic mechanisms.

## CHAPTER 5

### MICROGRAVITY DEMONSTRATIONS OF FLUX PINNING FOR STATION-KEEPING AND RECONFIGURATION OF CUBESAT-SIZED SPACECRAFT

This chapter reports the results of two demonstrations of magnetic flux pinning technologies implemented on CubeSat-sized spacecraft during microgravity flights as part of the NASA Facilitated Access to the Space Environment for Technology Development and Training (FAST) program in August 2009. In the first experiment, a CubeSat mockup flux pinned to a CubeSat-scale vehicle carrying superconductors and demonstrated low-stiffness, non-contacting, passive station-keeping in six degrees of freedom (6DOF). The second experiment studied the reconfiguration of two CubeSat mockups between equilibrium configurations via a revolute joint formed by a flux-pinned non-contacting kinematic mechanism. The spacecraft rotated about an axis defined by the flux-pinned interface rather than their respective centers of mass. These microgravity flight results highlight the role magnetic flux pinning might play in future small satellite operations.

Each experiment was performed on a microgravity aircraft with two free-floating

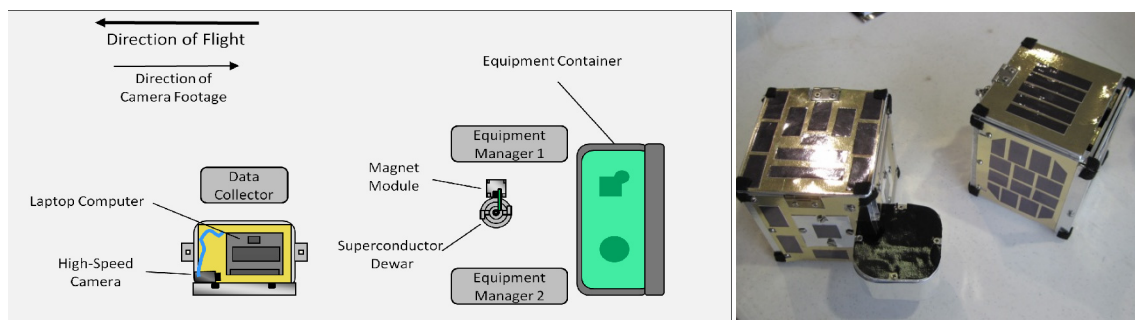


*Fig. 5-1 (Left) Top-down diagram of the experimental setup on the microgravity flight. The laptop computer and equipment container were secured to the floor of the aircraft, while the magnet modules and superconductor Dewar floated freely during the microgravity portions of the flight. Camera views in this note are from the left to the right on this diagram. (Right) Photograph of the two free-floating magnet modules used in these experiments. The left of the image shows the revolute joint module, and the right of the image shows the 6DOF station-keeping magnet module.*

modules: one containing an array of magnets appropriate to the experiment, and the other containing superconductors in a Dewar of liquid nitrogen. Three experimenters participated in each flight – two equipment managers to monitor the position of the free-floating modules at all times, and one data collector who operated the motion-capture camera. Fig. 5-1 is a diagram of the test setup.

This material has been published as “Microgravity Demonstrations of Flux Pinning for Station-Keeping and Reconfiguration of CubeSat-Sized Spacecraft” in the *Journal of Spacecraft and Rockets* [49].

## 5.1 6DOF Station-Keeping Demonstration

A basic structure of a flux-pinned interface for a modular pair of spacecraft includes a cryocooled superconductor on one module and one or more permanent magnets in an array on the other. The cooling system must “field cool” the superconductor in the presence of the magnet array to imprint the magnetic field distribution into the superconductor. This process establishes the equilibrium position and orientation of the magnets and superconductor as their position and orientation when the superconductor first cools below its critical temperature. In order to keep the superconductors, yttrium barium copper oxide or YBCO, below their critical

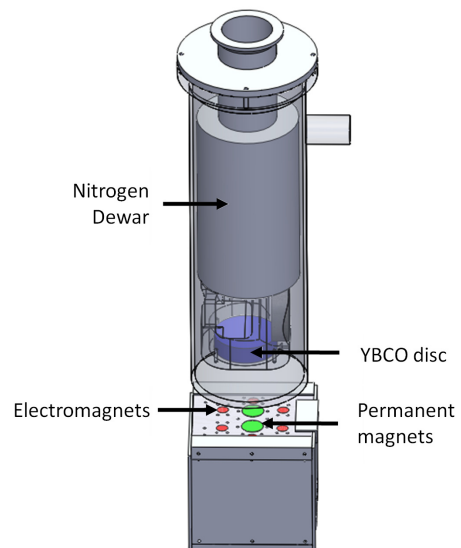


Fig. 5-2 Diagram of the 6DOF magnet module cube in flight position relative to the cylindrical superconductor Dewar. The superconductor is mounted at the bottom of the Dewar and the magnets are located on the top face of the cube (permanent magnets in green; electromagnets in red).



*Fig. 5-3 Still photos of the low-stiffness 6DOF station keeping demo. The superconductors are located at the bottom face of the insulated superconductor carrier; magnets are in the top face of the CubeSat mockup. (Photo on right courtesy of NASA.)*

temperature of 88 K, the superconductor-carrying module includes a 0.8 L liquid nitrogen Dewar with two YBCO disks mounted in vacuum at the bottom of the Dewar cylinder. A phase separator and relief valve at the top of the Dewar allow nitrogen gas boiloff to escape while keeping the cryogenic liquid sealed inside. The entire superconductor carrier is approximately the size of a 3U (30×10×10 cm) CubeSat spacecraft. The second module is a mockup of a 1U (10× 10×10 cm) CubeSat. It includes a microcontroller, batteries, BlueTooth communications, and an array of NdFeB permanent magnets. The permanent magnet array consists of two cylindrical magnets with their faces aligned to one cube face. Since this array does not have any rotational symmetry, the flux-pinned connection has nonzero stiffness in all six rigid-body degrees of freedom. During the experiment, the magnet module was arranged such that the face containing all of the magnets directly faced the superconductor insider the Dewar, as shown in Fig. 5-2.

During each low-g parabola of the microgravity flight, experimenters removed the CubeSat mockup and superconductor carrier from a protective case and positioned them within flux-pinning distance of one another. Still cameras and 100 frames-per-

second (FPS) video documented the mockup spacecraft as they demonstrated flux pinning (Fig. 5-3). The photos show magnet-superconductor separations ranging from a few centimeters up to approximately 5 cm. At these separation distances, and with two small permanent magnets in the CubeSat

(2.54 cm diameter, 30 g mass, approximately 2.5 J/T dipole moment), the stiffness provided by flux pinning is only a few newtons per meter (Chapter 4). Video data from the microgravity flight support this expectation of low-stiffness behavior.

## 5.2 Revolute Joint Demonstration

The revolute joint, or hinge, demonstration consists of the same superconductor carrier Dewar and a second CubeSat mockup. This mockup is a 10×10×10 cm cube with an arm, projecting from one edge, containing a large cylindrical NdFeB permanent magnet. The dipole axis of this magnet, aligned with the cube edge and displaced approximately 9.5 cm from the cube center, forms a non-contacting revolute joint when flux-pinned to a superconductor. Electromagnets on the cube faces to either

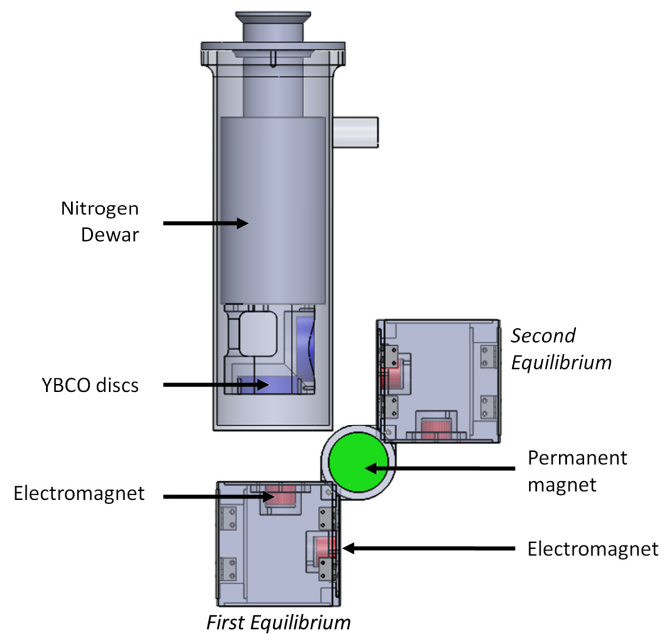


*Fig. 5-4 Diagram of the revolute joint magnet module at its two equilibrium states relative to the superconductor Dewar. The axis of the flux-pinned revolute joint is at the center of the permanent magnet, pointing out of the page.*

side of the hinge-axis magnet provide a means to lock the joint at both extremes of its motion by introducing additional stiffness between the activated electromagnet and superconductor. This system is a fully three-dimensional realization of an analogous air-levitated system from the laboratory [37].

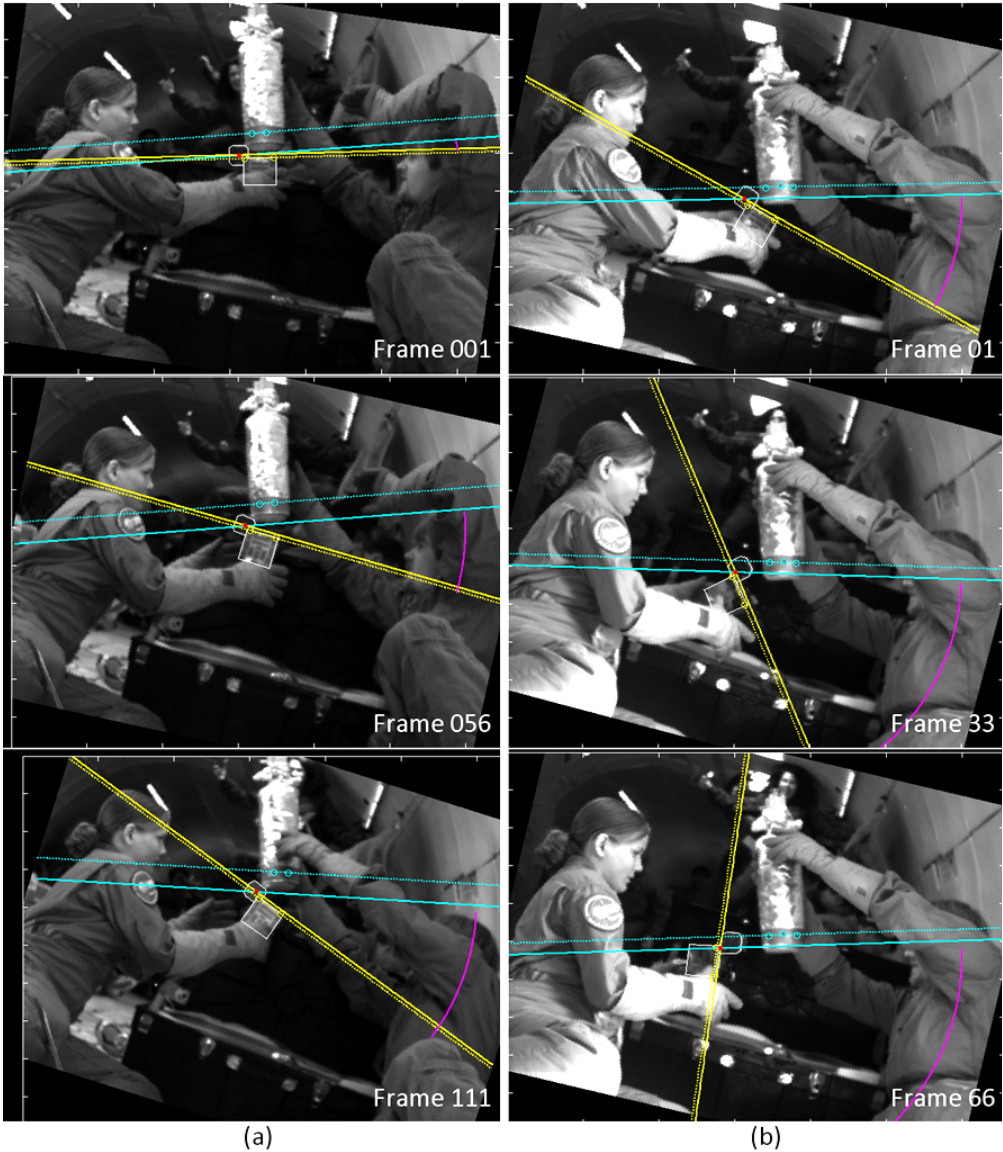


Fig. 5-5 Demonstration of a flux-pinned hinge on a CubeSat mockup at 100 FPS. (a) Flux pinning stiffens the translational motion of the CubeSat, which rotates about the hinge axis of the magnet (intersection of the solid lines). (b) Flux pinning does not prevent the CubeSat from drifting away from the superconductor carrier and the estimate of the hinge axis wanders off of the magnetic axis.

High-speed videos from the microgravity flight demonstrate that this hinge mockup coupled to the superconductor carrier with higher stiffness than the first CubeSat mockup pinned in 6DOF. The enhanced pinning stiffness is because the hinge-axis magnet is more powerful than the permanent magnets from the 6DOF station-keeping demonstration. However, there was near-zero stiffness between the superconductor carrier and hinged CubeSat about a rotation axis defined by the magnetic dipole axis in the protruding arm. Fig. 5-5 demonstrates that flux pinning constrains the two modules to move only in rotation about the hinge magnet axis. The frames in Fig. 5-5 are stills from a 100 FPS video, rotated so that the superconductor Dewar remains fixed throughout the movie. The CubeSat and Dewar remain at a close separation distance throughout the 1.1 s video. Motion capture of points on the Dewar and CubeSat provides data for an estimate of the hinge axis, shown at the point where the solid lines intersect. When the hinge is fully closed, these solid lines overlie one another. On the left, Fig. 5-5(a), the YBCO pins flux and the estimate of the hinge rotation axis remains on the dipole axis of the hinge magnet. The CubeSat swings away from the Dewar due to the residual angular momentum after the experimenters released the vehicles. Fig. 5-6 shows the rotation angle of the hinge as a function of time. The rotation is at a constant rate, demonstrating that angular momentum is conserved about the hinge axis. The noise level of this plot is due to motion tracking errors in the video postprocessing.

In Fig. 5-5(b), the frames on the right, the liquid nitrogen has boiled off from the Dewar and the YBCO is no longer below its critical temperature. After the experimenter releases the CubeSat, the module fails to maintain the close separation distance to the superconductors that would be seen in the presence of flux pinning. In addition, the estimate of the hinge rotation axis wanders off the hinge magnet's dipole

axis, leaving the body of the CubeSat and arm enclosure of the hinge magnet entirely by the end of the 0.66 s video. This motion capture analysis of the video demonstrates that flux pinning constrains the superconductor carrier and

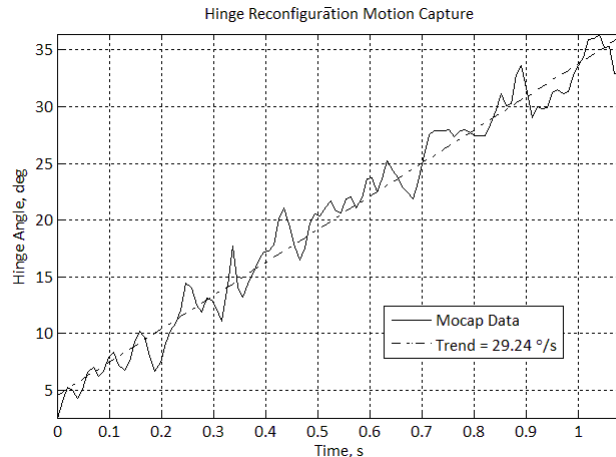


Fig. 5-6 Rotation angle between the flux-pinned CubeSat mockup and superconductor carrier about the hinge axis.

CubeSat mockup to rotate about a specific joint axis, which is defined by the dipole axis of the powerful hinge magnet. Without flux pinning, the CubeSat tumbles about an axis running through its center of mass. The motion capture videos also provide information on the joint stiffness in the flux-pinned hinge. The in-frame distance from the estimated hinge axis to the motion-capture tracking points varies slowly over the course of the 111 video frames; the frequency of a sinusoid fit to this variation, averaged for all the tracking points, is 0.017 rad/s. The reduced mass of the Dewar and hinge module is 1.02 kg and the video frames have a resolution of 2.3 millimeters per pixel on the flux-pinned modules. Therefore, an upper limit on joint stiffness in the hinge is 7.3 N/m. This value agrees with data obtained in prior 1g experiments with similar magnets, superconductors, and separation distances (Chapter 4).

### 5.3 Chapter Conclusions

Magnetic flux pinning is a promising technology for spacecraft self-assembly and reconfiguration applications. This chapter reports the first demonstration of flux

pinning for station-keeping and kinematic reconfiguration of space systems in a microgravity environment. These CubeSat-scale experiments show that flux pinning can provide low-stiffness station keeping of spacecraft, and demonstrate an implementation of a flux-pinned, non-contacting revolute joint. The small scale of these demonstration mockup spacecraft illustrates that flux pinning hardware could be developed for larger spacecraft with larger power and mass budgets. A larger system could include more powerful magnets for higher-stiffness pinning, more powerful electromagnets for relative position and orientation actuation, or other enhanced capabilities. Future microgravity technology demonstrations involving flux pinning may make use of these concepts to demonstrate self-assembly and reconfiguration concepts with multiple flux-pinned mockup vehicles.

CHAPTER 6  
SIMULATION OF MULTIBODY SPACECRAFT RECONFIGURATION  
THROUGH SEQUENTIAL DYNAMIC EQUILIBRIA

This chapter reports the development of a simulation environment for exploring space system reconfiguration as a sequence of passive dynamical evolutions with chosen sets of kinematic constraints. These simulations are based on the formulation of equations of motion from Udwadia and Kalaba, because of the ease with which that formulation accounts for kinematic constraints [50]. Section 6.1 describes the sequential-equilibrium multibody spacecraft reconfiguration concept at a high level. Section 6.2 then develops equations of motion, with the Udwadia-Kalaba technique augmented by quaternion states and Euler's equation for rigid body dynamics, for implementation in simulations. Using these simulations, Section 6.3 explores possible reconfigurations of example spacecraft systems and develops methods to identify reconfiguration maneuvers for general systems. Furthermore, this simulation environment provides tools for the analysis of the air-levitated testbed and microgravity flight experiments, and suggests conclusions about optimization of reconfiguration maneuvers and dynamic stability of reconfiguring systems.

The material comprising this chapter appeared as Shoer, J., and Peck, M. "Simulation of Multibody Spacecraft Reconfiguration through Sequential Dynamic Equilibria," *AIAA Guidance, Navigation, and Control Conference*, Toronto, ON, 2010. It has been submitted as "High-level Reconfiguration Controllers for Multibody Spacecraft with Switchable Kinematics" to the *Journal of Guidance, Control, and Dynamics* and "Udwadia-Kalaba Dynamics for Constrained Rigid Body Systems with Quaternion Attitude Representations" to the *Journal of Applied Mechanics*.

## 6.1 The Sequential-Equilibrium Reconfiguration Concept

A single point in an  $n$ -dimensional configuration space represents the physical configuration of a multibody system with  $n$  degrees of freedom. The configuration space may take the form of ordered  $n$ -tuples of, for example, joint angles and offsets [51]. Configuration space is thus related, but not identical, to state space. The architecture of a reconfigurable space system in this paradigm includes kinematic constraints, defining the locus of points in configuration space that the system may occupy. In this treatment, kinematic constraints appear as boundaries of the configuration space. The system may move continuously from point to point in configuration space as both external and internal forces act on the system, in accordance with the laws of motion. An important point for this reconfiguration concept is that specified alterations of the kinematic constraints are part of the control effort on the multibody system. That is, some of the control laws acting on the system involve changing the allowed trajectories in configuration space so that the system naturally evolves towards a desired configuration.

Given a multibody system represented by a point in configuration space, let us now introduce force fields to augment its dynamics with a potential function. This potential function is a scalar value associated with each point in configuration space, resulting from an application of internal or external forces or torques to the system—for instance, gravity gradient, interactions between a dipole on the spacecraft and a planetary magnetic field, solar radiation pressure, electromagnetic fields interacting between multibody spacecraft modules, or springs connecting spacecraft bodies. Now, depending on the shape of the potential function, there will be dynamic equilibria, represented by minima or “wells” in the potential, in configuration space. The system

will naturally move towards these equilibria and, assuming that the system is dissipative, will settle into the potential well in steady state. From the equilibrium, a new set of kinematic constraints and a new potential function could drive the system to evolve to a different equilibrium. The space system proceeds from one configuration to the next in a “stepping-stone” fashion until it reaches a target configuration. The following three steps identify the possible reconfiguration maneuvers a system may undergo:

1. Determine, from the possible kinematic constraints on the system, the allowed trajectories of the system in configuration space.
2. Set up a potential to create a stable equilibrium at a location in configuration space. Allow the system to evolve dynamically in simulation, settling into the resulting potential well.
3. If necessary, identify any newly allowed trajectories in configuration space and repeat the first two steps to move the system to another point in configuration space.

The applied control input at each discrete step in this process consists of a collection of the assigned kinematics of the multibody system and the potential  $U(x)$  from the applied force fields. At each stepping-stone configuration, the choice of kinematics and potential must be one of the allowable selections associated with that point in configuration space. Such selections will, in general, depend on the proximity of the various bodies and the properties of the joints in question. Similarly, the selection of  $U(x)$  must be a member of the finite set of possible functions related to the spacecraft capabilities and environment. Some potential functions, such as those due to gravity or rigid-body dynamics, will always be present. The inverse problem

(identifying sets of kinematics and potentials from desired configurations) will also be important.

The terminology of hybrid automata [52] applies to this description in a straightforward manner. The continuous modes of the automaton are each set of dynamics while the system kinematics remain constant;

that is, the dynamics of the

system at any configuration-space equilibrium and during the dissipative transition to that equilibrium. The possible collections of kinematics are the guards enabling discrete transitions. The invariants that cause the automaton to perform a discrete transition are conditions that the current configuration (represented by a state space vector  $x$ ) must be at a potential minimum,  $x_{eq} = (x | U(x) = \min U)$ . The control strategy in this chapter involves manipulating the invariants and guards to guide the hybrid execution of the automaton to a continuous mode with a desired equilibrium configuration  $x_{target}$ .

As an illustration of the process, consider a system consisting of two bodies in free space, with one of two possible joints linking them together. The bottom plane in Fig. 6-1 represents a two-dimensional configuration space for these bodies; for example, the separation between their centers of mass and their relative angle about an arbitrary axis. Control over this system consists of the choice of joint and the

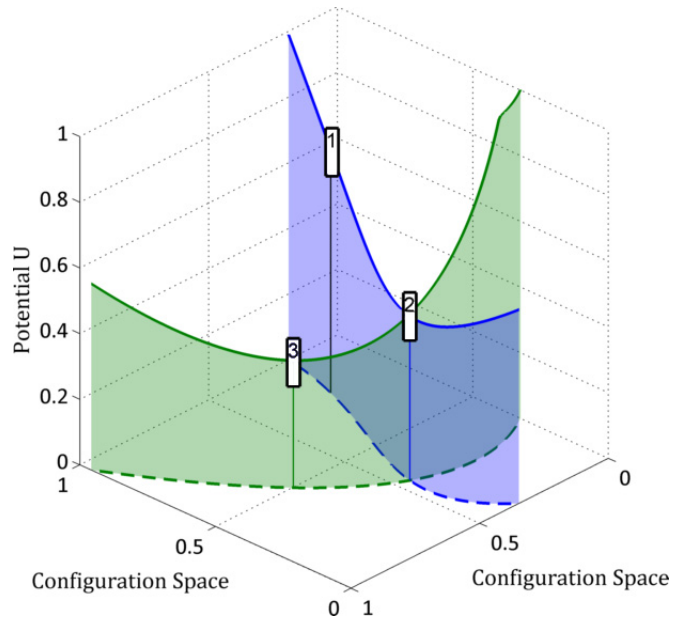


Fig. 6-1 Potential energies in the stepwise passive reconfiguration concept for a system with two possible degrees of freedom.

application of one of two arbitrary force fields to establish a potential function along the line of allowed configurations. The system starts at Point 1 in configuration space, with the kinematic constraint that the system must move along the blue dotted line in configuration space and a potential energy along that line given by the height of the blue curve (Fig. 6-1). The presence of a potential minimum will move the system from Point 1 to Point 2. This process may involve transient dynamics; the reconfiguration sequence does not proceed further until the system has reached steady state. If the new configuration is not the desired final configuration of the system  $x_{target}$ , another selection of kinematic constraints (such as the green dotted line) and potential function may drive the system to move to yet another configuration, such as from Point 2 to Point 3. Fig. 6-2 shows a possible time history of the system evolution.

There are several important points illustrated by this example. The first is that the system cannot reach Point 3 directly from Point 1, given the possible system kinematics. In a more complex system, kinematic constraints may not change only in character but also appear and disappear, so some configurations are certain to be impossible to reach from other configurations and intermediate steps will be necessary. This situation is the case in a system that engages and disengages some of its joints as the component bodies come close to or separate from one another. A second point is that this control strategy does

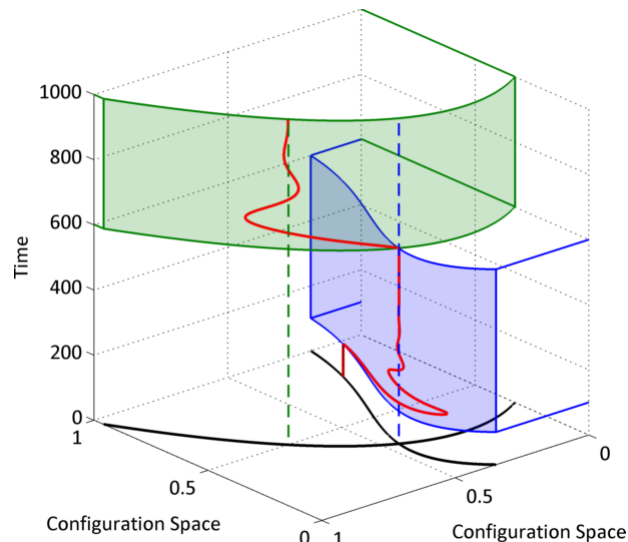


Fig. 6-2 Sample time history of the system from Fig. 6-1. The control input changes at  $t = 100$  s and  $t = 600$  s.

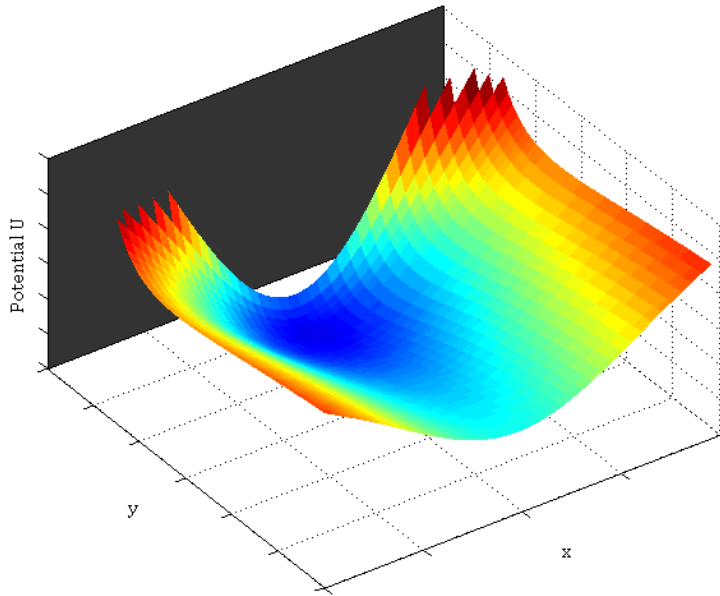


Fig. 6-3 Potential well linking a flux-pinned magnet and superconductor. The superconducting plane is shaded.

not require any sensing, computation, or feedback actuation of the system while it is between equilibria in configuration space. This controller requires only knowledge of the initial and final configurations for each step in the process, as long as the intermediate

dynamics meet any safety and robustness criteria (such as collision avoidance) which may be verified in simulation before the maneuver begins. It is a high-level, hybrid control scheme in which the continuous-time dynamics of the system are less relevant than the configuration space points at which the system dynamics change. On a space system with limited computation capabilities, determination of the locus of possible reconfiguration sequences may occur on the ground and either be transmitted on an as-needed basis or stored in spacecraft memory as a compact lookup table. The on-board reconfiguration controller need only know the desired configuration and determine a possible set of intermediate steps.

This control architecture is based on a large set of equilibria in configuration space, and the identification of reachable equilibria from the current system configuration. Graph theory provides a convenient language to describe the equilibria and the control inputs necessary to move the spacecraft system from one to another. In this paradigm, each reconfigurable space system has an associated “reconfiguration

graph.” The vertices of the reconfiguration graph represent each of the possible passively stable potential wells of the system in configuration space  $x$ , while the directed arcs represent the collections of kinematics and potentials that take the system from one configuration  $x$  to another  $x'$ . For application in a spacecraft system, the graph will be constructed offline according to the three-step process described above. Important questions for reconfiguration control, such as which configurations are reachable from a given initial configuration and which configurations, if any, are “sinks” from which the system cannot proceed further, will be answered from this graph. A well-constructed reconfiguration graph inherently prevents transient dynamics that include unsafe behaviors, as those transient dynamics could be identified in simulation and eliminated from the graph. Such a graph theoretical approach highlights how this reconfiguration paradigm allows spacecraft or spacecraft operators to concentrate on reconfiguration tasks from a high level, relegating the low-level evolution of the system from one configuration to another to passive physics.

One feature of flux pinning that makes it particularly attractive to this approach to reconfiguration is that it provides a means to establish stable potential wells in all six degrees of freedom. Fig. 6-3 shows a sketch of the potential well binding a flux-pinned permanent magnet to a superconducting plane in translation space,  $U(x, y)$ . A frozen-image model of flux pinning generated the data for this plot [45]. If the magnet does not have an axisymmetric field, similar potential wells keep the magnet stably positioned with respect to the superconductor in the remaining four degrees of freedom as well. Establishing such stable potential wells is critical to enabling reconfiguration with little active control, as it is the passive stability of these wells that allows this control strategy to ignore the continuous-time dynamics of the system when it moves from point to point in configuration space.

## 6.2 Formulation of Udwadia and Kalaba's Fundamental Equation with Quaternion Coordinates

### 6.2.1 Derivation of General Equation of Motion with Quaternion States

Udwadia and Kalaba offer an algorithm for finding equations of motion [50] for systems with constraints that can be expressed in terms of the second derivative of the system's generalized coordinates  $x$ , i.e., in terms of an array of accelerations:

$$A(x, \dot{x}, t)\ddot{x} = b(x, \dot{x}, t). \quad (6-1)$$

The coordinates  $x$  consist of all  $n$  positions and orientations for the bodies in the system, and the matrices  $A$  and  $b$  ( $m \times n$  and  $m \times 1$ , respectively, with elements that may depend on the system kinematics and time) express the  $m$  constraint equations. In the presence of applied forces  $F$  such that

$$F = Ma, \quad (6-2)$$

where  $M$  is the system mass matrix and  $a$  is the matrix of coordinate accelerations *in the absence of all constraints* (6-1) (in other words,  $F$  includes no constraint forces), the following is the equation of motion of the system:

$$M\ddot{x} = F + A^T(AM^{-1}A^T)^+(b - AM^{-1}F). \quad (6-3)$$

The superscript  $+$  indicates a Moore-Penrose matrix pseudoinverse. Eq. (6-3) is one of several possible expressions of Udwadia and Kalaba's Fundamental Equation. It can be evaluated analytically, by hand or in a symbolic computation environment, or numerically at every time step of a numerical integration.

Evaluating the prospects of the proposed reconfiguration concept requires a simulation environment that can accommodate bodies with arbitrary positions and

orientations in six degrees of freedom (6DOF). In the process of computing a reconfiguration maneuver as a sequence of dynamical evolutions, there are not necessarily any guarantees on the orientation of each body in an arbitrary multibody system at the end of each evolution. Therefore, the equations of motion should not be susceptible to singularities if the bodies take certain orientations, such as those associated with Euler angles and any other global, three-parameter attitude representation. To this end, the coordinates of each body  $B$  (in an inertial frame) are expressed as its center-of-mass position and quaternion:

$${}^N x_B = \begin{bmatrix} {}^N r_B \\ {}^N q^B \end{bmatrix}. \quad (6-4)$$

${}^N q^B = [({}^N q_{123}^B)^T \quad {}^N q_4^B]^T$  denotes the quaternion relating the rotation from axes fixed in body  $B$  to reference axes in  $N$ —associated with an inertially fixed basis—with superscripts analogous to the notation for direction-cosine matrices,  ${}^N Q^B$ .

The equation of unconstrained motion in the positions for one body is straightforward:

$${}^N f_B = m_B {}^N \ddot{r}_B \quad (6-5)$$

However, in order to account for rigid-body kinematics, Eq. (6-2) must include not only the force  $f_B$  on the body center of mass but also terms due to Euler's equation for rigid body motion with a torque on body  $B$ ,

$$\boldsymbol{\tau}_B = \mathbf{I}_B \cdot \dot{\boldsymbol{\omega}}^{B/N} + \boldsymbol{\omega}^{B/N} \times \mathbf{I}_B \cdot \boldsymbol{\omega}^{B/N}. \quad (6-6)$$

In  $B$ , the angular velocity and derivative of the angular velocity can be expressed in terms of the quaternion elements. This approach allows the portion of Eq. (6-2)

dealing with rotational coordinates for each body to be recast with an effective mass matrix and effective force. Suppressing the superscripts on  ${}^N q^B$  for brevity, the transformation between angular velocity and quaternion derivative is:

$$\begin{aligned} {}^B \omega^{B/N} &= 2[(-q_{123}^\times + q_4 \mathbf{1}_3) \quad -q_{123}] \dot{q} \\ {}^B \omega^{B/N} &= T(q) \dot{q} \end{aligned} \quad (6-7)$$

with a superscript  $^\times$  denoting the  $3 \times 3$  skew-symmetric cross-product matrix form of a  $3 \times 1$  matrix and  $T^T T = T T^T = \mathbf{1}_3$ . Euler's equation then becomes

$${}^B I_B (\dot{T} \dot{q} + T \ddot{q}) = {}^B \tau_B - (T \dot{q})^\times {}^B I_B (T \dot{q}) \quad (6-8)$$

$${}^B \tau_B - (T \dot{q})^\times {}^B I_B (T \dot{q}) - {}^B I_B \dot{T} \dot{q} = {}^B I_B T \ddot{q} \quad (6-9)$$

This expression is analogous to Eq. (6-5), but the matrix  ${}^B I_B T$ , which serves as the mass matrix, is  $3 \times 4$ . Eq. (6-3) requires a square system mass matrix; so, we pre-multiply Eq. (6-9) by the transpose of the transformation matrix  $T^T$ :

$$\begin{aligned} T^T {}^B \tau_B - T^T (T \dot{q})^\times {}^B I_B (T \dot{q}) - T^T {}^B I_B \dot{T} \dot{q} &= T^T {}^B I_B T \ddot{q} \\ \tilde{F}_B(q, \dot{q}, \tau_B) &= \tilde{M}_B(q) \ddot{q} \end{aligned} \quad (6-10)$$

As a check, note that

$$\frac{1}{2} \dot{q}^T \tilde{M}_B \dot{q} \quad (6-11)$$

gives the correct rotational kinetic energy expression for the body.

The effective force and mass matrices for body  $B$  are, therefore,

$$F_{B,eff} = \begin{bmatrix} {}^N f_B \\ \tilde{F}_B(q, \dot{q}, \tau_B) \end{bmatrix} \quad (6-12)$$

$$M_{B,eff} = \begin{bmatrix} m_B \mathbb{1}_3 & \mathbb{0}_{3 \times 4} \\ \mathbb{0}_{4 \times 3} & \tilde{M}_B(q) \end{bmatrix} \quad (6-13)$$

for use in Eq. (6-3). The effective force matrix for the entire system consists of a stack of the effective force matrices of each body, and the system effective mass matrix is comprised of a block matrix of each body's effective mass matrix.  $M_{B,eff}$  is rank-deficient because of the transformation from three-element angular velocity vectors to four-element quaternion derivatives. Fortunately, Udwadia and Phohomsiri [53] provide a form of Eq. (6-3) that handles singular mass matrices and redundant coordinates,

$$\ddot{x} = \begin{bmatrix} (\mathbb{1} - A^+A)M_{eff} \\ A \end{bmatrix}^+ \begin{bmatrix} F_{eff} \\ b \end{bmatrix}, \quad (6-14)$$

provided that the constraint matrices  $A$  and  $b$  include any constraints among redundant coordinates. In the case of quaternion states,  $A$  and  $b$  include the second derivative of the constraint that the norm of any quaternion must equal 1,

$$\begin{aligned} \frac{d^2}{dt^2} (q^T q = 1) \\ 2q^T \ddot{q} + 2\dot{q}^T \dot{q} = 0. \end{aligned} \quad (6-15)$$

This is the form of Eq. (6-3) that we have implemented in a set of MATLAB toolbox functions.

### 6.2.2 Constraint Matrices for Joints with Quaternion Coordinates

The constraint matrix corresponding to a joint connecting, for example, bodies  $B$  and  $C$  must conform to the following template:

(6-16)

$A$  has zeros in all other elements. For example, if a spherical joint connecting bodies  $B$  and  $C$  is located at the point  $\mathbf{p}_{BC}$  from body  $B$ 's center and  $\mathbf{p}_{CB}$  from body  $C$ 's center, the second derivative of the single vector constraint

(6-17)

The constraint matrix elements, with full superscripts, are

$$\begin{aligned}
 A_{r_B} &= \mathbf{1}_3 \\
 A_{N_{q^B}} &= -\left({}^N Q^B \mathbf{p}_{BC}\right)^\times {}^N Q^B T_B \\
 A_{r_C} &= -\mathbf{1}_3 \\
 A_{N_{q^C}} &= \left({}^N Q^C \mathbf{p}_{CB}\right)^\times {}^N Q^C T_C \\
 b &= \left(\left({}^N Q^C T_C \dot{q}_C\right)^\times\right)^2 {}^N Q^C \mathbf{p}_{CB} - \left({}^N Q^C \mathbf{p}_{CB}\right)^\times {}^N Q^C \dot{T}_C \dot{q}_C \\
 &\quad - \left(\left({}^N Q^B T_B \dot{q}_B\right)^\times\right)^2 {}^N Q^B \mathbf{p}_{BC} + \left({}^N Q^B \mathbf{p}_{BC}\right)^\times {}^N Q^B \dot{T}_B \dot{q}_B.
 \end{aligned} \tag{6-18}$$

One expression for the constraint matrices for a revolute joint or hinge with its rotation axis aligned with a unit vector  $\mathbf{u}$  that is fixed on the body  $B$  is a combination of two spherical joints displaced along the rotation axis from one another:

$$\begin{aligned}
A_{r_B} &= \begin{bmatrix} 1_3 \\ 1_3 \end{bmatrix} \\
A_{N_{q^B}} &= \begin{bmatrix} -\left({}^N Q^B ({}^B p_{BC} + {}^B \hat{a})\right)^\times {}^N Q^B T_B \\ -\left({}^N Q^B ({}^B p_{BC} - {}^B \hat{a})\right)^\times {}^N Q^B T_B \end{bmatrix} \\
A_{r_C} &= -\begin{bmatrix} 1_3 \\ 1_3 \end{bmatrix} \\
A_{N_{q^C}} &= \begin{bmatrix} \left({}^N Q^C ({}^C p_{CB} + {}^C Q^B {}^B \hat{a})\right)^\times {}^N Q^C T_C \\ \left({}^N Q^C ({}^C p_{CB} - {}^C Q^B {}^B \hat{a})\right)^\times {}^N Q^C T_C \end{bmatrix} \\
b &= \begin{bmatrix} \left(\left({}^N Q^C T_C \dot{q}_C\right)^\times\right)^2 {}^N Q^C ({}^C p_{CB} + {}^C Q^B {}^B \hat{a}) \\ + \left({}^N Q^C ({}^C p_{CB} + {}^C Q^B {}^B \hat{a})\right)^\times {}^N Q^C \dot{T}_C \dot{q}_C \\ - \left(\left({}^N Q^B T_B \dot{q}_B\right)^\times\right)^2 {}^N Q^B ({}^B p_{BC} + {}^B \hat{a}) \\ - \left({}^N Q^B ({}^B p_{BC} + {}^B \hat{a})\right)^\times {}^N Q^B \dot{T}_B \dot{q}_B \\ \left(\left({}^N Q^C T_C \dot{q}_C\right)^\times\right)^2 {}^N Q^C ({}^C p_{CB} - {}^C Q^B {}^B \hat{a}) \\ + \left({}^N Q^C ({}^C p_{CB} - {}^C Q^B {}^B \hat{a})\right)^\times {}^N Q^C \dot{T}_C \dot{q}_C \\ - \left(\left({}^N Q^B T_B \dot{q}_B\right)^\times\right)^2 {}^N Q^B ({}^B p_{BC} - {}^B \hat{a}) \\ - \left({}^N Q^B ({}^B p_{BC} - {}^B \hat{a})\right)^\times {}^N Q^B \dot{T}_B \dot{q}_B \end{bmatrix} \tag{6-19}
\end{aligned}$$

The second derivatives of other joint constraint equations generate other constraint matrix elements in the same manner. A simple vertical stack of the constraint matrix for each of the joints accommodates many joints in a multibody system:

(6-20)

This system-constraint matrix can include nonholonomic and redundant constraints when implemented for simulation. For example, the revolute constraint matrices of Eq. (6-19) have six equations representing only five independent constraints.

## 6.3 Simulation of Sequential Multibody Reconfiguration

An object-oriented MATLAB implementation of the constraint equation and equation of motion from Section 6.2 provides an intuitive and extensible simulation environment. The key classes of this simulation environment toolbox are the following:

- *Body* objects, which store the physical properties and track the position and quaternion coordinates of a rigid body, as well as providing graphical representations of bodies for animation;
- *Joint* objects, which supply the kinematic constraint matrices (e.g. Eq. (6-18) or (6-19)) between connected bodies;
- *Force* objects, which represent force and torque functions on bodies;
- *Sensor* objects, which are attached to bodies and can halt simulations of multibody motion when they come into proximity with one another; and
- *Multibody* objects, which act as containers for all the above classes, specify information relevant to entire systems such as potential energy functions, use Eqs. (6-12), (6-13), and (6-14) with MATLAB's ordinary differential equation integrators to solve equations of motion, and include various plotting and animation functions for analyzing the motion of multibody systems.

These toolbox functions are available on the Internet at <http://www.spacecraftresearch.com/flux/quirk>. The implementation easily accommodates simple multibody mechanisms, and provides the means to develop an algorithm to construct the reconfiguration graph of a multibody system with switchable kinematic constraints through direct simulation, as Section 6.1 describes.

The simulation algorithm is a design tool to determine the set of reachable equilibrium configurations of a multibody spacecraft as a means of evaluating the locations of possible joint sites on individual bodies and the potential energies the system can produce. It takes the brute-force approach of enumerating all possible joint layouts and potential energies of a system and simulating the resulting multibody dynamics to identify reachable equilibrium positions. With the system at those equilibria, the program enumerates and simulates possible joint layouts again. This algorithm proceeds as follows:

1. Set up bodies in their initial configuration and set initial potential energy.
2. Place sensor objects at locations on bodies where joint connections are possible.
3. Add a single node to a graph object. Label this node with the current configuration of the bodies. Add this node to a list of nodes that require processing.
4. Loop through each node in the processing list.
  - 4.1. Enumerate all possible combinations of joints (where compatible sensors are in proximity) and potential energy functions at the configuration of bodies represented by the node label.
  - 4.2. Loop through all combinations of joint set and potential energy selections.
    - 4.2.1. Place selected joints on bodies and set multibody system potential energy.
    - 4.2.2. Simulate the motion of the multibody system until either the system reaches equilibrium, two sensors come into proximity, or bodies collide.

4.2.3. Check the configuration of the bodies after simulation against safety criteria. If safety criteria are violated (for example, if one of the bodies separates from the rest or bodies collide during simulation), terminate this iteration of the loop.

4.2.4. Check the configuration of the bodies after simulation against the configurations represented by all extant node labels in the graph. If the configuration does not match any existing nodes, label a new node and add it to the graph.

4.2.5. Add a directed edge to the graph, representing the transition between the node being processed and the newly generated node. Label this edge with the joint set and potential energy selection for this iteration.

4.3. Remove the processed node from the processing list.

5. Save the reconfiguration graph of the system.

Given enough time and computing power, this approach will construct the entire reconfiguration graph for an arbitrarily complex system. The graph can then be evaluated based on system design criteria.

### 6.3.1 Simulation of Two-Equilibrium Laboratory Demonstrations

Consider the following reconfiguration example, which reproduces the results of laboratory demonstrations with two flux-pinned, CubeSat-sized spacecraft mockup modules on an air table [37] and a NASA microgravity flight (Chapter 5). One cube-shaped module (blue in Fig. 6-4) is inertially fixed, while the other (red) is attached to the first module by a hinge with its rotation axis aligned with the bodies'  $z$  axes.

Sensor objects detect when the cubes' faces align and terminate simulation with the

cubes locked together in these positions. There are two possible potential energy functions, with a potential well either in the positive  $x$  or negative  $y$  direction from the center of the blue cube. Selection of one potential energy function or the other determines the system's equilibrium. The algorithm successfully computes the reconfiguration graph of this system, which consists of two nodes representing the two configurations in Fig. 6-4 connected by two directed edges representing each of the two potential energy selections. In the physical systems, combinations of magnets, electromagnets, and superconductors realize these potential energies. A simple extension of the system, with possible joints at each of the vertical edges of the cubes and four potential wells located near each face of the blue cube, gives a four-node reconfiguration graph and allows the red cube to “walk” all the way around the perimeter of the blue module.

This system is entirely passive during the reconfiguration from one equilibrium to another. A plot of the system's total energy appears in Fig. 6-5. Total energy decreases because there is some dissipation in the multibody system to encourage numerical stability. During the motion, the system does not use power except that which is necessary to maintain the potential energy functions. In the case of the laboratory

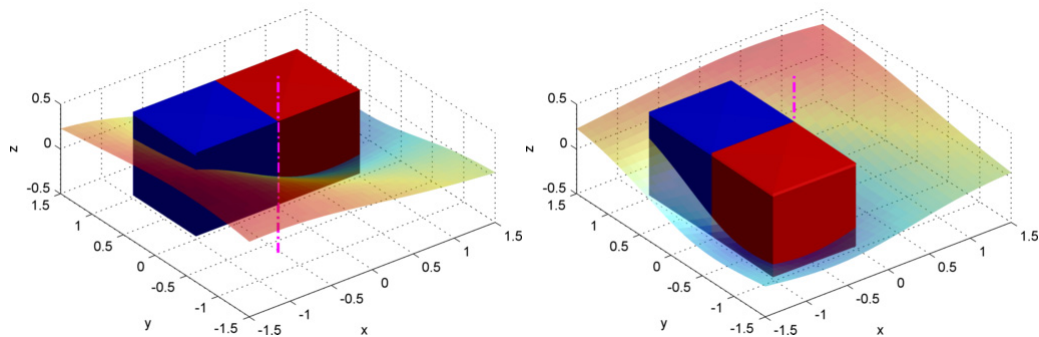


*Fig. 6-4 First reconfiguration example: multibody system equilibria at two nodes in the reconfiguration graph. The dashed line indicates the rotation axis of a revolute joint. The shaded surface's height shows the potential energy as a function of  $x$  and  $y$  position of the bodies.*

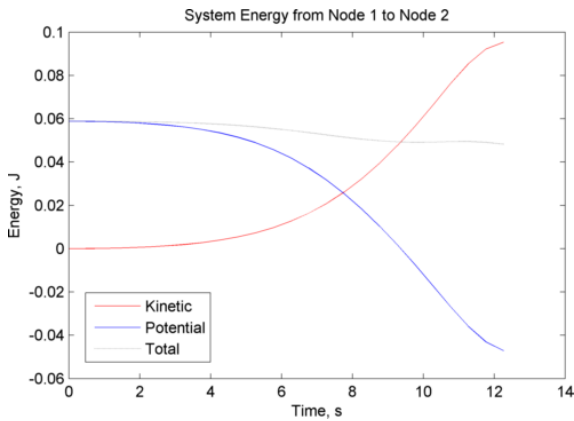


Fig. 6-5 System energy as a function of time.

demonstrations, there is constant power supplied to electromagnets during the motion. However, the potential energy functions could also be realized by permanent magnets that move or rotate to change between the two potentials. In that case, at the point when a new reconfiguration maneuver begins, the system must perform work equal to at

least the difference between the value of the previous potential energy and the value of the new potential energy at the same state of the system. For the identical potential wells of Fig. 6-4, this change in energy is the difference between the values of the potential energy at the beginning and end of the time series shown in Fig. 6-5. For other systems, such power expenditures must be considered against the power consumed by a low-level feedback control system to determine which approach is advantageous.

### 6.3.2 Planetary Imaging Mission

A second example of a reconfigurable system with a kinematically defined reconfiguration graph is an innovative planetary imaging mission consisting of a spacecraft with four identical CubeSat-scale modules. Each module has a suite of cameras or other instruments, a set of possible revolute or fixed joint locations, and the capability to energize or reorient magnetic fields to choose between four potential energy functions. Fig. 6-6 shows the initial configuration of the spacecraft, with possible joint sites marked. Each joint site can be fully free, fully fixed, or a revolute

joint. The potential energy functions in simulation are scaled to the size and shape of magnetic flux pinning potential wells for magnets and superconductors of similar size to those in the laboratory demonstrations from the previous section. A sketch of the spacecraft's reconfiguration graph, as identified by the simulation algorithm, appears in Fig. 6-7.

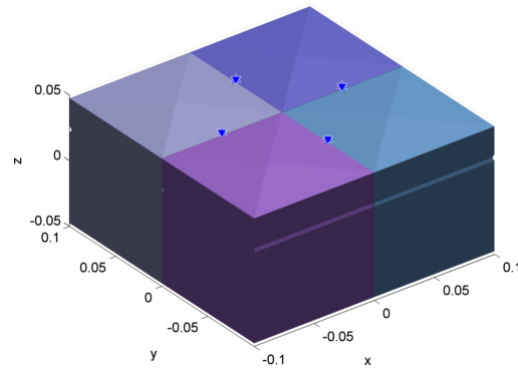


*Fig. 6-6 Initial setup of the CubeSat-based imaging mission. Blue dots represent possible joint locations.*

Many configurations in Fig. 6-7 serve a mission purpose by changing the orientation of the various instruments, solar panels, and other hardware on the spacecraft cube faces. For example, the initial configuration (1) is appropriate for launch and for injection into a transfer orbit to the target planet. Configuration (2) in Fig. 6-7 is a compact arrangement of modules with cameras and instruments facing slightly outward, giving the spacecraft wide-angle imaging capabilities for acquiring context images. Configuration (3) is a linear formation that allows its cameras to sweep across large swaths of the planetary surface. This layout may efficiently acquire a planetary map or cover the same ground with multiple instruments; or, if the imaging fields overlap, it may acquire stereo images on the same orbital pass. The reconfiguration graph also reveals undesirable configurations and transitions: for example, configuration (3) contrasts with configuration (4), which has a similar system layout but has no outgoing transitions. Unless the design of possible joint locations on the spacecraft changes or the spacecraft is capable of generating different potential energy functions, the spacecraft should avoid this “sink” configuration. To

that end, designers may choose to prune node (4) from the graph before installing the graph in the spacecraft controller.

Each configuration of the spacecraft is a dynamic equilibrium, and each transition is free of collisions. No active control is applied during transitions. A software or control problem on the spacecraft therefore results in one of several relatively benign failure modes that do not involve hardware damage. If a control failure occurs when the spacecraft is at an equilibrium configuration, then the spacecraft remains in that configuration. If, however, the failure occurs while the spacecraft is carrying out a maneuver, then the system continues to move until it reaches dynamic equilibrium. In either case, the system remains passively stable, with kinematic constraints that prevent motions with any danger of collisions. Only a hardware failure of the joints

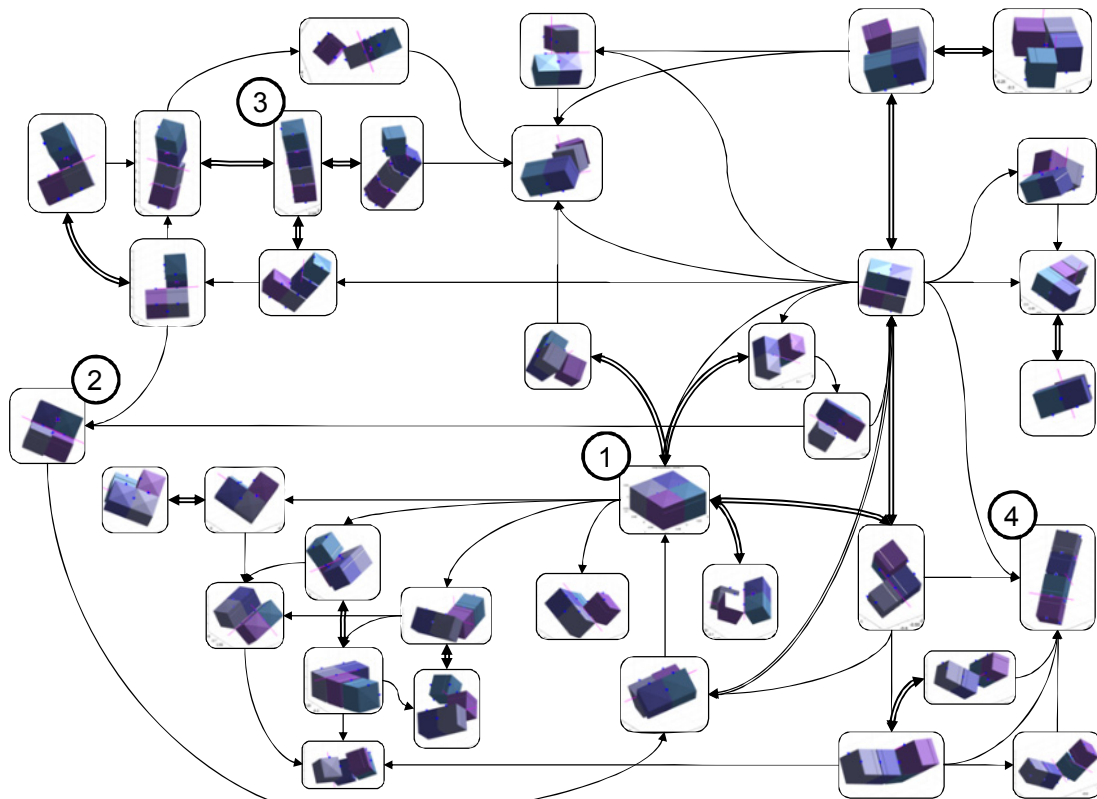


Fig. 6-7 Equilibrium configurations and directed reconfiguration graph of an example system.

themselves could pose a physical danger to the spacecraft.

One of the strengths of this reconfiguration methodology is that it can identify opportunities for emergent behaviors. For example, the different arrangements of cameras in Fig. 6-7 may allow the spacecraft to function as a set of filter masks for interferometry that emphasizes different spatial scales depending on the configuration. In addition, the enumeration of all possible equilibrium configurations of the space system may identify configurations that enable otherwise unanticipated functionality, or it may identify sequences of reconfigurations that reach a desired end state in some advantageous way. The prospect for such emergent behaviors increases with system complexity, as the algorithm enumerates many more possible transitions.

In this system, internal forces provided by the modules realize the potential energy functions. Ambient forces such as gravity gradient may allow advantageous orientations of the entire system, but do not drive reconfigurations. The spacecraft therefore must provide power to realize the inter-body forces. If electromagnets establish the potential wells, there will be constant power usage over the course of each transition along the graph; if, however, the spacecraft moves permanent magnets to enable each transition, power usage will occur in discrete bursts at the beginning of each step in the reconfiguration process. Other spacecraft systems may rely on ambient forces to drive the dynamics and, depending on the specific sequence of reconfigurations, the spacecraft might use very little power; or it might perform power-intensive maneuvers very infrequently. Again, a trade study must compare the power usages of this reconfiguration method and one involving feedback control and actuation in the context of this mission.

### 6.3.3 Imaging Mission Graph-Weighting Schemes

The ability to access the multibody system state while simulating transitions between equilibrium configurations offers the opportunity to generate many mission-relevant weighting schemes for a reconfiguration graph. With a weighted graph, the reconfiguration controller becomes an optimal controller in the sense that spacecraft maneuvers may maximize or minimize the metrics labeling each graph edge. These metrics could involve solar panel light incidence, system thermal considerations, measures of ground coverage, amount of power required to maintain potential wells, or time elapsed during each maneuver. Standard graph-search algorithms, such as Dijkstra’s Algorithm [54], are well-known and computationally efficient to implement when compared with multi-vehicle full-state feedback controllers.

One such weighting scheme appears in Fig. 6-8. During simulation of each

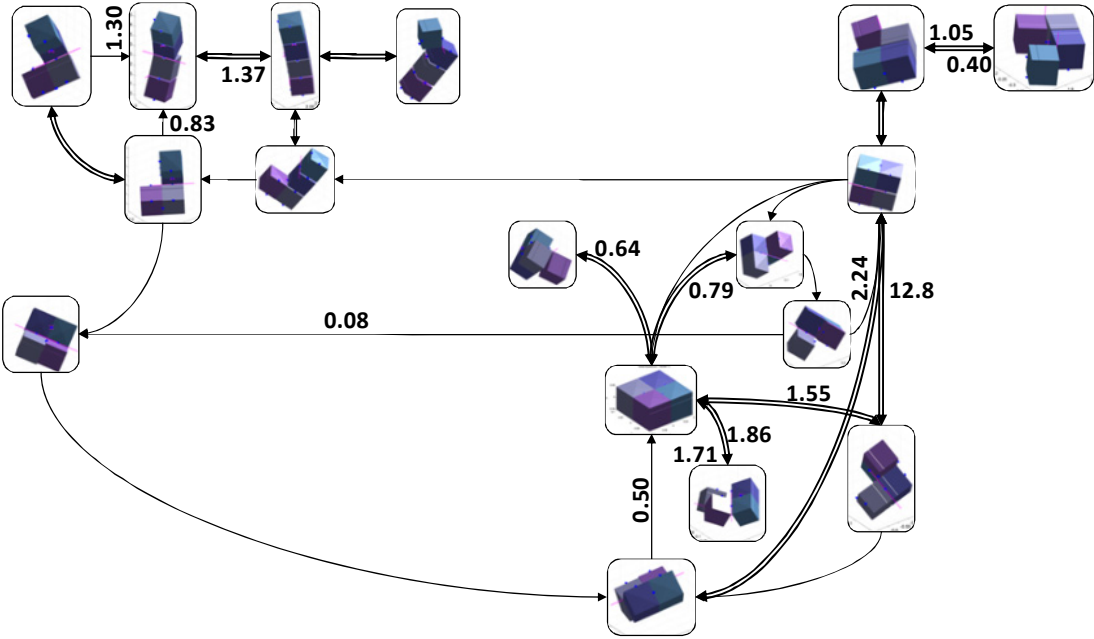


Fig. 6-8 Imaging-mission reconfiguration graph weighted by a relative measure of the time during which at least one cube face is within 20° alignment of an arbitrary vector. Edge labels that are zero are not shown; edges with two transitions are labeled near the head of each arrow.

transition between configurations, the computer tallied the total time during which at least one cube face aligned to within  $20^\circ$  of the arbitrary vector  $[1\ 0\ 1]^T$ . The figure does not show zero weights and nodes or subgraphs without any outgoing edges. The spacecraft might maximize this metric (or a similar one) in order to maintain ground coverage with certain instruments or in order to maintain sufficient lighting conditions on solar panels. On the other hand, the metric may represent the amount of time a thermally sensitive component spends in direct sunlight, in which case the spacecraft should choose paths through the graph that have minimum weight.

Many other weighting schemes are possible. One illustrative case, in Fig. 6-9, involves weights that are a measure of each transition's robustness to variation in the individual cube masses. For each directed edge, the computer performs simulations in

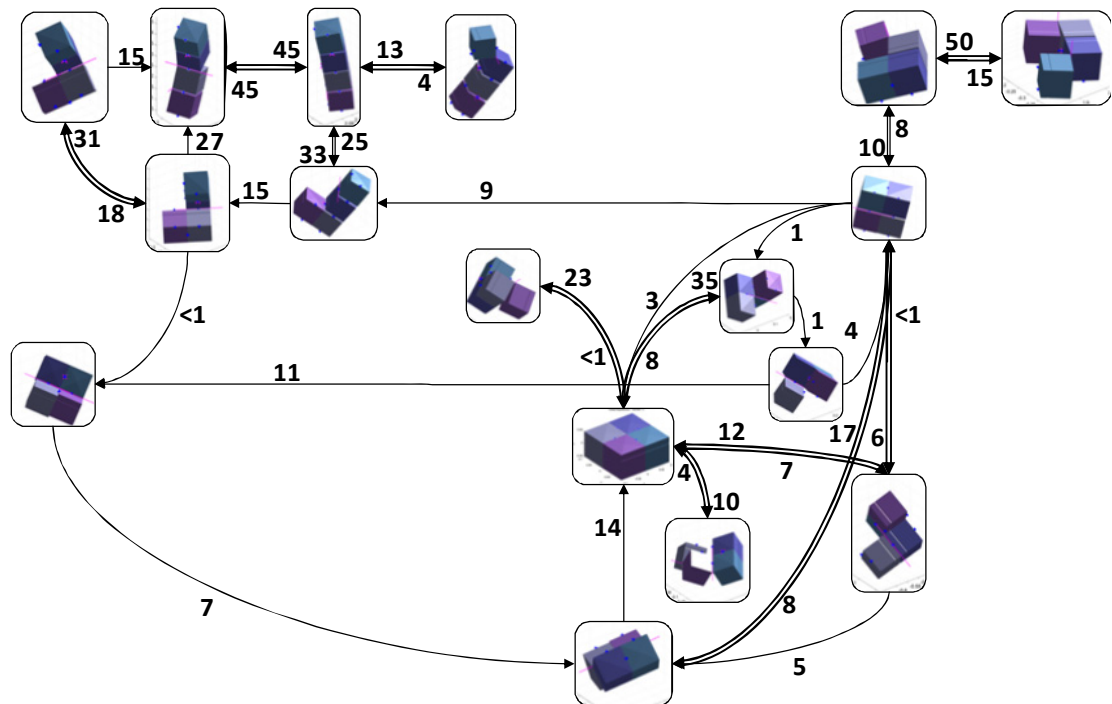


Fig. 6-9 Imaging-mission reconfiguration graph weighted by the maximum percent uncertainty in the individual module masses for which the system successfully completes each transition; edges with two transitions are labeled near the head of each arrow.

which the body masses vary from the nominal case (with masses equal to those specified for the generation of this reconfiguration graph, in Section 6.3.2) up to some percentage amount. The edge weights are the maximum percentage deviation in body masses from the nominal case for which the spacecraft successfully completes each transition according to the passive dynamics the corresponding graph edge specifies. This weighting scheme may be useful if, for instance, an unknown amount of unspent propellant is on board one of the spacecraft. In that case, the spacecraft controller should choose only those transitions with a minimum value of this mass robustness metric. This is an interesting and unusual example because it implements a robust controller without any feedback control.

## 6.4 Chapter Conclusions

The reconfiguration of multibody spacecraft systems in orbit will be an important part of future space development. Reconfiguration is related to the in-orbit docking, assembly, repair, and refurbishment of high-value systems and provides an avenue for small, responsive space systems to perform a wide range of functions and meet many different mission needs. Low-power, robust approaches to space system reconfiguration will allow many more future space systems to take advantage of these capabilities. These systems may include applications from large-aperture, Earth-orbiting telescopes composed of small modules deployed in a phased manner to outer Solar System exploration missions able to adapt to new mission roles and changing science targets. Human spaceflight activities will also benefit from failure-robust reconfiguration techniques that enable expansions to space stations or self-repair and adaptation of manned vehicles beyond low Earth orbit.

This chapter described a potential low-power, robust method to reconfigure modular space systems by stating the problem of reconfiguration from one shape to another as a stepwise sequence of kinematics and passively stable dynamics rather than as an active tracking problem. A spacecraft system undergoing such a reconfiguration maneuver achieves low control and computation effort by taking advantage of the ambient force fields naturally present in the space environment, such as gravity, or augmenting these forces with additional force fields from passive sources, such as permanent magnets. The passive dynamics of the system add robustness by reducing the number of actuators required for reconfiguration and placing the onus of regulating the low-level dynamics of the maneuver on multibody kinematics rather than an on-board control system. This strategy gives the system determinacy in each step of the reconfiguration, in the sense that the system moves towards known dynamic equilibria. Operators can confirm the system configuration at each of these “safe steps.” Should any problem arise during the process, the spacecraft will naturally fall into a stable equilibrium configuration, from which recovery operations can safely take place.

In addition, this chapter developed a simulation environment for multibody spacecraft simulations, based on the equation of motion formulation advocated by Udwadia and Kalaba. Those equations of motion have been adapted to account for full three-dimensional rigid body dynamics with quaternion states. The MATLAB simulation environment is object-oriented, extensible, and allows access to the full system

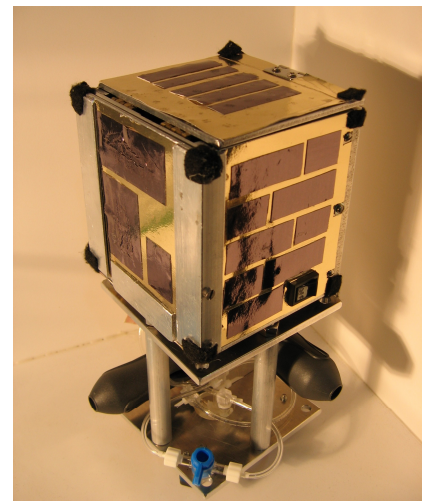


*Fig. 6-10 Air-levitated, CubeSat-sized laboratory demonstration unit.*

state for analysis during and after simulation. Simulations of example multibody spacecraft architectures provide a means to explore the full tree of possible sequential-equilibrium reconfigurations for a given system, thus determining the reachable configurations and control input sequence of kinematics to reach them. These simulation tools have numerous other applications to multibody dynamics problems, as well.

In the future, laboratory testbeds will demonstrate implementations of these reconfiguration algorithms and control strategies. The enumeration approach for constructing reconfiguration graphs outlined in Section 6.1 is generalizable to many multibody space systems. Air-levitated spacecraft simulator systems in the laboratory, such as the one shown in Fig. 6-10, and future NASA microgravity flights will verify that the enumeration algorithm identifies the possible equilibrium configurations and the proper connectivity between them. With a reconfiguration graph in hand, these systems will also demonstrate practical implementations of reconfiguration control through sequential equilibria and provide data on power usage and fault tolerance of the control strategy to sensing, actuation, or control failures in a real system.

These theoretical tools have applications to more general reconfigurable systems than those linked by magnetic flux pinning or other non-contacting forces. They apply to any systems which can alter kinematic constraints, modify connectivity between bodies, or apply force fields. A logical extension from applied force fields to body forces and torques will generalize these methods to many other reconfiguration problems, as well, though in such cases the system will not have the stability guarantees of stable potential wells. The techniques and data from this research may enable new classes of reconfigurable space systems or enhance the capabilities of existing and next-generation space systems.

## CHAPTER 7

### CONCLUSIONS

This dissertation introduces magnetic flux pinning, an intriguing physical interaction between Type II superconductors and magnetic fields, as the basis of an enabling technology for the self-assembly and reconfiguration of modular space systems. Such spacecraft would consist of modules linked by the mechanical stiffness and damping of flux pinning, but with several-centimeter separations between neighboring modules. The modules passively attract each other into stable configurations without the danger of collisions. Furthermore, certain magnetic field shapes introduce degrees of freedom to the flux-pinned connection that have zero stiffness, causing the interfaces to become non-contacting kinematic joints and enabling new techniques for spacecraft reconfiguration. This unusual concept of a space system blurs the distinction between spacecraft assembly and formation flight, encourages new approaches to the design of modular spacecraft, and may enable the construction of next-generation systems such as sparse-aperture space telescopes and reconfigurable space stations.

In order to pursue flux pinning as a spacecraft technology, this work describes the mechanical properties of the phenomenon and presents engineering metrics that are relevant for design. Experimental investigations found that flux pinning can provide sufficient stiffness to resist perturbations in the space environment with magnets and superconductors of reasonable sizes. Both linear and nonlinear models of flux pinning corroborate these results and provide tools for design. Relevant design parameters for flux-pinned docking interfaces include the amount of magnetic flux at the superconductor surface, the size and placement of ferromagnetic materials to shape the

field around the superconductor, the amount of eddy-current damping conductive materials near the superconductor provide, and the range of actuation nearby electromagnets can accomplish.

Demonstrations of flux-pinned docking interfaces at the CubeSat scale show that flux pinning is a viable technology for space applications. Tests in the laboratory as well as in a relevant microgravity environment reveal that nanosatellite-sized spacecraft can support the requirements of flux-pinning components. These demonstrations include passive station-keeping of two spacecraft modules within several centimeters, relative position and orientation actuation superimposed on the passive stability of flux pinning, and an implementation of a non-contacting hinge for reconfiguration.

The capability of flux-pinned interfaces to form various kinematic joints by shaping magnetic fields inspire the development of control strategies for modular spacecraft reconfiguration based on altering joint kinematics. These spacecraft comprise hybrid systems in which the ambient forces of the space environment drive the system to different, passively stable, dynamic equilibria based on the controller's choice of kinematics. The set of possible equilibrium configurations available to a given spacecraft is computed in simulations based on a multibody dynamics software package developed for this work. These possible configurations are stored as nodes in a graph, with edges labeled by the kinematic choices that initiate each passively stable reconfiguration. This strategy casts the problem of multibody spacecraft reconfiguration as a computationally efficient system-level graph search and, with appropriate pruning of nodes from the graph, provides guarantees that systems always avoid undesirable or risky maneuvers.

Future work on flux-pinned technologies and systems will continue to push their technology readiness level towards an on-orbit demonstration. The design principles identified in this work will be honed in experiment and with the development of more accurate numerical models for flux pinning. Air-levitated systems in the laboratory will provide a development platform for control algorithms to provide high-bandwidth, precise positioning of modules linked by the low-stiffness but passively stable interaction of flux pinning. These air-levitated spacecraft simulators will also allow demonstrations of kinematically controlled reconfiguration maneuvers on a physical system, providing information on the requirements and robustness properties of such controllers. Eventually, on-orbit demonstrations of spacecraft linked together by non-contacting, flux-pinned interfaces may be achieved at the nanosatellite or microsatellite scale, proving the technology before it is implemented on larger self-assembling, reconfigurable systems.

## REFERENCES

- 1 Thunnissen, D. "Balancing Cost, Risk, and Performance under Uncertainty in Preliminary Mission Design," *AIAA Space 2004 Conference and Exhibit*, Washington, D.C., 2004.
- 2 Rehnmark, F., Pryor, M., Holmes, B., Pedreiro, N., and Carrington, C. "Development of a Deployable Nonmetallic Boom for Reconfigurable Systems of Small Modular Spacecraft," *48th AIAA/SME/ASCE/AHS/ASC Structures, Structural Dynamics, and Materials Conference*, Washington, D.C., 2007.
- 3 Dong, S., Allen, K., Bauer, P., Bethke, B., Brzezinski, A., Coffee, T., Chambers, R.-D., Flores, M., Gallagher-Rodgers, A., Head, J., Heiman, M., Hoff, N., Horin, C., Horvath, M., Jordan, E., Keesee, J., Kim, S., Kong, E., Koscielniak, A., Lawrence, S., Marquiss, J., McQuin, C., McRae, J., Miller, D., Modisette, J., Moghbeli, J., Nolet, S., Rodgers, L., Saenz-Otero, A., Schaffer, A., and Yesil, C., "Self-assembling wireless autonomously reconfigurable module design concept," *Acta Astronautica*, Vol. 62, 2008, pp. 246-256.
- 4 Domínguez-García, A., Hanuscahk, G., Hall, S., and Crawley, E. "A Comparison of GN&C Architectural Approaches for Robotic and Human-Rated Spacecraft," *AIAA Guidance, Navigation, and Control Conference and Exhibit*, Washington, D.C., 2007.
- 5 Duren, R., "Validation and Verification of Deep-Space Missions," *Journal of Spacecraft and Rockets*, Vol. 41, No. 4, 2004, pp. 651-658.
- 6 Lillie, C. "On-Orbit Assembly and Servicing for Future Space Observatories," *AIAA Space 2006 Conference*, Washington, D.C., 2006.
- 7 Defense Advanced Research Projects Agency (DARPA). Orbital Express On-Orbit Mission Updates. [http://www.darpa.mil/orbitalexpress/mission\\_updates.html](http://www.darpa.mil/orbitalexpress/mission_updates.html) (accessed September 2, 2008).
- 8 Pinson, R., Howard, R., and Heaton, A. "Orbital Express Advanced Video Guidance Sensor: Ground Testing, Flight Results and Comparisons," *AIAA Guidance, Navigation, and Control Conference*, Washington, D.C., 2008.
- 9 Brown, O. and Eremenko, P. "The Value Proposition for Fractionated Space Architectures," *AIAA Space 2006 Conference and Exhibit*, Washington, D.C., 2006.
- 10 Brown, O. and Eremenko, P. "Fractionated Space Architectures: A Vision for Responsive Space," *4th AIAA Responsive Space Conference*, Washington, D.C., 2006.
- 11 LeMaster, E., Schaechter, D., and Carrington, C. "Experimental Demonstration of Technologies for Autonomous On-Orbit Robotic Assembly," *AIAA Space 2006*

- Conference, Washington, D.C., 2006.
- 12 Xia, C., Wang, P., and Hadaegh, F., "Optimal Formation Reconfiguration of Multiple Spacecraft with Docking and Undocking Capability," *Journal of Guidance, Control, and Dynamics*, Vol. 30, No. 3, 2007, pp. 694-702.
  - 13 Norman, M. and Peck, M. "Stationkeeping and Reconfiguration of a Flux-Pinned Satellite Network," *AIAA Guidance, Navigation, and Control Conference*, Honolulu, HI, 2008.
  - 14 Gersh, J. "Architecting the Very-Large-Aperture Flux-Pinned Space Telescope: A Scalable, Modular Optical Array with High Agility and Passively Stable Orbital Dynamics," *AIAA Guidance, Navigation, and Control Conference*, Honolulu, HI, 2008.
  - 15 Jones, L. and Peck, M. "Prospects and Challenges of Particulate Solar Sail Propulsion," *AIAA/AAS Astrodynamics Specialist Conference*, Honolulu, HI, 2008.
  - 16 Brandt, E. H., "Rigid levitation and suspension of high-temperature superconductors by magnets," *American Journal of Physics*, Vol. 58, 1990, pp. 43-49.
  - 17 Schonhuber, P. and Moon, F. C., "Levitation forces, stiffness, and force-creep in YBCO high-Tc superconducting thin films," *Applied Superconductivity*, Vol. 1994, 1994, pp. 523-534.
  - 18 Kramer, E. J., "Scaling laws for flux pinning in hard superconductors," *Journal of Applied Physics*, Vol. 44, 1973, pp. 1360-1370.
  - 19 Johansen, T. H., Yang, Z. J., Bratsberg, H., Helgesen, G., and Skjeltop, A. T., "Lateral force on a magnet placed above a planar YBa<sub>2</sub>Cu<sub>3</sub>O<sub>x</sub> superconductor," *Applied Physics Letters*, Vol. 179, 1991, pp. 179-181.
  - 20 Davis, L. C., "Lateral restoring force on a magnet levitated above a superconductor," *Journal of Applied Physics*, No. 1990, 1990, pp. 2631-2636.
  - 21 Brandt, E. H., "Levitation in Physics," *Science*, Vol. 243, 1989, pp. 349-355.
  - 22 Moon, F. C. *Superconducting Levitation*, Wiley, New York, 1994.
  - 23 Sugiura, T., Aoyagi, T., Ura, H., and Yoshizawa, M., "Parametrically excited horizontal and rolling motion of a levitated body above a High-Tc Superconductor," *IEEE Transactions on Applied Superconductivity*, Vol. 13, No. 2, 2003, pp. 2247-2250.
  - 24 Hull, J. R. and Cansiz, A., "Vertical and lateral forces between a permanent magnet and high-temperature superconductor," *Journal of Applied Physics*, Vol. 86, No. 11, 1999, pp. 6396-6405.
  - 25 Earnshaw, S., "On the nature of the molecular forces which regulate the constitution of the luminiferous ether," *Transactions of the Cambridge Philosophical Society*, Vol. 7, 1842, pp. 97-112.
  - 26 Kong, E. M. C., Kwon, D. W., Schweighart, S. A., Elias, L. M., Sedwick, R. J., and Miller, D. W., "Electromagnetic Formation Flight for Multi-Satellite Arrays,"

- Journal of Spacecraft and Rockets*, Vol. 41, No. 4, 2004, pp. 659-666.
- 27 Schaub, H., Parker, G. G., and King, L. B., "Challenges and Prospects of Coulomb Spacecraft Formations," *Journal of the Astronautical Sciences*, Vol. 52, No. 1, 2004, pp. 169-193.
  - 28 Johansen, T. H. and Bratsberg, H., "Theory for lateral stability and magnetic stiffness in a high-Tc superconductor-magnet levitation system," *Journal of Applied Physics*, Vol. 74, 1993, pp. 4060-4065.
  - 29 Norman, M. C. and Peck, M. "Characterization and modeling of a modular satellite network," *AAS/AIAA Astrodynamics Specialist Conference*, Washington, D.C., 2007.
  - 30 Norman, M. and Peck, M., "Simplified Model of a Flux-Pinned Spacecraft Formation," *Journal of Guidance, Control, and Dynamics*, Vol. 33, No. 3, 2010, pp. 814-822.
  - 31 Werner, M., "Spitzer: the first 30 months," *Astronomy & Geophysics*, Vol. 47, No. 6, 2006, pp. 11-16.
  - 32 Breger, L. and How, J., "Safe Trajectories for Autonomous Rendezvous of Spacecraft," *Journal of Guidance, Control, and Dynamics*, Vol. 31, No. 5, 2008, pp. 1478-1495.
  - 33 Polites, M. E., "Technology of Automated Rendezvous and Capture in Space," *Journal of Spacecraft and Rockets*, Vol. 36, No. 2, 1999, pp. 280-291.
  - 34 McCamish, S. B., Romano, M., Nolet, S., Edwards, C. M., and Miller, D. W. "Ground and Space Testing of Multiple Spacecraft Control During Close-Proximity Operations," *AIAA Guidance, Navigation, and Control Conference*, Honolulu, HI, 2008.
  - 35 Jones, L. and Peck, M. "Stability and Control of a Flux-Pinned Docking Interface for Spacecraft," *AIAA Guidance, Navigation, and Control Conference*, Toronto, ON, 2010.
  - 36 Rui, C., Kolmanovsky, I., and McClamroch, N. H., "Nonlinear Attitude and Shape Control of Spacecraft with Articulated Appendages and Reaction Wheels," *IEEE Transactions on Automatic Control*, Vol. 45, No. 8, 2000, pp. 1455-1469.
  - 37 Wilson, W., Shoer, J., and Peck, M. "Demonstration of a Magnetic Locking Flux-Pinned Revolute Joint for Use on CubeSat-Standard Spacecraft," *AIAA Guidance, Navigation, and Control Conference*, Chicago, IL, 2009.
  - 38 Shoer, J. and Peck, M., "Stiffness of a Flux-Pinned Virtual Structure for Modular Spacecraft," *Journal of the British Interplanetary Society*, Vol. 62, No. 2, 2009, pp. 57-65.
  - 39 Eshed Robotec Ltd. *SCORBOT-ER Vplus User's Manual*, 1998, pp. 2-2.
  - 40 Basinger, S. A., Hull, J. R., and Mulcahy, T. M., "Amplitude dependence of magnetic stiffness in bulk high-temperature superconductors," *Applied Physics Letters*, Vol. 57, 1990, pp. 2492-2494.

- 41 Johansen, T. H., Riise, A. B., Bratsberg, H., and Shen, Y. Q., "Magnetic levitation with high-Tc superconducting thin films," *Journal of Superconductivity*, Vol. 11, 1998, pp. 519-524.
- 42 Shoer, J. and Peck, M., "Reconfigurable Spacecraft as Kinematic Mechanisms Based on Flux-Pinning Interactions," *Journal of Spacecraft and Rockets*, Vol. 46, No. 2, 2009, pp. 466-468.
- 43 Wittenburg, J. *Dynamics of Systems of Rigid Bodies*, B.G. Tenbner, Stuttgart, 1977.
- 44 Shoer, J. and Peck, M., "Flux-Pinned Interfaces for the Assembly, Manipulation, and Reconfiguration of Modular Space Systems," *Journal of the Astronautical Sciences*, 2011.
- 45 Kordyuk, A., "Magnetic levitation for hard superconductors," *Journal of Applied Physics*, Vol. 83, No. 1, 1998, pp. 610-612.
- 46 Griffiths, D. *Introduction to Electrodynamics*, 3rd ed.; Prentice Hall, 1999, p. 246.
- 47 Sarafin, T. and Larson, W., Eds. *Spacecraft Structures and Mechanisms: From Concept to Launch*, Microcosm, Inc, El Segundo, CA, 1995, p. 824.
- 48 Halbach, K., "Design of permanent multipole magnets with oriented rare earth cobalt material," *Nuclear Instruments and Methods*, Vol. 169, No. 1, 1980, pp. 1-10.
- 49 Shoer, J., Wilson, W., Jones, L., Knobel, M., and Peck, M., "Microgravity Demonstration of Flux Pinning for Station-Keeping and Reconfiguration of CubeSat-Sized Spacecraft," *Journal of Spacecraft and Rockets*, Vol. 47, No. 6, 2010, pp. 1066-1070.
- 50 Udwadia, F. and Kalaba, R. *Analytical Dynamics: A New Approach*, Cambridge University Press, 2007.
- 51 Toumela, J., "Kinematic Analysis of Multibody Systems," *BIT Numerical Mathematics*, Vol. 48, No. 2, 2008, pp. 405-412.
- 52 Henzinger, T. A. "The Theory of Hybrid Automata," *Proceedings of the 11th Annual Symposium on Logic in Computer Science*, IEEE Computer Society Press, 1996, pp. 278-292.
- 53 Udwadia, F. and Phohomsiri, P., "Explicit Equations of Motion for Constrained Mechanical Systems with Singular Mass Matrices and Applications to Multi-Body Dynamics," *Proceedings of the Royal Society A*, Vol. 462, 2006, pp. 2097-2117.
- 54 Bondy, J. A. and Murty, U. S. R. *Graph Theory with Applications*, Elsevier Science Publishing Co., New York, 1976, p. 19.
- 55 Shoer, J. and Peck, M. "A Flux-Pinned Magnet-Superconductor Pair for Close-Proximity Station Keeping and Self-Assembly of Spacecraft," *AIAA Guidance, Navigation, and Control Conference*, Washington, D.C., 2007.
- 56 Norman, M. C. and Peck, M. "Modeling and Properties of a Flux-Pinned Network of Satellites," *AAS/AIAA Astrodynamics Specialist Conference*, Washington, D.C., 2007.

- 57 Gu, E. Y. L., "Configuration Manifolds and Their Applications to Robot Dynamic Modeling and Control," *IEEE Transactions on Robotics and Automation*, Vol. 16, No. 5, 2000, pp. 517-527.
- 58 Shoer, J. and Peck, M. "Sequences of Passively Stable Dynamic Equilibria for Hybrid Control of Reconfigurable Spacecraft," *AIAA Guidance, Navigation, and Control Conference*, Chicago, IL, 2009.